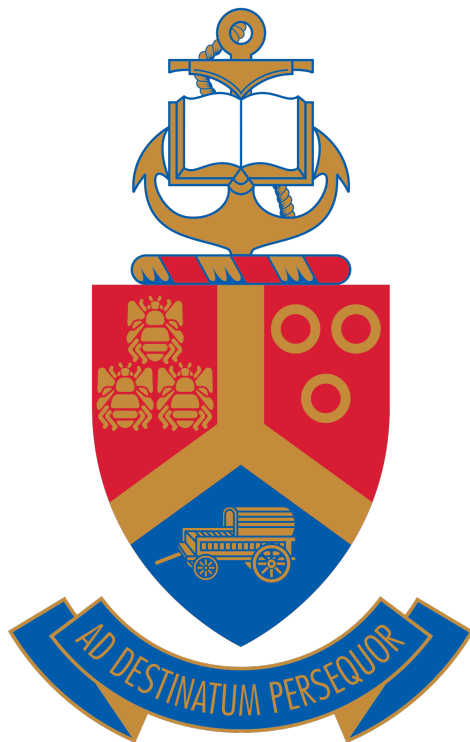# First-principles study of the enhancement of electrochemical performance of a SnS$_2$ monolayer for lithium/sodium-ion batteries via vacancy defects

by

Craig Arthur Bekeur

Submitted in partial fulfilment of the requirements for the degree

Magister Scientiæ(MS) in Physics

in the Faculty of Natural and Agricultural Sciences

University of Pretoria

Supervisor: Dr. Refilwe Edwin Mapasha

June 29, 2023

UNIVERSITY OF PRETORIA

DECLARATION OF ORIGINALITY

This document must be signed and submitted with every essay, report, project, assignment, dissertation, and/or thesis.

Full names of student: CRAIG ARTHUR BEKEUR

Student number: u16019220

Personnel number:

Declaration

1. I understand what plagiarism is and am aware of the University's policy in this regard.

2. I declare that this thesis is my own original work. Where other people's work has been used (either from a printed source, Internet or any other source), this has been properly acknowledged and referenced in accordance with departmental requirements.

3. I have not used work previously produced produced by another student or any other person to hand in as my own.

4. I have not allowed, and will not allow, anyone to copy my work with the intention of passing it off as his or her own.

SIGNATURE STUDENT:_____

SIGNATURE SUPERVISOR:_____

Abstract

Various transition metal dichalcogenides materials have been investigated from bulk to monolayer phases for different advanced technological applications. Tin disulfide monolayer offers advantages as an anode material for Li/Na-ion batteries, although it cannot be considered an ideal for direct exploitation. We systematically performed a comparative study of the adsorption and diffusion behaviour of Li/Na on a pristine SnS_2 monolayer and on a SnS_2 monolayer with a S-vacancy for enhancement of electrochemical performance, using the density functional theory approach. Although all the adsorption sites are exothermic, it was established that Li/Na adatoms mostly prefer to bind strongly on a SnS_2 monolayer with a S-vacancy but avoiding the S-vacancy site. It was established that avoiding the S-vacancy site along the path, an excellent diffusion barriers of 0.19 eV for Li and 0.13 eV for Na were achieved, suggesting possible ultrafast charge/discharge rate. Due to reduced molar mass, the SnS_2 monolayer with a S-vacancy has a slightly higher storage capacity than its pristine counterparts for both Li and Na adatoms. The obtained open circuit voltage values are within the range of 0.25–3.00 V assuring that the formation of dendrites can surely be averted for the envisaged battery operation. Understanding the effects of an S-vacancy on the electrochemical properties of Li/Na on the SnS_2 monolayer allows us to consider possible improvements to energy storage devices that can be applied as a result of improved anode material.

Dedication

To my beloved family, supportive throughout all the days of triumphs and hardships.

Acknowledgements

Contents

List of Figures

List of Tables

List of Abbreviations

AE all-electron. 45, 47

BZ Brillouin zone. 41–44

CBM conduction band minimum. 75–77

CNT carbon nanotube. 21

CP carbon paper. 23

CVT chemical vapour transport. 7

DFT density functional theory. 8, 9, 16, 17, 19, 21–24, 29, 33, 35, 39–41, 43, 45, 47, 48, 53, 84

DFTB density-functional tight binding. 21

DOS density of states. 7, 21, 49, 58, 75, 76

G graphene. 20

GGA generalized gradient approximation. 29, 36, 38–40, 49, 56, 67

HK Hohenberg-Kohn. 29, 33–35, 41

HRTEM high-resolution transmission electron microscopy. 20

IBZ irreducible Brillouin zone. 44

KS Kohn-Sham. 29, 35, 36, 38, 40–43, 47, 48

LDA local density approximation. 29, 36–40

LIB lithium-ion battery. 1–4, 7, 8, 15–23, 62, 65, 69, 70, 77, 79, 84

LSDA local spin density approximation. 37, 38

MC mesoporous carbon. 20

MPI message passing interphase. 48

Chapter 1

Introduction

In this introductory chapter, a brief overview is given of battery technologies, and the limitations resulting from the configuration and choice of materials of the most popular commercial batteries. This is followed by exploring alternative materials applicable to energy storage, and the main idea of our research, which focuses on monolayer tin disulfide (SnS_2) in particular as an anode material. The chapter ends by highlighting the aims and objectives of this dissertation, and an outline of the remaining chapters.

1.1 Rationale

The modern lifestyle is heavily dependant on portable electronic devices, such as mobile phones or laptop computers, which in turn requires the application of high density energy storage. Attempts to acquire energy storage started with lead-acid batteries, which displayed at the time commendable cycling stability. [1] The drawbacks of their significant size and weight made them unfit for portable electronic devices. The major requirements for modern energy storage in electronic devices are low weight, long life span, long term cycling stability, high energy density and quick charge/discharge rate. [2] The earliest energy storage devices were nickel-cadmium and nickel-metal hydride batteries. The former showed poor battery life span and dangerous component toxicity, while the latter was prone to leakage. [3,4] The lithium-ion battery (LIB) was soon developed. Its lightweight structure and volume reduction meets portability requirements, while leakages are countered with the introduction of solid polymer electrolytes to replace the existing liquid electrolytes. [5] To date, there is a continuous and rising global demand for batteries, and in turn, the variety of materials that are required for the construction. In turn, the dwindling supply of mineable lithium sources has fueled interest in more abundant elements as alternative charge carriers. [6]

1.1.1 Li/Na-ion batteries

The largest fraction of materials used as charge carriers for high density energy storage are lithium and sodium, representing Li-ion batteries (LIBs) and Na-ion batteries (NIBs). The former is the primary material for commercial batteries, and fuels a continuous demand that is severely limited by the scarcity of lithium in nature. At the turn of the century in 2000, LIBs were a relatively young technology, and considered the system of choice for their high energy density and flexibility when compared to contemporaries. Fifteen years later, there is growing awareness of the depletion of fossil-fuels and the requirement
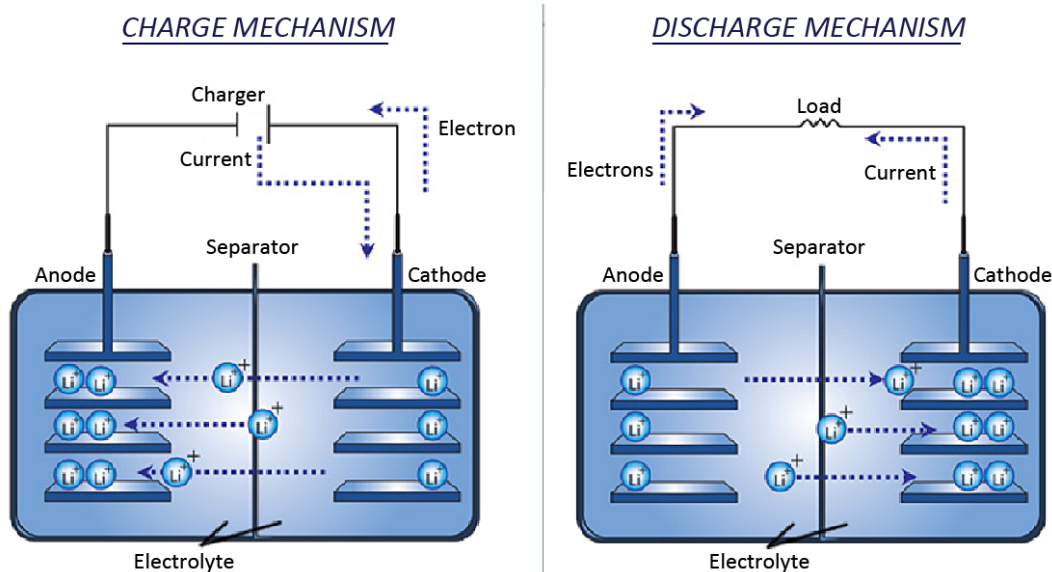
Figure 1.1: Charge and discharge cycles of the lithium-ion battery. Reproduced from Omar *et al.* (2012)

for energy sustainability. It is essential to consider elemental abundance, toxicity, and scalability when considering the development of battery technologies, which includes looking beyond the commercial LIB templates.[7,8]

The structure of LIBs consists of three components: the negative electrode (anode), the electrolyte, and the positive electrode (cathode). As we can see in figure 1.1, during the discharge cycle, Li-ions will migrate through the electrolyte from the anode to the cathode. The anode and cathode are electrically isolated from each other by a separator. There is a choice of either a liquid or solid electrolyte. The former hinders performance due to a tendency to react with the electrode surfaces, forming an interfacial layer that increases resistance to charge flow during cycling. Battery performance also depends on the amount of Li-ions that can be stored in the electrodes. The storage of a higher Li concentration indicates a higher storage capacity, allowing more energy to be extracted from the battery during operation.[9,10]

The most popular cathodes for commercial LIBs are lithium cobalt oxide ($LiCoO_2$) and graphite, with the former having been investigated as early as 1981, in a Mizushima *et al.* article on Li intercalation onto lithium cobalt oxide[11]. These designs have since approached a critical limit in energy density. In 2007, Ohzuku & Brodd reviewed alternative cathode materials for LIBs: lithium transition metal phosphates, layered lithium manganese oxides, and lithium nickel manganese oxides with or without cobalt.[12] The more advanced materials have all undergone trials on application in both high-power LIBs, and hybrid capacitors leading to 12 V lead-free accumulators.

Regarding lithium abundance as of 2013, Vikstrom *et al.* reported that due to lithium being a finite resource, as well as restraints due to geological, technical and economical conditions, production cannot be infinitely large.[6] As lithium depletion in nature continues, future extraction becomes progressively more expensive. This severely limits the application of LIBs to large scale developments, such as enabling a transition to electrical vehicle for the majority of the population. Investigations into the recycling of existing lithium resources can be undertaken. Otherwise, alternative battery types must be considered and developed, discouraging the use of lithium or similarly restricted materials.

The first demonstration of reversible electrochemical Na intercalation was observed on TiS_2 in 1980.[13] Following this demonstration, NIBs have not been commercialized due to positive results shown in the application of LIBs. More recently, the development of rechargeable batteries is instead aimed at sustainable energy in future. From an article by Stevens & Dahn[14] in 2000, Na insertion onto graphite-based carbon anode materials has achieved a reversible capacity of 300 mAh/g, similar to what is possible with lithium insertion, despite atomic size differences. This suggests a similar life span and discharge length for NIBs and LIBs. Since 2010, NIBs have attracted interest following changing social situation and the more developed field of battery technology. Sodium is present in abundance and evenly distributed in the Earth's crust and sea. Additionally, even if Na atoms have a greater atomic size than Li atoms, few concessions are required to accommodate Na, as sodium remains the second-lightest alkali metal following lithium.[15]

The methodology utilized in the design of LIBs does not necessarily transfer directly over to NIBs, although there is some crossover. NIB materials are similar, but differences are clear in the case of air stability, for instance with high energy density O_3-type layered oxide electrode materials.[16] This and similar issues require differences in the mixing as well as coating during manufacture, so as to improve shelf life for the components. Additionally, safety procedures that might be required for NIBs are not well researched, although substituting the copper current collector for an aluminium collector should prevent some types of failure.[17] Additional information is required regarding the choice of electrolyte interphase to prevent reactivity, along with thermal stability. If these issues are addressed, NIB would prove a cost-effective alternative to LIBs. A more difficult issue to overcome is the lower energy densities present in NIB designs, necessitating further investigation to approach, but not surpass, LIB energy densities.

Graphite, the commercial anode for LIBs, is not easily applicable to NIBs due to its extremely low storage capacity. Sodium requires precise conditions for insertion into graphite, such as a helium or vacuum atmosphere to result in the formation of NaC_{64}. In comparison, hard carbon exhibits reversible capacity of 400 mAh/g with sodiation potential plateauing at 0.05 V, which is higher than for lithiation, and is perhaps the best short term choice for mass production of NIBs. There is a lower risk of Na dentrite formation, which as consequence could cause an internal short circuit through the seperator film, a defect observed in practical LIBs. Looking at other materials, tin (Sn) and phosphorus (P) are especially noteworthy. When used as anode materials for NIBs and LIBs, they deliver higher theoretical specific capacities for the former, at 700 mAh/g for Sn and 1600 mAh/g for P. Sn-P alloys mixed with carbon via mechanical ball milling allows for the production of even higher capacity anodes.[18] As for cathodes, 3d transition metals (Fe, Co, Cu, Ni, Zn) improves the stability of layered structures such as sodium transition metal oxides, due to the significant difference in ionic radius between the transition metal ions and Na^+. Fe-based oxides in particular are electrochemically active in Na cells (unlike Li cells), potentially lowering production costs of NIBs. In general, the wide variety of transition metals as dopants allows near precise engineering of properties for the layered oxides, such as crystal structure, electronic or ionic conductivity, water-resistance, and phase transitions during charge and discharge.[19]

The above mentioned developments are mostly restricted to the variation in molecular composition of the electrode material. Another path for the development of improved battery technology, while still focusing on the electrode material, is the application of advanced crystal structures. In particular, consider the application of 2D or layered materials, such as graphene and its derivatives.

1.1.2 Graphene and similar 2D materials

Graphene, or as described by Novoselov *et al.*, monocrystalline graphite films, are metallic, have high structural quality, and remain stable under ambient condition while only being a few atoms thick[20]. Graphene films are two-dimensional (2D) semimetals, having a tiny overlap between the valence and conduction bands, and exhibit strong ambipolar electric field effects, with electrons and holes being present in concentrations of up to 10^{13} cm^{-2}. Applying a gate voltage can induce mobility of approximately 10000 cm^2/Vs in standard temperature and pressure conditions. Recent progress in graphene-based materials, particularly as nodes for LIBs and NIBs, is reviewed in 2019 in an Al Hassan *et al.* article[21]. The review comes to the conclusion that graphene preserves a higher Li$^+$ or Na$^+$ charge than more basic graphitic carbon, mostly due to the unique 2D structure.

First-principles investigation of Li adsorption and intercalation, for mono- and few layer graphene compared with bulk graphite, was conducted in a 2012 Lee and Persson study[22]. The monolayer graphene investigation looked for the lowest energy ion configuration as a function of Li adsorption using a cluster expansion method. The predicted result was no arrangements of Li existing that will stabilize Li adsorption in the absence of any defects in the graphene substrate, due to the substrate having a positive adsorption energy for Li. This result shows that monolayer graphene is inferior to bulk graphite in terms of Li capacity, in the absence of defects. In comparison, for few layer graphene the addition of van der Waals interlayer forces requires taking account of the contribution of empty interlayer sites (lacking Li) to the total energy. Analyzing Li intercalation shows that this mechanism allows for an increased Li concentration compared to monolayer graphene. The capacity still remains inferior to graphite for defect-free graphene.

A significant drawback when using graphene is the weak Li binding energy, which allows for the formation of Li atom clusters that can nucleate to undesired dendrites.[23,24] To counteract this issue, several theoretical and experimental avenues to improve Li-graphene binding have been explored.[25] Modification of the graphene anode structure, so as to improve electrochemical properties, can be achieved through a conversion of the pristine graphene to either a nanocomposite or nanohybrid, or by incorporating defects such as voids and pores (both vacancy defects), or substitution defects. Various graphene derivatives have also been considered, including graphane, graphone, and flourographene. The graphene composites and hybrids in particular offer a improved charge storage capacity due to a larger specific surface area, which allow for fast and facile Li$^+$ or Na$^+$ diffusion paths. Additionally, the structures accommodate changes in volume, and will hinder the formation of the solid-electrolyte interphase (SEI) layer which results from material decomposition.[26–29]

Regardless, while graphene is very popular because of its unique properties, the lack of an electronic band gap encourages an investigation into other novel 2D materials that do display semiconducting characteristics. Other comparable materials that displayed the preferred characteristics needed for LIBs and NIBs are various nanoparticle metallic oxides, sulfides, and phosphides. Graphene-like layered materials consisting of group 14 elements have also been considered, such as stanene, silicene, and germanene.[30,31] A promising alternative is seen in transition metal dichalcogenides (TMD). This is a group of semiconductors with chemical formula MX$_2$, with M being transition metal atom (such as Mo, W, Se, Sn, etc.) and X is a chalcogen atom (group 16 elements). MoS$_2$ in particular is a well studied TMD material, chiefly because of its robustness. In general, the layered metal dichalcogenides are quasi-one-dimensional molecular crystals that form a unique class of crystal structures known as molecular close packed, and have

a monolayer minimal unit of the crystal structure.[32] TMDs are characterized by a unique combination of atomic-scale thickness, direct band gap, and strong spin–orbit coupling. In addition, TMDs also possess weaker interlayer van der Waals interaction, which accommodates Li or Na intercalation with less volume expansion, a boon for improving cycling stability. These properties along with favourable mechanical and electronic properties make TMDs an interesting prospect for study, as well as possible application in high-end and/or flexible electronics, spintronics, optronics, and energy harvesting.[33]

In particular, TMDs have significant potential for energy storage in nanotechnology, due to large surface areas. TMD layered materials are a diverse group, with a large fraction of the members less explored for application in 2D systems.[34] TMD layers with variable thickness and size can be produced via an exfoliation or vapour phase deposition method to a degree of quality sufficient to achieve excellent electronic and optical properties. Due to these properties as well as the high surface areas of TMDs, the material applied as semiconducting monolayers can be used in various energy related devices, such as nano generators, electrocatalytic hydrogen generation, or high performance energy storage. Monolayer SnS_2 in particular is a typical example of TMD properties.

1.1.3 Monolayer SnS_2 structure

(a) 1T-SnS_2 (b) 1H-SnS_2
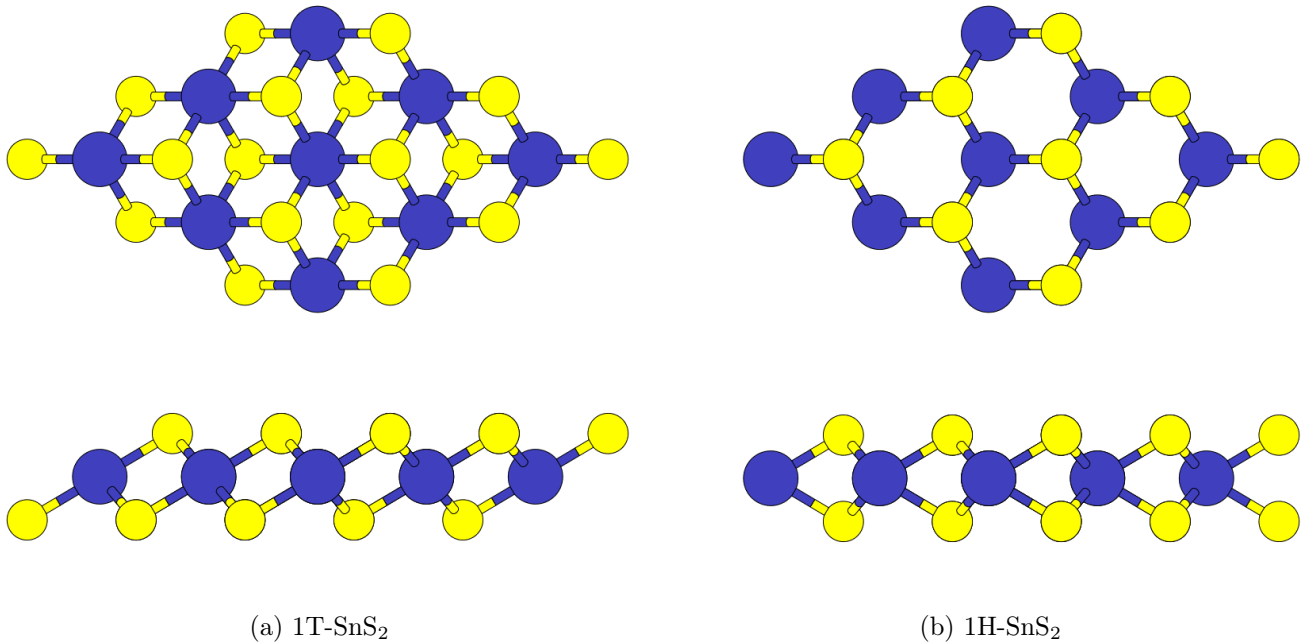
Figure 1.2: The top views (top row) and side views (bottom row) of the SnS_2 monolayer phases, 1T and 1H.

One of the less explored TMDs is the hexagonal 2D tin disulfide (SnS_2), which has a PbI_2 layered structure with a hexagonal unit cell. The Sn atoms are located in octahedral sites between two hexagonally close-packed S layers, forming a sandwich structure. There are more than 70 polytype structures of SnS_2, as previously established from complex single crystal structure analysis.[35] All of the polytypes have the same hexagonal close-packed structure within the layer, and therefore an identical unit cell lattice constant a of 3.647 Å. Differences are exhibited for lattice constant c, which also governs interlayer distances. The

H and T phases are used to denote some polytypes of multilayer SnS_2, designating the number of layers and their phase types, such as 1T, 2H, and 4H, although there is more interest in the monolayer polytypes for application in anode materials.

From Bacaksiz *et al.*, it has been reported that the two phases of monolayer tin disulfide are 1T and 1H (see 1.2), the latter of which occurs in nature as 2H.[36] Both structures have an Sn subplane sandwiched between two S subplanes, and have a hexagonal prism unit cell. The difference in their structures lies in the offset between the S layers. The 1H-SnS_2 unit cell belongs to the $P\bar{6}m2$ (trigonal prismatic) space group, with the S atoms in both layers have the same x and y coordinates (stacked ABA). For the 1T-SnS_2 unit cell the S layers are mirrored across the xy-plane, meaning the x and y coordinates are swapped (stacked ABC), and fits into the close packed $P\bar{3}m2$ (octahedral) space group. Both phases have the same lattice vectors describing the two-dimensional unit cells:

$$\mathbf{v}_1 = a \left(\frac{1}{2}, \frac{\sqrt{3}}{2}, 0 \right)$$

$$\mathbf{v}_2 = a \left(\frac{1}{2}, -\frac{\sqrt{3}}{2}, 0 \right),$$

which have the same magnitude or lattice constants such that $|\mathbf{v}_1| = |\mathbf{v}_2| = a$. From these lattice vectors, we can go on to define atomic coordinates for the Sn atom and the two S atoms for both monolayer SnS_2 phases. First, note that lattice constant c, which describes the width of the unit cell along the z-axis, also describes the distance between monolayers. The atomic positions for T1-SnS_2 are:

$$\mathbf{R}(\text{Sn}) = \left(\frac{a}{2}, \frac{a}{2}, 0 \right)$$
$$\mathbf{R}(\text{S}) = \left(\frac{a}{6}, \frac{a}{6}, \frac{c}{2} \right) \tag{1.1}$$
$$\mathbf{R}(\text{S}') = \left(\frac{5}{6}a, \frac{5}{6}a, -\frac{c}{2} \right),$$

where $\mathbf{R}(\text{S})$ and $\mathbf{R}(\text{S}')$ represents atomic positions for the top and bottom layer S atoms respectively. Meanwhile, the atomic positions for 1H-SnS_2 are:

$$\mathbf{R}(\text{Sn}) = \left(\frac{a}{3}, \frac{a}{3}, 0 \right)$$
$$\mathbf{R}(\text{S}) = \left(\frac{2}{3}a, \frac{2}{3}a, \frac{c}{2} \right) \tag{1.2}$$
$$\mathbf{R}(\text{S}') = \left(\frac{2}{3}a, \frac{2}{3}a, -\frac{c}{2} \right).$$

The lattice constants a for 1T- and 1H-SnS_2 are roughly equivalent when measured experimentally, being approximately 3.68 Å, although the 1H lattice constant is expected to be slightly smaller. Previous studies have also recorded an energy difference between the 1T- and 1H-SnS_2 unit cells of approximately 0.8 eV, suggesting that the formation of the 1T-SnS_2 monolayer being slightly favourable over 1H-SnS_2. This energy difference also suggests a greater material stability, making 1T-SnS_2 the preferred polytype for implementation in nanotechnology and in turn anode materials.[36–38]

Tin disulfide is perhaps the first known tin sulfide material, originally known as *aurum mosaicum*

or "mosaic gold", with laboratory synthesis having occurred as early as 1771.[39] Various methods to synthesize tin disulfide exist, with the chemical vapour transport (CVT) technique being used for the majority of bulk synthesis. Single crystals of SnS_2 have been prepared by iodine vapour transport in 1965 by Greenaway & Nitsche. While in platelet form, the crystals were readily cleaved, resulting in areas of up to 1 cm^2. Measuring optical absorption for an energy range of 0.05-2.50 eV showed that SnS_2 is an indirect gap semiconductor with a room temperature energy gap of 2.21 eV. Measuring reflectivity (energy range of 1–12 eV) showed multiple strong maxima in the DOS of the fundamental absorption region. These results could tentatively predict the energy band structure of the material, and coupled with exciton studies the experiment supported then recent models to explain the function of interband transitions and excitons in ionic crystals.[40]

Synthesis by Conroy & Park in 1968 used a methodology similar to Greenaway to form SnS_2 single crystals. Forming SnS_2 crystals required SnS_2 powder to seed the formation, with the best crystals having formed when cooling from 700 to 600 °C within 30 hours. Following synthesis conductivity was measured, with SnS_2 being placed into a near-insulator class. This low conductivity results either from low impurity level, or the lack of empty d10 orbitals.[41] In the next decade, a 1972 experiment by Rimmington & Balchin attempted to grow single crystals of various layered compounds.[42] The experiment shows that single crystals of tin disulfide can be grown using iodine vapour transport techniques, resulting in widths of at least 5 mm. The obtained tin disulfide crystal, is found to be near perfect following examination using X-ray topography. Dislocation (surface defect) densities are observably low enough to resolve individual dislocations, with large areas being entirely free from dislocations. At this early stage of experimentation, extremely low density defects are largely undetectable, with the observed defects largely being more significant deviations in the crystal lattice of tin disulfide. Even more recently, a 1998 Jiang & Ozin article on the chemistry of tin sulfides discusses the dense 2D structure of SnS_2.[35] The SnS_2 crytals were again prepared using CVT with iodine I_2 as transport agent.

A more modern approach that allows for the synthesis of SnS_2 thin films, rather than bulk, has the material deposited via the successive ionic layer adsorption and reaction (SILAR) technique. Deposition quality is determined by the numerous parameters. For SnS_2, 60 SILAR cycles at 27 °C, with immersion times of 20s and rinsing time of 10s has proven to be an optimized set of parameters to ensure good quality thin films, as shown by Despande *et al.* in 2007.[43] For these obtained SnS_2 films, X-ray diffraction reveals the expected hexagonal crystal structure, while energy dispersive X-ray analysis shows near exactly correct, having obtained $SnS_{2.02}$. Observation using scanning electron microscopy showed that material deposition over the entire substrate was uniform. The direct band gap was measured at 2.22 eV, and tin disulfide was shown to exhibit n-type conductivity. Ultrathin SnS_2 nanosheets can also be synthesized using a hydrothermal reaction, as seen with Zhai *et al.* in 2011.[44] The hydrothermal method typically has one part $SnCl_4 \cdot 5H_2O$ and four parts thioacetamide (TAA) dissolved into deionized water, after which the resulting solution is heated for 12 hours at 160 °C. The product, SnS_2 nanosheets retrieved post centrifugation and drying, were tested for application as an anode material for LIBs. These nanosheets provide a stable capacity greater than that of carbon-based anodes such as graphite and graphene.

It is apparent that the pristine SnS_2 monolayer is suitable for application in LIBs and similar batteries. When used as an anode material it has been proven to offer improved storage capacity that surpasses commercial anodes. SnS_2 also has the additional advantage of being suitable for alternative charge carriers,

such as sodium and potassium, in the first place. In addition, tin and sulfur is sufficiently abundant such that using these elements instead of carbon is not prohibitively expensive. However, there are some disadvantages to the SnS_2 monolayer that must be discussed, such as the stacking problem widespread in all 2D materials. The engineering of the SnS_2 monolayer, whether through the introduction of defects or by designing heterogeneous or homogeneous structures, with the goal of improving electronic or structural properties, must be considered.

1.2 Aims and objectives

This dissertation is aiming to investigate the enhancement of electrochemical performance of the SnS_2 monolayer for LIBs/NIBs, through the introduction of vacancy defects. These defects are introduced in very low concentrations in the SnS_2 monolayer, looking at the removal of only a single S or Sn atom. Properties likely to be affected by the introduced vacancy defect vary. Focusing on battery technology necessitates that we consider the properties that determine or strongly influence battery performance; these properties include energetic stability, ion mobility, structural stability, electronic conductivity, etc.

Most of these properties will be derived using density functional theory methodology, with the required properties being derived from a computed total energy for each input SnS_2 unit cell or supercell. Within DFT, the derived properties aimed for include activation energy or barrier, binding energy, density of states, open circuit voltage, and specific storage capacity. Each of these values will need to be required for all necessary configurations of the SnS_2 monolayer. Listing the objectives towards obtaining the required results, are:

- Compare the 1H- and 1T-SnS_2 phases to determine the preferred monolayer configuration for use as an anode material.

- Determine the most effective parameters for performing calculations, which includes k-points, cutoff energy, lattice constants, and Hubbard U parameter.

- Determine how the absence of an S or Sn atom will alter the properties of the SnS_2 monolayer. These vacancy defects are also directly compared for suitability in an anode material.

- Analyze the surface diffusion and ion mobility of both Li and Na adatoms across the monolayer surface for the pristine and vacancy configurations. This will identify both diffusion barriers as well as preferable binding sites on the SnS_2 monolayer.

- Calculate the binding energies at the preferred binding sites for both Li and Na adatoms, so as to determine the energetic stability of the SnS_2 monolayer and its vacancy defect configurations.

- Plot the TDOS of the SnS_2 monolayer for all configurations, so as to determine electronic properties such as the band gap and Fermi energy. This in turn partially determines conductivity for the material.

- Comparison of diffusion paths, binding energies, and TDOS for both SnS_2 monolayer vacancy defect configurations, with an S-vacancy or an Sn-vacancy. This is to determine which vacancy defect configuration is most suitable for use as an enhanced anode material.

- Calculate the open circuit voltage (or average voltage) of the SnS_2 monolayer for all configurations, for an increasing number of Li or Na adatoms. This in turn partially shows the charge characteristic of the material.

- For the increasing number of Li or Na adatoms, determine the theoretical specific capacity of the SnS_2 monolayer for all configurations.

- For each of the obtained values (diffusion barrier, binding energy, etc.), make a comparison with similar 2D materials.

Once these objectives are achieved, a much better understanding of the SnS_2 monolayer as an anode material is obtained. In addition, the enhancement of properties using vacancy defects is better understood. Having made a distinction between S- and Sn-vacancies, further DFT research can obtain more specific details regarding material properties, beyond energetic stability and TDOS, for each case, or just the preferred vacancy defect for anode materials. Additional charge carriers might also be considered, such as potassium (K), which is even more abundant in nature than either Li or Na.

1.3   Synopsis

After this introduction, Chapter 2 goes into greater depth on the relevant topics regarding the usage of tin disulfide as an anode material for lithium- and sodium-ion batteries, with a greater emphasis placed on the efforts made to improve upon its deficiencies as an anode through defect engineering. Pristine SnS_2 monolayer properties are listed and elaborated on, as they were discovered in existing experimental and theoretical studies. This is followed up with information on the effects of homogeneous and heterogeneous layering, doping, and vacancy defects. In chapter 3, we expand upon the principles that goes into understanding density functional theory (DFT). This includes concepts such as the Hartree-Fock method, Hohenberg-Kohn theorems, and Kohn-Sham equations. Additionally, the practical application of DFT, through the use of software packages, is discussed. Quantum ESPRESSO, the software package used for this dissertation, is expanded upon, along with all the necessary inputs that go into allowing the software to work correctly.

The calculated results being in chapter 4, with each set of obtained values and plotted figures followed by discussion and any relevant conclusions. These results include structural and electronic properties for the pristine, S-vacancy, and Sn-vacancy SnS_2 monolayer, with values having been produced through the computational application of DFT. Chapter 5 will summarize the obtained results and what we could conclude from them. We detail how the introduction of vacancy defects has altered the electrochemical performance of the SnS_2 monolayer, and what opportunities these changes offer that can be explored in more detail for future studies.

Bibliography

[1] Ken Sawai, Yuichi Tsuboi, Yuichi Okada, Masaaki Shiomi, and Shigeharu Osumi. New approach to prevent premature capacity loss of lead-acid battery in cycle use. *Journal of Power Sources*,

179(2):799–807, 2008. ISSN 0378-7753. doi: https://doi.org/10.1016/j.jpowsour.2007.12.106. URL `https://www.sciencedirect.com/science/article/pii/S0378775307028686`.

[2] Gianfranco Pistoia. *Batteries for portable devices*. Elsevier, 2005.

[3] J. David. Nickel-cadmium battery recycling evolution in Europe. *Journal of Power Sources*, 57(1):71–73, 1995. ISSN 0378-7753. doi: https://doi.org/10.1016/0378-7753(95)02244-9. URL `https://www.sciencedirect.com/science/article/pii/0378775395022449`. Proceedings of battery recycling '95.

[4] Tobias Müller and Bernd Friedrich. Development of a recycling process for nickel-metal hydride batteries. *Journal of Power Sources*, 158(2):1498–1509, 2006. ISSN 0378-7753. doi: https://doi.org/10.1016/j.jpowsour.2005.10.046. URL `https://www.sciencedirect.com/science/article/pii/S0378775305014527`. Special issue including selected papers from the 6th International Conference on Lead-Acid Batteries (LABAT 2005, Varna, Bulgaria) and the 11th Asian Battery Conference (11 ABC, Ho Chi Minh City, Vietnam) together with regular papers.

[5] P.U. Nzereogu, A.D. Omah, F.I. Ezema, E.I. Iwuoha, and A.C. Nwanya. Anode materials for lithium-ion batteries: A review. *Applied Surface Science Advances*, 9:100233, 2022. ISSN 2666-5239. doi: https://doi.org/10.1016/j.apsadv.2022.100233. URL `https://www.sciencedirect.com/science/article/pii/S2666523922000253`.

[6] Hanna Vikström, Simon Davidsson, and Mikael Höök. Lithium availability and future production outlooks. *Applied Energy*, 110:252–266, 2013. ISSN 0306-2619. doi: https://doi.org/10.1016/j.apenergy.2013.04.005. URL `https://www.sciencedirect.com/science/article/pii/S0306261913002997`.

[7] J.M. Tarascon and M. Armand. Issues and challenges facing rechargeable lithium batteries. *Nature*, 414(6861):359–367, Nov 2001. ISSN 1476-4687. doi: 10.1038/35104644. URL `https://doi.org/10.1038/35104644`.

[8] D. Larcher and J.-M. Tarascon. Towards greener and more sustainable batteries for electrical energy storage. *Nature Chemistry*, 7(1):19–29, Jan 2015. ISSN 1755-4349. doi: 10.1038/nchem.2085. URL `https://doi.org/10.1038/nchem.2085`.

[9] Noshin Omar, Mohamed Daowd, Peter van den Bossche, Omar Hegazy, Jelle Smekens, Thierry Coosemans, and Joeri van Mierlo. Rechargeable Energy Storage Systems for Plug-in Hybrid Electric Vehicles—Assessment of Electrical Characteristics. *Energies*, 5(8):2952–2988, 2012. ISSN 1996-1073. doi: 10.3390/en5082952. URL `https://www.mdpi.com/1996-1073/5/8/2952`.

[10] K.s Jones, Nicholas Rudawski, Isaiah Oladeji, Roland Pitts, and Richard Fox. The State of Solid-State Batteries. *ChemInform*, 43, 11 2012. doi: 10.1002/chin.201247219.

[11] K. Mizushima, P.C. Jones, P.J. Wiseman, and J.B. Goodenough. Li_xCoO_2 $(0 < x \leq 1)$: A new cathode material for batteries of high energy density. *Solid State Ionics*, 3-4:171–174, 1981. ISSN 0167-2738. doi: https://doi.org/10.1016/0167-2738(81)90077-1. URL `https://www.sciencedirect.com/science/article/pii/0167273881900771`.

[12] Tsutomu Ohzuku and Ralph J. Brodd. An overview of positive-electrode materials for advanced lithium-ion batteries. *Journal of Power Sources*, 174(2):449–456, 2007. ISSN 0378-7753. doi: https://doi.org/10.1016/j.jpowsour.2007.06.154. URL `https://www.sciencedirect.com/science/article/pii/S037877530701289X`. 13th International Meeting on Lithium Batteries.

[13] Gerald H. Newman and Lawrence P. Klemann. Ambient Temperature Cycling of an Na-TiS$_2$ Cell. *Journal of The Electrochemical Society*, 127(10):2097, oct 1980. doi: 10.1149/1.2129353. URL `https://dx.doi.org/10.1149/1.2129353`.

[14] D. A. Stevens and J. R. Dahn. High Capacity Anode Materials for Rechargeable Sodium-Ion Batteries. *Journal of The Electrochemical Society*, 147(4):1271, apr 2000. doi: 10.1149/1.1393348. URL `https://dx.doi.org/10.1149/1.1393348`.

[15] Kei Kubota and Shinichi Komaba. *Na-ion batteries*, pages 1–64. John Wiley & Sons, Ltd, 2020. ISBN 9783527610426. doi: https://doi.org/10.1002/9783527610426.bard110019. URL `https://onlinelibrary.wiley.com/doi/abs/10.1002/9783527610426.bard110019`.

[16] Kei Kubota, Naoaki Yabuuchi, Hiroaki Yoshida, Mouad Dahbi, and Shinichi Komaba. Layered oxides as positive electrode materials for Na-ion batteries. *MRS Bulletin*, 39(5):416–422, May 2014. ISSN 1938-1425. doi: 10.1557/mrs.2014.85. URL `https://doi.org/10.1557/mrs.2014.85`.

[17] Samuel Roberts and Emma Kendrick. The re-emergence of sodium ion batteries: testing, processing, and manufacturability. *Nanotechnol Sci Appl*, 11:23–33, June 2018.

[18] Wei Luo, Fei Shen, Clement Bommier, Hongli Zhu, Xiulei Ji, and Liangbing Hu. Na-Ion Battery Anodes: Materials and Electrochemistry. *Accounts of Chemical Research*, 49(2):231–240, 2016. doi: 10.1021/acs.accounts.5b00482. URL `https://doi.org/10.1021/acs.accounts.5b00482`. PMID: 26783764.

[19] Qiannan Liu, Zhe Hu, Weijie Li, Chao Zou, Huile Jin, Shun Wang, Shulei Chou, and Shi-Xue Dou. Sodium transition metal oxides: the preferred cathode choice for future sodium-ion batteries? *Energy Environ. Sci.*, 14:158–179, 2021. doi: 10.1039/D0EE02997A. URL `http://dx.doi.org/10.1039/D0EE02997A`.

[20] K S Novoselov, A K Geim, S V Morozov, D Jiang, Y Zhang, S V Dubonos, I V Grigorieva, and A A Firsov. Electric field effect in atomically thin carbon films. *Science*, 306(5696):666–669, October 2004.

[21] M.R. Al Hassan, A. Sen, T. Zaman, and M.S. Mostari. Emergence of graphene as a promising anode material for rechargeable batteries: a review. *Materials Today Chemistry*, 11:225–243, 2019. ISSN 2468-5194. doi: https://doi.org/10.1016/j.mtchem.2018.11.006. URL `https://www.sciencedirect.com/science/article/pii/S2468519418301745`.

[22] Eunseok Lee and Kristin A. Persson. Li Absorption and Intercalation in Single Layer Graphene and Few Layer Graphene by First Principles. *Nano Letters*, 12(9):4624–4628, 2012. doi: 10.1021/nl3019164. URL `https://doi.org/10.1021/nl3019164`. PMID: 22920219.

[23] Xiaofeng Fan, W.T. Zheng, and Jer-Lai Kuo. Adsorption and Diffusion of Li on Pristine and Defective Graphene. *ACS Applied Materials and Interfaces*, 4(5):2432–2438, 2012. doi: 10.1021/am3000962. URL `https://doi.org/10.1021/am3000962`. PMID: 22536839.

[24] Xiaofeng Fan, W. T. Zheng, Jer-Lai Kuo, and David J. Singh. Adsorption of Single Li and the Formation of Small Li Clusters on Graphene for the Anode of Lithium-Ion Batteries. *ACS Applied Materials and Interfaces*, 5(16):7793–7797, 2013. doi: 10.1021/am401548c. URL `https://doi.org/10.1021/am401548c`. PMID: 23863039.

[25] Yuanyue Liu, Vasilii I. Artyukhov, Mingjie Liu, Avetik R. Harutyunyan, and Boris I. Yakobson. Feasibility of Lithium Storage on Graphene and Its Derivatives. *The Journ of Physical Chemistry Letters*, 4 (10):1737–1742, 2013. doi: 10.1021/jz400491b. URL `https://doi.org/10.1021/jz400491b`. PMID: 26282987.

[26] Shigeki Kawai, Shohei Saito, Shinichiro Osumi, Shigehiro Yamaguchi, Adam S. Foster, Peter Spijker, and Ernst Meyer. Atomically controlled substitutional boron-doping of graphene nanoribbons. *Nature Communications*, 6, 2015. doi: 10.1038/ncomms9098. URL `https://www.scopus.com/inward/record.uri?eid=2-s2.0-84940055190&doi=10.1038%2fncomms9098&partnerID=40&md5=88072320a47c18792f078dc687ed419e`. Cited by: 309; All Open Access, Gold Open Access, Green Open Access.

[27] Haibo Wang, Thandavarayan Maiyalagan, and Xin Wang. Review on Recent Progress in Nitrogen-Doped Graphene: Synthesis, Characterization, and Its Potential Applications. *ACS Catalysis*, 2(5): 781–794, 2012. doi: 10.1021/cs200652y. URL `https://doi.org/10.1021/cs200652y`.

[28] Chun Kiang Chua, Zdeněk Sofer, Bahareh Khezri, Richard D. Webster, and Martin Pumera. Ball-milled sulfur-doped graphene materials contain metallic impurities originating from ball-milling apparatus: their influence on the catalytic properties. *Phys. Chem. Chem. Phys.*, 18:17875–17880, 2016. doi: 10.1039/C6CP03004A. URL `http://dx.doi.org/10.1039/C6CP03004A`.

[29] J. Song, B. Ouyang, and N. V. Medhekar. Energetics and Kinetics of Li Intercalation in Irradiated Graphene Scaffolds. *ACS Applied Materials and Interfaces*, 5(24):12968–12974, 2013. doi: 10.1021/am403685w. URL `https://doi.org/10.1021/am403685w`. PMID: 24256350.

[30] Hao Wu, Zhonglu Guo, Jian Zhou, and Zhimei Sun. Vacancy-mediated lithium adsorption and diffusion on MXene. *Applied Surface Science*, 488:578–585, 2019. ISSN 0169-4332. doi: https://doi.org/10.1016/j.apsusc.2019.05.311. URL `https://www.sciencedirect.com/science/article/pii/S0169433219316198`.

[31] Tomáš Hartman and Zdeněk Sofer. Beyond Graphene: Chemistry of Group 14 Graphene Analogues: Silicene, Germanene, and Stanene. *ACS Nano*, 13(8):8566–8576, 2019. doi: 10.1021/acsnano.9b04466. URL `https://doi.org/10.1021/acsnano.9b04466`. PMID: 31294962.

[32] G. B. Dubrovskii. Crystal structure and electronic spectrum of SnS_2. *Physics of the Solid State*, 40(9):1557–1562, Sep 1998. ISSN 1090-6460. doi: 10.1134/1.1130598. URL `https://doi.org/10.1134/1.1130598`.

[33] Sajedeh Manzeli, Dmitry Ovchinnikov, Diego Pasquier, Oleg V. Yazyev, and Andras Kis. 2D transition metal dichalcogenides. *Nature Reviews Materials*, 2(8):17033, Jun 2017. ISSN 2058-8437. doi: 10.1038/natrevmats.2017.33. URL `https://doi.org/10.1038/natrevmats.2017.33`.

[34] Henan Li, Yumeng Shi, Ming-Hui Chiu, and Lain-Jong Li. Emerging energy applications of two-dimensional layered transition metal dichalcogenides. *Nano Energy*, 18:293–305, 2015. ISSN 2211-2855. doi: https://doi.org/10.1016/j.nanoen.2015.10.023. URL `https://www.sciencedirect.com/science/article/pii/S2211285515004024`.

[35] Tong Jiang and Geoffrey A. Ozin. New directions in tin sulfide materials chemistry. *J. Mater. Chem.*, 8:1099–1108, 1998. doi: 10.1039/A709054D. URL `http://dx.doi.org/10.1039/A709054D`.

[36] C. Bacaksiz, S. Cahangirov, A. Rubio, R. T. Senger, F. M. Peeters, and H. Sahin. Bilayer SnS_2: Tunable stacking sequence by charging and loading pressure. *Phys. Rev. B*, 93:125403, Mar 2016. doi: 10.1103/PhysRevB.93.125403. URL `https://link.aps.org/doi/10.1103/PhysRevB.93.125403`.

[37] Wenping Sun, Xianhong Rui, Dan Yang, Ziqi Sun, Bing Li, Wenyu Zhang, Yun Zong, Srinivasan Madhavi, Shixue Dou, and Qingyu Yan. Two-Dimensional Tin Disulfide Nanosheets for Enhanced Sodium Storage. *ACS Nano*, 9(11):11371–11381, 2015. doi: 10.1021/acsnano.5b05229. URL `https://doi.org/10.1021/acsnano.5b05229`. PMID: 26487194.

[38] Yuan Huang, Eli Sutter, Jerzy T. Sadowski, Mircea Cotlet, Oliver L.A. Monti, David A. Racke, Mahesh R. Neupane, Darshana Wickramaratne, Roger K. Lake, Bruce A. Parkinson, and Peter Sutter. Tin Disulfide—An Emerging Layered Metal Dichalcogenide Semiconductor: Materials Properties and Device Characteristics. *ACS Nano*, 8(10):10743–10755, 2014. doi: 10.1021/nn504481r. URL `https://doi.org/10.1021/nn504481r`. PMID: 25247490.

[39] Peter Woulfe. Experiments to shew the nature of Aurum mosaicum. *Philosophical Transactions of the Royal Society of London*, 61:114–130, 1771. doi: 10.1098/rstl.1771.0015. URL `https://royalsocietypublishing.org/doi/abs/10.1098/rstl.1771.0015`.

[40] D.L. Greenaway and R. Nitsche. Preparation and optical properties of group IV–VI2 chalcogenides having the CdI2 structure. *Journal of Physics and Chemistry of Solids*, 26(9):1445–1458, 1965. ISSN 0022-3697. doi: https://doi.org/10.1016/0022-3697(65)90043-0. URL `https://www.sciencedirect.com/science/article/pii/0022369765900430`.

[41] Lawrence E. Conroy and Kyu Chang Park. Electrical properties of the Group IV disulfides, titanium disulfide, zirconium disulfide, hafnium disulfide and tin disulfide. *Inorganic Chemistry*, 7(3):459–463, 1968. doi: 10.1021/ic50061a015. URL `https://doi.org/10.1021/ic50061a015`.

[42] H.P.B. Rimmington, A.A. Balchin, and B.K. Tanner. Nearly perfect single crystals of layer compounds grown by iodine vapour-transport techniques. *Journal of Crystal Growth*, 15(1):51–56, 1972. ISSN 0022-0248. doi: https://doi.org/10.1016/0022-0248(72)90319-3. URL `https://www.sciencedirect.com/science/article/pii/0022024872903193`.

[43] N.G. Deshpande, A.A. Sagade, Y.G. Gudage, C.D. Lokhande, and Ramphal Sharma. Growth and characterization of tin disulfide (SnS_2) thin film deposited by successive ionic layer adsorption and reaction (SILAR) technique. *Journal of Alloys and Compounds*, 436(1):421–426, 2007. ISSN 0925-8388. doi: https://doi.org/10.1016/j.jallcom.2006.12.108. URL `https://www.sciencedirect.com/science/article/pii/S0925838806022444`.

[44] Chuanxin Zhai, Ning Du, and Hui Zhang Deren Yang. Large-scale synthesis of ultrathin hexagonal tin disulfide nanosheets with highly reversible lithium storage. *Chem. Commun.*, 47:1270–1272, 2011. doi: 10.1039/C0CC03023F. URL `http://dx.doi.org/10.1039/C0CC03023F`.

Chapter 2

Literature review

The intercalation of lithium, as well as similar alkali metals, onto pristine SnS_2, has been studied extensively in the effort to find viable alternatives to the existing commercial LIB electrode materials. The SnS_2 monolayer is suitable for use as an anode material, and performs better than graphite with regards to storage capacity in particular. While tin disulfide has a history of study into the 1700's, only in the last few decades has battery technologies developed to the point where alternative materials needed to be considered. In this chapter, several examples of experimental and computational studies into the application of SnS_2 in battery technologies are reviewed. Following a review of pristine SnS_2 studies, we go on to review studies that have also introduced doping, layering, and vacancy defects.

2.1   Alkali metals on the pristine SnS_2 monolayer

A 1991 Bronold *et al.* article studied the intercalation of alkali metals, in particular sodium and potassium, into SnS_2.[1] This intercalation was studied following atom deposition in ultra high vacuum conditions, using multiple methods of spectroscopy (ultraviolet photoelectron, X-ray photoelectron and ion scattering), as well as low energy electron diffraction. When Na is deposited onto SnS_2 surfaces and intercalates, the new phase of semiconducting Na_xSnS_2, with the x concentration value being a measurement of the capacity of the surface, is influenced by the quality of the crystal surface and environmental conditions. The primary factors determining Na concentration are the activation barrier and the concentration of defects in the SnS_2 lattice.

Schellenberger *et al.* 1991 results for Na adsorption on layered SnS_2 semiconductors revealed a change in the valence band with an increase in sodiation.[2] The deposited Na inserted into the SnS_2 substrate lattice, and consequently no binding energy shifts due to contact formation was observed. The observed results corresponded closely with the intercalation of Cu in an SnS_2 substrate. The article also makes a comparison with similarly obtained results for an WSe_2 substrate, which in turn did experience binding energy shifts. The difference can be attributed to the energy bands, with SnS_2 having p orbital bands near valence band edge for the S atoms, and s orbital bands near the conduction band edge for the Sn atoms. On the other hand, WSe_2 only has band edges attributed to weakly bonding d-states of the W atom.

Studying amorphous and crystalline SnS_2 structures, Momma *et al.* found that the temperature at annealing influenced the storage capacity of the material for Li-ions.[3] Following annealing at 400 °C,

SnS$_2$ doubled its initial capacity measurement from 300 mAh/g to 600 mAh/g. Additionally it is shown that using SnS$_2$ as an anode in LIBs with a LiCoO$_2$ cathode is possible. Although the study focuses on bulk SnS$_2$, annealing has been shown to display similar improvements to material properties in TMDs. MoS$_2$ displays more uniform structural properties up to annealing temperature of 300 °C, after which cracking occurs along grain boundaries.

Following up on the former study, Mukaibo *et al.* considered the annealing of SnS$_2$ structures as small as 30 nm across.[4] The smaller SnS$_2$ particles displayed higher storage capacity along with improved cycling ability; the initial discharged capacity was measured at 620 mAh/g for a constant discharge current. The difference in surface area would facilitate Li-ion diffusion through the material during charge and discharge. Furthermore, annealing improved storage capacity further, increasing it to 736 mAh/g. The increase possibly results from structural changes following annealing, prompting further investigation.

In 2007, Kim *et al.* synthesized SnS$_2$ nanosheets for application as an LIB anode material.[5] The obtained nanosheets had a thickness of approximately 2 nm, with the resulting charge-capacity measuring 323 mAh/g. Hence, 95% of this capacity was retained after 50 cycles discharging from 1.5 V to 0 V. Kim *et al.* also looked at variations in the nanosheet thickness, up to 26 nm, and repeated charge-capacity measurements. This investigation of the nanostructure during charge/discharge cycling concluded that the thinner SnS$_2$ nanosheets displayed more advantageous reaction kinetics (lower diffusion barriers and improved ion mobility). Only nanosheets with a thickness below 10 nm retained over 90% of the maximum charge capacity after 50 cycles.

The voltage profile of an SnS$_2$ electrode, as analyzed by Seo *et al.* in 2018, shows a shoulder (turn) at 0.35 V, and begins to plateau at 1.21 V.[6] These voltages in particular are visible during the initial charge cycle, and are characteristic of irreversible and reversible charge capacities. During Li intercalation, SnS$_2$ decomposes into Sn and Li$_2$S. Following Li saturation, a Li-Sn alloy will form. This behaviour should limit the discharge capacity, although the initial subsequent discharge capacity was measured at 645 mAh/g, close to the maximum theoretical capacity. The discharge capacity remains fairly stable and reversible up to 30 cycles. The average discharge capacity measured at 583 mAh/g, 90% of the maximum theoretical capacity. This result is significantly greater than the average commercial graphite electrode storage capacity of 372 mAh/g. After 30 cycles, it was determined that 85% of the maximum theoretical capacity was retained. The enhanced electrochemical properties of SnS$_2$ nanocrystals can be attributed to the 2D layered characteristics. These factors help facilitate Li-ion diffusion and decrease excess voltages during Li-Sn alloying reactions. Seo *et al.* concludes that the electrode offers faster reactions, higher charge/discharge capacity and improved cycling stability.[6]

A 2010 DFT study of monolayer SnS$_2$ nanoribbons attempts to predict the stability and electronic properties of the material.[7] It is determined that monolayer SnS$_2$ acts as a nonmagnetic semiconductor, with its band gap decreasing monotonically as the ribbon width is increased. Considering the calculated formation energy, the wider SnS$_2$ nanoribbons, thus closer in structure to monolayer SnS$_2$ nanosheets, displayed a greater stability than the narrowest nanoribbons. The large-scale synthesis of ultrathin SnS$_2$ nanosheets, with thickness under 5 nm, is detailed in a 2011 Zhai *et al.* article.[8] Once again, thinner SnS$_2$ nanosheets showed improved reversible storage capacity and capacity retention of Li-ions, with 96% capacity being retained after 50 cycles, another improvement over earlier studies (and a significant improvement over graphite[9]). In general, this improvement in performance observed for thinner SnS$_2$

nanosheets can be attributed to the well-defined nanostructure, and is encouraging for anode material application in next generation LIBs.

The synthesis of SnS_2 thin films was improved by the development of an L-cysteine-assisted hydrothermal method by Zhong *et al.* in 2012.[10] The synthesized SnS_2 films are built onto Sn foil, with a thickness of two to five atomic layers. The resultant ultrathin SnS_2 nanosheet demonstrated a discharge capacity of 690 mAh/g. Described as graphene-like, the SnS_2 material also demonstrated enhanced photoelectrical properties, such as high photosensitivity and thermal stability.

As previously stated, NIBs can be considered as alternatives to LIBs due to the abundance of sodium. However, the application of NIBs is hindered by low capacity, and poor rate capability cycling stability of commercial anodes for sodiation. In 2015, Sun *et al.* investigated the SnS_2 nanosheets of 3 to 4 nm in thickness for application in NIBs.[11] High Na-ion mobility is exhibited, suggesting fast sodiation reactions. The SnS_2 nanosheets display a reversible Na storage capacity of 733 mAh/g at 0.1 A/g, while at a high current density of 2.0 A/g the capacity is 435 mAh/g. After 50 cycles, 88% of the reversible storage capacity is retained, far better than other pristine SnS_2 structures. Thus, nanosheet morphology is a benefit to cycling stability. The overall performance and electrochemical performance shows considerable potential for SnS_2 nanosheets as anodes for NIBs.

Comparing the Li storage mechanisms of RuO_2, SnO_2 and SnS_2 as anode materials for LIBs, Hassan *et al.* found that lithium adsorption still occurs beyond a conversion reaction limit.[12] Beyond this limit, SnO_2 and SnS_2 allow for additional Li adsorption through alloying reactions, although a contribution to additional storage also comes from interfacial storage. The latter mechanism is also present for RuO_2 lithiation, and appears to be a universal high-capacity storage mechanism in both TMDs and metal oxides. Of the three materials tested, SnS_2 showed the least volume expansion as result of lithiation, which in turn suggests a smaller degree of anode pulverization with repeated long-term cycling.

Huang *et al.* investigates monolayer SnS_2 as an anode for LIBs, focusing on the mechanisms undergone during charge/discharge.[13] The initial conversion process of SnS_2 with Li will form Li_2S. This product is electrochemically inactive, and in turn this conversion reaction is irreversible, limiting the storage capacity and in turn the potential application of SnS_2 in LIBs. The conversion reaction can be counteracted with the introduction of molybdenum (Mo) as a catalyst in SnS_2. The Mo catalyst promotes reversible reactions, allowing Sn to react with Li_2S to reform SnS_2.

Having discussed both LIBs and NIBs with SnS_2 as an anode material, an additional alkali metal often considered as charge carrier is potassium (K). Monolayer SnS_2 reacts to the insertion of K similarly to the insertion of Li and Na, as observed by Rehman *et al.* in their DFT study on the topic.[14] SnS_2 gains improved metallic properties upon K insertion, with electronic conductivity increasing as the K concentration increases. A low average open circuit voltage of 0.84 V was measured from the binding energy between K-ions and the monolayer SnS_2, which was on par commercial anode materials, and a very low diffusion barrier of 0.054 eV was measured for K diffusion. Overall, Rehman *et al.* showed that SnS_2 is suitable as an anode material for KIBs.

A more recent 2021 study by Anlin Lazar *et al.* goes into more detail on the effect of annealing on the structural properties of SnS_2 thin films.[15] The synthesized SnS_2 films were fabricated via a bi-stage process, involving of tin precursor thermal evaporation followed by sulfur annealing. Annealing takes 0.5 to 3 hours, occurring at temperatures ranging from 300 °C to 500 °C. The lower temperature resulted

in improved crystallinity in the fabricated SnS_2 thin films, while for higher temperatures nanocrystalline SnS_2 phases are observed. While annealing in general will decrease the optical band gap, this effect is more pronounced for higher annealing temperatures.

2.2 Deficiencies of the pristine SnS_2 monolayer

2D nanomaterials such as graphene and transition metal dichalcogenides (TMD), regardless of their excellent properties are known to easily restack and condense, reforming a bulk material which weakens the performance and properties initially desired. Tin disulfide also displays this restacking problem, which deters the reversible capacity of the material in LIBs or NIBs. SnS_2 is attractive over graphite and graphene-like materials in large part due to the high storage capacity the material initially offers as an anode, however, this capacity is hindered by poor initial reversibility.[16,17]

The drawbacks of the SnS_2 electrode also include low electronic conductivity, slow charge transfer and poor cycling stability, the latter being a consequence of the large volume expansion. As previously stated, the storage mechanism of Li on SnS_2 involves a conversion reaction, which is the decomposition of SnS_2 into metallic Sn, and an alloying process, which forms the alloy $Li_{4.4}Sn$. Large irreversible capacity is observed in first cycle due to the conversion reaction, as a large portion of Li-ions cannot be reused. The alloying/dealloying mechanism drives most electrochemical activity in the SnS_2 electrode, but is the source of the large volume expansion and long-term pulverization, which will cause storage capacity and performance to deteriorate. These observations are confirmed by results obtained by Wei *et al.* in 2018, along with additional deficiencies of the SnS_2 monolayer. The solid electrolyte interphase displays poor stability, which can be minimized through treatment prior to any lithiation. This problem is also solved through a better understanding of Li reaction mechanisms. A more difficult issue is the high voltage barrier, which inhibits reversible storage capacity. This is due to the charge and discharge cycles not having the same maximum voltage, leading to voltage inefficiency during initial cycling. As an example, the SnS_2/graphene composite has a 0.3 V difference, unacceptable in commercial LIBs.[11,18,19]

2.3 Improving the SnS_2 monolayer for energy storage

There is an ongoing effort to improve the energy density, power density, battery cycle life and cycling stability for the application of the SnS_2 monolayer as an anode material. Various methods can be undertaken to alter the properties of a 2D material, the most significant of which being doping, homogeneous or heterogeneous stacking layering, and vacancy defects.

2.3.1 Doping

Preferably, doping introduces elements that will interact well with Li or Na adatoms, aiding both adsorption and binding energy, as well as diffusion. The dopants will often introduce more efficient diffusion paths in the material, although a variety of additional effects have been observed. Depending on the charge of the dopant, the electronic structure of SnS_2 can be altered significantly.

From first-principles calculations, Xia *et al.*[20] investigated the change in characteristics of monolayer SnS_2 nanosheets following n- and p-type doping in 2014. Multiple group 5 and group 7 elements were

substituted in place of S atoms, including N, P and As, and F, Cl, Br and I, respectively. The investigation revealed that substituting group 5 atoms resulted in high formation energies paired with deep transition levels, indicative of ineffective p-type carriers in the SnS_2 monolayer following doping. In contrast, group 7 atoms have low formation energies and shallow transition levels. Group 7 substitution acts as effective n-type dopants for monolayer SnS_2. Looking at more specific examples, F atoms are the most effective n-type dopants, with the lowest formation energy. An additional result obtained shows that all doped SnS_2 nanosheets favour Sn-rich conditions (either high S-vacancy concentration, or low Sn-vacancy concentration), and that the nanosheet stability depends on the atomic size of dopants. The investigation concludes by suggesting future studies consider similar n- and p-type doping of monolayer SnS_2. An additional source shows that Cl or I doping of SnS_2 does not influence the mechanisms of interatomic interactions.[21] The bonding that occurs between Sn atoms and the dopants (Cl, I), will form between p-orbitals of both Sn and the dopants. No bonding occurs between the dopants and S atoms.

A study on Ce doping of SnS_2 shows that Li diffusivity or mobility during lithiation is negatively impacted. The 2015 Liu *et al.* study used first-principle calculations to evaluate pristine and modified SnS_2 as an anode material for LIBs.[22] In addition to affecting ion mobility, volume expansion was also observed following the substitution of an Sn atom by a Ce atom. This expansion lowered the formation energy, as the increased volume facilitated Li atom intercalation. Interaction between the Li atom and Ce dopant was also confirmed after comparison of the density of states of the pristine and Ce-doped SnS_2. In addition, the expansion lowered the diffusion barrier along the prefered paths of interstitial Li atoms. However, the interaction between Li atoms and Ce dopant are strong enough to limit the benefit of a reduced diffusion barrier, thus the negative impact to ion mobility.

Liu *et al.* attributes the improvements in the performance of Ce-doped SnS_2 anodes for LIBs to the Ce^{3+}-ion. Their 2019 DFT study calculates the structural stability and electronic and magnetic properties of both a pristine and Ce-doped SnS_2 monolayer.[23] The larger ionic radius of Ce^{3+} offers increased lattice space for Li^+, in agreement with experimental results. Liu *et al.* has overall confirmed experimental observations regarding the positive influence of intrinsic defects in SnS_2.

The use of iron as a dopant for SnS_2 has often been considered due to the opportunity of introducing ferromagnetic properties into the material. A 2017 Li *et al.* study has an Fe-doped monolayer obtained through exfoliation via micromechanical cleavage.[24] Pure SnS_2 is diamagnetic, while the inclusion of Fe doping at Sn sites will induce ferromagnetism with a Curie temperature of 31 K. DFT calculations revealed that the Fe-doped SnS_2 monolayer is energetically stable, and can be applied in nanoelectronic or magnetic applications.

Specific metals, in particular transition metals from groups V to VIII, can be introduced into monolayer SnS_2 as dopants, in order to magnetize the material. These and similar dopants undergo DFT investigation in a 2021 study by Zhan *et al.*.[25] Beyond transition metals, the influence of studied dopants were categorized into one of two groups. Nonmetal atoms resulted in both p-type and n-type carriers. Metal atoms beyond transition metals could only result in p-type doping. On average, it was observed that transition metals resulted in higher binding energies.

A 2020 Ullah *et al.* article reports on five different dopants for monolayer SnS_2, that all induce changes for the spin-up and spin-down states, and in turn introduces magnetic semiconductor behaviour.[26] The dopants were V, Co, Mo, W and Re, as well as O, Se and Te for a different set of results. All the doped

systems remain semiconducting while the band gap is influenced. Of the dopants, the bond length between O and Sn is the smallest, corresponding to a higher bond energy, and in turn increasing the band gap. In the case of Mo-doped SnS_2, there is an observable asymmetry surrounding the Fermi energy, indicating that spin polarized states were induced. Dopants are more easily incorporated onto an S atom site for an Sn-rich environment, thus doping is improved by the presence of S-vacancies.

2.3.2 Heterogeneous layering

Heterogeneous layering often attempts to combine the best properties of multiple materials while also shoring up deficiencies. In the case of SnS_2 as an anode, one of the largest benefits of heterogeneous layering (or compositing/hybridization in general) is the prevention of pulverization during cycling. This requires enhancement of the structural stability of SnS_2, which is easily achieved by anchoring the monolayer with a substrate surface or structure.

A facile solution-phase method for preparing few-layer SnS_2/graphene (SnS_2/G) was developed by Chang *et al.* in 2012.[27] For the sulfide source and reducing agent, the process employs l-cysteine. The resultant SnS_2/G hybrid underwent X-ray diffraction (XRD), scanning electron microscopy (SEM), and high-resolution transmission electron microscopy (HRTEM) for characterization. These techniques and electrochemical tests demonstrate that SnS_2/G has an excellent storage capacity of 920 mAh/g accompanied by high cycling stability and high-rate capability. In addition, the incorporated graphene has improved electric conductivity and electron mobility. Overall, the improved properties are attributable to the synergy of complementary interactions between the layered SnS_2 and graphene. These experimental results suggest that SnS_2/G offers great potential for LIBs for high performance devices, while also avoiding the poor electronic conductivity and unstable cycling common to metal oxide/graphene composites.

Another SnS_2/G nanosheet composite is synthesized through chemical modification of graphene oxide and subsequent hydrothermal treatment, as designed by Sathish *et al.* in 2012.[28] Following SEM and TEM analysis, SnS_2 nanoparticles can be seen embedded into a graphene surface of 2 nm thickness. The SnS_2 nanoparticles will inhibit graphene restacking while also facilitating Li-ion diffusion across the surface, enhancing both cycling performance and reversible storage capacity. The nanosheet structure allows for electrolyte contact with the entire surface of composite materials and reduces Li-ion diffusion paths further. Overall, the Li-ion storage capacity measured for SnS_2/G is much higher for initial cycles. For less than 40 cycles, SnS_2/G has a higher reversible capacity of 584 mAh/g, falling only slightly to 577 mAh/g after 50 cycles.

A 2013 paper by Li *et al.* reported on SnS_2 nanosheets acting as anchor for mesoporous carbon (MC/SnS_2), resulting in the integration of both TMDs and porous carbon characteristics.[29] As an anode for LIBs, the unique structure of the MC/SnS_2 nanoscale composite allows for significantly improved cycling stability and high rate capability when compared with pristine SnS_2. The initially measured MC/SnS_2 storage capacity of 1552.9 mAh/g falls slightly below the measured pristine SnS_2 storage capacity of 1602.8 mAh/g, as a result of the MC matrix having been introduced. The storage capacity retention much higher, a direct result of increased cycling stability. After 50 cycles, MC/SnS_2 retains 64.4% of the reversible discharge capacity, resulting in a stable discharge capacity of 428.8 mAh/g. In comparison, pristine SnS_2 only retained a stable discharge capacity of 282.2 mAh/g after 50 cycles.

Qu *et al.* developed a layered SnS_2/reduced graphene oxide (SnS_2/RGO) composite as an anode

for NIBs in 2014. As an anode, the composite material demonstrated an exceptional storage capacity of 630 mAh/g at 0.2 A/g. Increasing the charge rate to 2 A/g still maintained good performance and capacity of 544 mAh/g. As for long term cycling stability, 84% of the initial storage capacity is retained after 400 cycles (500 mAh/g at 1 A/g). Qu *et al.* attributed the improved electrochemical performance to the layered SnS_2 structure, which better accommodates volume changes resulting from Na insertion.[30] The inclusion of RGO increased both mechanical resilience, limiting anode pulverization, and electronic conductivity.

A theoretical DFT investigation of the monolayers SnS, SnS_2, and their composite double layer was reported on by Lorenz *et al.* in 2014, discussing various electronic and structural properties.[31] The investigation made use of density-functional tight binding (DFTB) to approximate a large system consisting of several hundred atoms. The monolayer structures were compared with their corresponding bulk structures, revealing that the band gaps were larger for the former in all cases. Additionally, the band gaps corresponded well with experimental results. The structure of the SnS/SnS_2 double layer forms in a consistent manner, regardless of dispersion interactions between the monolayers. The DOS of SnS/SnS_2 shows additional S atom p states as well as Sn atom s and p states, which originates from the SnS monolayer. The transferred state indicates charge transfer has occurred from SnS_2 to SnS. This additional interaction results in increased stability for the double layer.

The application of a SnS_2/RGO composite as anode for NIBs is investigated again by Zhang *et al.*, with a focus placed on using few-layer SnS_2 for a resulting thickness under 4 nm.[32] Synthesis made use of a solvothermal method. The composite material undergoes more extensive testing for cycling stability. At 0.1 A/g, the yielded charge capacity is 649 mAh/g, while at a higher rate of 0.8 A/g, the charge capacity is 469 mAh/g. The latter result can be retained for up to 61% effectiveness after 1000 cycles. The highest rate tested (12.8 A/g) had the composite charge to full in 1.3 minutes, although only delivering a charge capacity of 337 mAh/g. Overall, the SnS_2/RGO composite offers excellent storage capacity and ultralong cycle life, along with excellent rate capability, and is a fast and stable anode for NIBs.

A carbon nanotube (CNT) and SnS_2 nanoparticle composite was prepared via hydrothermal methods by Guan *et al.* in 2015.[33] The addition of conductive CNTs alters the SnS_2 structural morphology. SnS_2 crystal growth is restrained, resulting in the 2D SnS_2/CNT composite, which can grow to form a porous 3D structure with enlarged surface area. Li-ion transfer paths are shortened and offer less resistance, and the SnS_2 work in concert with the CNT matrix to speed up electronic diffusion while also limiting pulverization as a result of volume change during charge/discharge. In summary, the SnS_2/CNT composite shows improved cyclability and rate performance for LIBs when compared to a pristine SnS_2 anode.

A consequence of the restacking problem in SnS_2 is poor reversible capacity and cycling stability. Balogun *et al.* attempts to address this problem in 2015, through the strengthening of a SnS_2 nanosheet by growing it onto a vanadium nitride (VN) substrate.[17] This resultant VN/SnS_2 has an initial reversible capacity of 75% of the specific capacity of 819 mAh/g, for a current density of 0.65 A/g. This stabilizes to a capacity of 791 mAh/g after 100 cycles, retaining 97%. Storage capacity is still acceptable for a high rate current density of 13 A/g, measured at 349 mAh/g after 70 cycles. Balogun *et al.* states that the improved performance results from the support provided by VN, which has also provided Li-ion diffusion shortcuts, while also improving mechanical and structural stability.

In 2016, Youn *et al.* discusses a variation on the SnS_2/RGO composite, with the conductive RGO

having an N dopant.[19] The NRGO layer will cushion against expansion stressors present during lithiation of SnS$_2$. Noncycling Li$_2$S will still form, although the composite helps increase the ion mobility between S and Sn atoms, as Li-ions will rapidly transfer from Li$_2$S and Li$_x$Sn. Overall, the SnS$_2$/NRGO composite will retain a storage capacity of 562 mAh/g after 200 cycles for a current density of 0.2 A/g.

Expanding on the study by Huang *et al.* in section 2.1, the Mo catalyst was utilized as part of a heterogeneous nanostructure of MoS$_2$ grown onto SnS$_2$ nanosheets while anchored by 3D graphene.[13] The resultant composite (SnS$_2$/MoS$_2$/3DG) has significantly enhanced electrochemical properties. Coulombic efficiency, the efficiency of charge transfer, was measured at 81.5%, with the initial discharge capacity measured at 960.5 mAh/g for a current density of 0.05 A/g, and 495.6 mAh/g for 1.0 A/g. Following cycling, TEM and X-ray photoelectron spectroscopy (XPS) analysis verified reversible conversion reactions in the composite as result of the Mo catalyst. This method confirms the potential of alloying reactions for SnS$_2$ and similar TMDs in high energy density LIBs.

More recently, Liu *et al.* tested the SnS$_2$/RGO composite for application as an LIB anode.[34] The 2022 study found that van der Waals interactions between the SnS$_2$ and RGO nanosheets resulted in close coupling, which in turn provides efficient ion diffusion paths for exceptional electrical conductivity along with buffering the layers during volume expansion. The SnS$_2$/RGO composite retains a Li storage capacity of 840 mAh/g after 120 cycles for a current density of 0.2 A/g. For a current density of 1.0 A/g, this retained storage capacity has decreased to 450 mAh/g after 1000 cycles. XRD analysis shows that SnS$_2$/RGO initially undergoes intercalation, conversion, and lastly alloying reaction during the extent of the first discharge cycle, while subsequent charge/discharge cycles largely consists of alloying/dealloying reactions.

2.3.3   Vacancies

The introduction of a vacancy defect in the SnS$_2$ monolayer, particularly as an anode material has been explored experimentally, with many observations verified with DFT calculations. S-vacancies have in general been explored in more detail, which Sn-vacancies often being considered less desirable.

A DFT investigation of an S-vacancy SnS$_2$ monolayer by Zhao *et al.* determined the reaction of adsorbed small gas molecules within the vicinity of the S-vacancy.[35] Of the tested molecules, H$_2$O and CO were physically adsorbed on the monolayer, which is to say the adsorption energy for these molecules was low, measuring below 0.2 eV. In comparison, the molecules of NH$_3$, NO, and NO$_2$ where chemically adsorbed, which is characterized by higher adsorption energies which likely indicate the presence of strong covalent bonding. Additional analysis determined that H$_2$O and NH$_3$ were charge donors, while the remaining gas molecules (CO, NO, NO$_2$) acted as charge acceptors. The different reactions of adsorption with respect to common gas molecules are useful for the application of S-vacancy SnS$_2$ monolayers in chemical sensors and similar electrical devices. An additional result of the study determined that the adsorption energies and charge transfer is also adjustable, following the application of bi-axial strain on the substrate.

A 2018 Bletskan & Frolova investigation of the influence defects on the electronic structure of 2H-SnS$_2$ confirmed changes as result of vacancies.[21] These changes include defective states forming in the band gap. For an Sn-vacancy (V_{Sn}), this occurs at the acceptor level of the band gap, separated 0.3 eV from the valence band maximum. Specifically, there is a change in the electronic states nearby V_{Sn}, with parts

of the 3p-states being transferred out towards the vacancy location. This results in a down shift of the Fermi level, while the density of states near E_F increases. For an S-vacancy, the donor level is separated from the conduction band minimum by 0.47 eV.

When considering the application of doping in conjunction with an S-vacancy in 2019, Liu *et al.* found that the most stable SnS_2 monolayer configuration had the 2Ce atom dopants located near V_S.[23] Existing experimental observations show that the presence of V_S turns grown SnS_2 samples into *n*-type semiconductor. The conjecture follows that there are factors which influence the dopant ionic state in doped SnS_2 nanosheets. A DFT investigation of introducing a Ce dopant onto monolayer SnS_2 clarified this information, showing that the Ce^{4+} dopant has undergone reduction, forming Ce^{3+} instead, under the influence of V_S.

Looking at a variant structure consisting of SnS_2 nanosheets, SnS_2 microspheres with an S-vacancy can be synthesized via a solvothermal process, as reported by Wang *et al.* in 2020.[36] SnS_2 in general often makes use of TAA, the amount of which controls the SnS_2 morphology as well as the V_S concentration. Wang *et al.* also investigates the SnS_2 microspheres via DFT calculations, determining that introducing V_S has decreased the band gap. As consequence, the SnS_2 microspheres display exceptional Na storage performance, providing a storage capacity 486 mAh/g at a charge rate of 1 A/g, even after 1000 cycles.

A post thermal treatment of interlayer expanded SnS_2 nanosheets will convert the material to hexagonal SnS_2 and orthorhombic SnS nanosheets with high S-vacancy concentration through the simple attunement of heating temperature.[18] The abundance of S-vacancies were achieved during phase conversion. Additionally, the process improved Li-ion diffusion mobility, electronic conductivity and the number of active sites, while reducing resistance to interfacial charge transfer. Overall, the S-vacancy rich SnS_2 nanosheets were significantly improved for application in LIBs.

The influence on the magnetic properties of monolayer SnS_2 following the introduction of vacancy defects is briefly discussed in a 2020 Ullah *et al.* article.[26] The pristine SnS_2 monolayer has no magnetic moment. Following the introduction of an S-vacancy, beyond defect levels in the band gap, there is no observed change in electromagnetic properties. Introducing the Sn-vacancy also tunes the band gap, but will also induce a magnetic ground state with a measured magnetic moment of 4.00 μB, resulting in a magnetic semiconductor monolayer SnS_2. As an aside, Ullah *et al.* observes that S- and Sn-vacancies display relatively high vacancy migration barriers, which reduces the possibility of vacancy clustering.

A recent DFT investigation of SnS_2 with high S-vacancy concentration by Huang *et al.* determined that vacancies can change the band gap to enhance electronic conductivity.[37] The investigation expands on the hydrothermal synthesis of binder-free SnS_2 with high S-vacancy concentration onto carbon paper (CP), which performed better than comparable SnS_2 powders as an anode for LIBs. SnS_2/CP delivered a stable (after 60 cycles) charge storage capacity of 2073.8 mAh/g at a current density of 0.2 A/g and 1545.7 mAh/g at 0.8 A/g, over fives times the capacity measured for SnS_2 powders. The composite material also performs exceptionally at high rates, delivering a charge capacity of 1020.2 mAh/g at a current density of 2.0 A/g.

2.4 Room for improvement

To a large degree, previous investigations have focused more on the inclusion of dopants of layering over vacancies for the engineering of the electronic properties of SnS_2. DFT studies analyzing different electrochemical properties of Li adatoms at different sites in the vicinity of the vacancy are available in abundance. In comparison, study of Na adatoms on the SnS_2 monolayer is much scarcer, especially on diffusion barriers. We will be expanding upon the research available for both S- and Sn-vacancies in SnS_2. The investigation is approached via density functional theory along with Hubbard U and dispersion corrections. A pristine or defective SnS_2 monolayer supercell will be simulated, after which the simulation undergoes self-consistent field calculations so as to determine the total energy. Subsequently, structural and electronic properties will be derived to determine various electrochemical properties.

Bibliography

[1] M. Bronold, C. Pettenkofer, and W. Jaegermann. Alkali metal intercalation into SnS_2. *Applied Physics A*, 52(3):171–179, Mar 1991. ISSN 1432-0630. doi: 10.1007/BF00324413. URL `https://doi.org/10.1007/BF00324413`.

[2] A Schellenberger, R Schlaf, T Mayer, E Holub-Krappe, C Pettenkofer, W Jaegermann, U.A Ditzinger, and H Neddermeyer. Na adsorption on the layered semiconductors SnS_2 and WSe_2. *Surface Science*, 241(3):L25–L29, 1991. ISSN 0039-6028. doi: https://doi.org/10.1016/0039-6028(91)90083-5. URL `https://www.sciencedirect.com/science/article/pii/0039602891900835`.

[3] Toshiyuki Momma, Nobuhiro Shiraishi, Atsuhito Yoshizawa, Tetsuya Osaka, Aharon Gedanken, Junjie Zhu, and Lena Sominski. SnS_2 anode for rechargeable lithium battery. *Journal of Power Sources*, 97-98:198–200, 2001. ISSN 0378-7753. doi: https://doi.org/10.1016/S0378-7753(01)00723-6. URL `https://www.sciencedirect.com/science/article/pii/S0378775301007236`. Proceedings of the 10th International Meeting on Lithium Batteries.

[4] Hitomi Mukaibo, Atsuhito Yoshizawa, Toshiyuki Momma, and Tetsuya Osaka. Particle size and performance of SnS_2 anodes for rechargeable lithium batteries. *Journal of Power Sources*, 119-121: 60–63, 2003. ISSN 0378-7753. doi: https://doi.org/10.1016/S0378-7753(03)00125-3. URL `https://www.sciencedirect.com/science/article/pii/S0378775303001253`. Selected papers presented at the 11th International Meeting on Lithium Batteries.

[5] Tae-Joon Kim, Chunjoong Kim, Dongyeon Son, Myungsuk Choi, and Byungwoo Park. Novel SnS_2-nanosheet anodes for lithium-ion batteries. *Journal of Power Sources*, 167(2):529–535, 2007. ISSN 0378-7753. doi: https://doi.org/10.1016/j.jpowsour.2007.02.040. URL `https://www.sciencedirect.com/science/article/pii/S037877530700448X`.

[6] Jung-wook Seo, Jung-tak Jang, Seung-won Park, Chunjoong Kim, Byungwoo Park, and Jinwoo Cheon. Two-Dimensional SnS2 Nanoplates with Extraordinary High Discharge Capacity for Lithium Ion Batteries. *Advanced Materials*, 20(22):4269–4273, 2008. doi: https://doi.org/10.1002/adma.200703122. URL `https://onlinelibrary.wiley.com/doi/abs/10.1002/adma.200703122`.

[7] Linze Li, Hong Li, Jing Zhou, Jing Lu, Rui Qin, Zhengxiang Gao, and Wai Ning Mei. Electronic Structure and Stability of Ultranarrow Single-Layer SnS_2 Nanoribbons: A First-Principles Study. *Journal of Computational and Theoretical Nanoscience*, 7(10):2100–2103, 2010. ISSN 1546-1955. doi: doi:10.1166/jctn.2010.1590. URL `https://www.ingentaconnect.com/content/asp/jctn/2010/00000007/00000010/art00040`.

[8] Chuanxin Zhai, Ning Du, and Hui Zhang Deren Yang. Large-scale synthesis of ultrathin hexagonal tin disulfide nanosheets with highly reversible lithium storage. *Chem. Commun.*, 47:1270–1272, 2011. doi: 10.1039/C0CC03023F. URL `http://dx.doi.org/10.1039/C0CC03023F`.

[9] Sid Megahed and Bruno Scrosati. Lithium-ion rechargeable batteries. *Journal of Power Sources*, 51(1):79–104, 1994. ISSN 0378-7753. doi: https://doi.org/10.1016/0378-7753(94)01956-8. URL `https://www.sciencedirect.com/science/article/pii/0378775394019568`.

[10] Haoxiang Zhong, Gongzheng Yang, Huawei Song, Qingyu Liao, Hao Cui, Peikang Shen, and Cheng-Xin Wang. Vertically Aligned Graphene-Like SnS_2 Ultrathin Nanosheet Arrays: Excellent Energy Storage, Catalysis, Photoconduction, and Field-Emitting Performances. *The Journal of Physical Chemistry C*, 116(16):9319–9326, 2012. doi: 10.1021/jp301024d. URL `https://doi.org/10.1021/jp301024d`.

[11] Wenping Sun, Xianhong Rui, Dan Yang, Ziqi Sun, Bing Li, Wenyu Zhang, Yun Zong, Srinivasan Madhavi, Shixue Dou, and Qingyu Yan. Two-Dimensional Tin Disulfide Nanosheets for Enhanced Sodium Storage. *ACS Nano*, 9(11):11371–11381, 2015. doi: 10.1021/acsnano.5b05229. URL `https://doi.org/10.1021/acsnano.5b05229`. PMID: 26487194.

[12] Ayorinde S. Hassan, Kathleen Moyer, B. Ramu Ramachandran, and Collin D. Wick. Comparison of Storage Mechanisms in RuO_2, SnO_2, and SnS_2 for Lithium-Ion Battery Anode Materials. *The Journal of Physical Chemistry C*, 120(4):2036–2046, 2016. doi: 10.1021/acs.jpcc.5b09078. URL `https://doi.org/10.1021/acs.jpcc.5b09078`.

[13] Zhi Xiang Huang, Ye Wang, Bo Liu, Dezhi Kong, Jun Zhang, Tupei Chen, and Hui Ying Yang. Unlocking the potential of SnS_2: Transition metal catalyzed utilization of reversible conversion and alloying reactions. *Scientific Reports*, 7(1):41015, Jan 2017. ISSN 2045-2322. doi: 10.1038/srep41015. URL `https://doi.org/10.1038/srep41015`.

[14] Javed Rehman, Xiaofeng Fan, and W.T. Zheng. Computational insight of monolayer SnS_2 as anode material for potassium ion batteries. *Applied Surface Science*, 496:143625, 2019. ISSN 0169-4332. doi: https://doi.org/10.1016/j.apsusc.2019.143625. URL `https://www.sciencedirect.com/science/article/pii/S0169433219324225`.

[15] K Anlin Lazar, V J Cicily Rigi, D Divya, and K J Saji. Effect of annealing on structural and optical properties of SnS_2 thin films grown by thermal evaporation and post sulphur annealing technique. *IOP Conference Series: Materials Science and Engineering*, 1166(1):012004, jul 2021. doi: 10.1088/1757-899X/1166/1/012004. URL `https://dx.doi.org/10.1088/1757-899X/1166/1/012004`.

[16] Xiaodong Xu, Wen Liu, Youngsik Kim, and Jaephil Cho. Nanostructured transition metal sulfides for lithium ion batteries: Progress and challenges. *Nano Today*, 9(5):604–630, 2014. ISSN 1748-0132. doi: https://doi.org/10.1016/j.nantod.2014.09.005. URL `https://www.sciencedirect.com/science/article/pii/S1748013214001303`.

[17] Muhammad-Sadeeq Balogun, Weitao Qiu, Junhua Jian, Yongchao Huang, Yang Luo, Hao Yang, Chaolun Liang, Xihong Lu, and Yexiang Tong. Vanadium nitride nanowire supported sns2 nanosheets with high reversible capacity as anode material for lithium ion batteries. *ACS Applied Materials & Interfaces*, 7(41):23205–23215, 2015. doi: 10.1021/acsami.5b07044. URL `https://doi.org/10.1021/acsami.5b07044`. PMID: 26439604.

[18] Junjun Zhang, Dongwei Cao, Yang Wu, Xialan Cheng, Wenpei Kang, and Jun Xu. Phase transformation and sulfur vacancy modulation of 2D layered tin sulfide nanoplates as highly durable anodes for pseudocapacitive lithium storage. *Chemical Engineering Journal*, 392:123722, 2020. ISSN 1385-8947. doi: https://doi.org/10.1016/j.cej.2019.123722. URL `https://www.sciencedirect.com/science/article/pii/S1385894719331377`.

[19] Duck Hyun Youn, Shannon K. Stauffer, Penghao Xiao, Hunmin Park, Yejin Nam, Andrei Dolocan, Graeme Henkelman, Adam Heller, and C. Buddie Mullins. Simple Synthesis of Nanocrystalline Tin Sulfide/N-Doped Reduced Graphene Oxide Composites as Lithium Ion Battery Anodes. *ACS Nano*, 10(12):10778–10788, 2016. doi: 10.1021/acsnano.6b04214. URL `https://doi.org/10.1021/acsnano.6b04214`. PMID: 28024327.

[20] Congxin Xia, Yuting Peng, Heng Zhang, Tianxing Wang, Shuyi Wei, and Yu Jia. The characteristics of n- and p-type dopants in SnS_2 monolayer nanosheets. *Phys. Chem. Chem. Phys.*, 16:19674–19680, 2014. doi: 10.1039/C4CP02214A. URL `http://dx.doi.org/10.1039/C4CP02214A`.

[21] D. I. Bletskan and V. V. Frolova. Influence of intrinsic point defects and substitutional impurities (Cl, I→S) on the electronic structure of $2H\text{-}SnS_2$. *Semiconductor Physics, Quantum Electronics and Optoelectronics*, 2018.

[22] Zhixiao Liu, Huiqiu Deng, and Partha P. Mukherjee. Evaluating Pristine and Modified SnS_2 as a Lithium-Ion Battery Anode: A First-Principles Study. *ACS Applied Materials & Interfaces*, 7(7): 4000–4009, 2015. doi: 10.1021/am5068707. URL `https://doi.org/10.1021/am5068707`. PMID: 25629298.

[23] Yaming Liu, Bo Hu, Dechuan Kong, Jianye Wang, Yongfeng Li, Jianxiu Su, and Congxin Xia. Effect of S-vacancy on the oxidation state of Ce in monolayer SnS_2. *International Journal of Modern Physics B*, 33(26):1950308, 2019. doi: 10.1142/S0217979219503089.

[24] Bo Li, Tao Xing, Mianzeng Zhong, Le Huang, Na Lei, Jun Zhang, Jingbo Li, and Zhongming Wei. A two-dimensional Fe-doped SnS_2 magnetic semiconductor. *Nature Communications*, 8(1):1958, Dec 2017. ISSN 2041-1723. doi: 10.1038/s41467-017-02077-z. URL `https://doi.org/10.1038/s41467-017-02077-z`.

[25] Qing Zhan, Xiaoguang Luo, Hao Zhang, Zhenxiao Zhang, Dongdong Liu, and Yingchun Cheng. Carrier and magnetism engineering for monolayer SnS_2 by high throughput first-principles calculations. *Chinese Physics B*, 30(11):117105, dec 2021. doi: 10.1088/1674-1056/ac2805. URL `https://dx.doi.org/10.1088/1674-1056/ac2805`.

[26] Hamid Ullah, Mohammad Noor-A-Alam, and Young-Han Shin. Vacancy- and doping-dependent electronic and magnetic properties of monolayer SnS_2. *Journal of the American Ceramic Society*, 103(1): 391–402, 2020. doi: https://doi.org/10.1111/jace.16739. URL `https://ceramics.onlinelibrary.wiley.com/doi/abs/10.1111/jace.16739`.

[27] Kun Chang, Zhen Wang, Guochuang Huang, He Li, Weixiang Chen, and Jim Yang Lee. Few-layer SnS_2/graphene hybrid with exceptional electrochemical performance as lithium-ion battery anode. *Journal of Power Sources*, 201:259–266, 2012. ISSN 0378-7753. doi: https://doi.org/10.1016/j.jpowsour.2011.10.132. URL `https://www.sciencedirect.com/science/article/pii/S0378775311021872`.

[28] Marappan Sathish, Satoshi Mitani, Takaaki Tomai, and Itaru Honma. Ultrathin SnS_2 Nanoparticles on Graphene Nanosheets: Synthesis, Characterization, and Li-Ion Storage Applications. *The Journal of Physical Chemistry C*, 116(23):12475–12481, 2012. doi: 10.1021/jp303121n. URL `https://doi.org/10.1021/jp303121n`.

[29] Jianping Li, Ping Wu, Feijian Lou, Peng Zhang, Yawen Tang, Yiming Zhou, and Tianhong Lu. Mesoporous carbon anchored with SnS_2 nanosheets as an advanced anode for lithium-ion batteries. *Electrochimica Acta*, 111:862–868, 2013. ISSN 0013-4686. doi: https://doi.org/10.1016/j.electacta.2013.08.104. URL `https://www.sciencedirect.com/science/article/pii/S0013468613016344`.

[30] Baihua Qu, Chuze Ma, Ge Ji, Chaohe Xu, Jing Xu, Ying Shirley Meng, Taihong Wang, and Jim Yang Lee. Layered SnS_2-Reduced Graphene Oxide Composite – A High-Capacity, High-Rate, and Long-Cycle Life Sodium-Ion Battery Anode Material. *Advanced Materials*, 26(23):3854–3859, 2014. doi: https://doi.org/10.1002/adma.201306314. URL `https://onlinelibrary.wiley.com/doi/abs/10.1002/adma.201306314`.

[31] Tommy Lorenz, Jan-Ole Joswig, and Gotthard Seifert. Combined $SnS@SnS_2$ double layers: charge transfer and electronic structure. *Semiconductor Science and Technology*, 29(6):064006, May 2014. doi: 10.1088/0268-1242/29/6/064006. URL `https://dx.doi.org/10.1088/0268-1242/29/6/064006`.

[32] Yandong Zhang, Peiyi Zhu, Liliang Huang, Jian Xie, Shichao Zhang, Gaoshao Cao, and Xinbing Zhao. Few-Layered SnS_2 on Few-Layered Reduced Graphene Oxide as Na-Ion Battery Anode with Ultralong Cycle Life and Superior Rate Capability. *Advanced Functional Materials*, 25(3):481–489, 2015. doi: https://doi.org/10.1002/adfm.201402833. URL `https://onlinelibrary.wiley.com/doi/abs/10.1002/adfm.201402833`.

[33] Dongsheng Guan, Jianyang Li, Xianfeng Gao, and Chris Yuan. Carbon Nanotube-Assisted Growth of Single-/Multi-Layer SnS_2 and SnO_2 Nanoflakes for High-Performance Lithium Storage. *RSC Adv.*, 5, 06 2015. doi: 10.1039/C5RA09613H.

[34] Jiande Liu, Yingfan Chang, Kai Sun, Pengqian Guo, Dianliang Cao, Yaodong Ma, Dequan Liu, Qiming Liu, Yujun Fu, Jie Liu, and Deyan He. Sheet-Like Stacking SnS_2/rGO Heterostructures as Ultrastable Anodes for Lithium-Ion Batteries. *ACS Applied Materials & Interfaces*, 14(9):11739–11749, 2022. doi: 10.1021/acsami.1c18268. URL `https://doi.org/10.1021/acsami.1c18268`. PMID: 35200005.

[35] Rumeng Zhao, Tianxing Wang, Mingyu Zhao, Congxin Xia, Xu Zhao, Yipeng An, and Xianqi Dai. A theoretical simulation of small-molecules sensing on an S-vacancy SnS_2 monolayer. *Phys. Chem. Chem. Phys.*, 19:10470–10480, 2017. doi: 10.1039/C7CP00336F. URL `http://dx.doi.org/10.1039/C7CP00336F`.

[36] Jianbiao Wang, Jiajia Huang, Shuping Huang, Hiroo Notohara, Koki Urita, Isamu Moriguchi, and Mingdeng Wei. Rational Design of Hierarchical SnS_2 Microspheres with S Vacancy for Enhanced Sodium Storage Performance. *ACS Sustainable Chemistry & Engineering*, 8(25):9519–9525, 2020. doi: 10.1021/acssuschemeng.0c02535. URL `https://doi.org/10.1021/acssuschemeng.0c02535`.

[37] Yu Huang, Shengqi Ding, Sunjie Xu, Zi-Feng Ma, and Xianxia Yuan. Binder-free SnS_2 sheet array with high sulfur vacancy concentration for enhanced lithium storage performance. *Electrochimica Acta*, 409:139979, 2022. ISSN 0013-4686. doi: https://doi.org/10.1016/j.electacta.2022.139979. URL `https://www.sciencedirect.com/science/article/pii/S0013468622001517`.

Chapter 3

Density Functional Theory

This chapter explains the Density Functional Theory (DFT) from its foundations as a solution to the study of the electronic structure of real material systems. The material is expressed as a many-body problem, which DFT attempts to solve. The various approaches to previously solve the many-body system are introduced first, building the basis of the first-principles DFT method. After introducing the many-body problem for solids, approximations are applied; that being the Born-Oppenheimer and Hartree-Fock approximations. This is followed by a review of the initial details of DFT, the HK theorems and KS equations. DFT methods are applied using XC functionals, for which various flavours of functionals are introduced; the standard local density approximation (LDA) and generalized gradient approximation (GGA), as well as hybrid functionals. The Hellman-Feynman theorem is briefly discussed, before moving on to the calculations used for practical application of DFT, such as Bloch's theorem, the plane wave basis set, the Brillouin zone, and pseudopotentials.

3.1   The many-body problem for solids

When considering a solid material, it is known to consist of a dense number of electrons and nuclei. These quantum scale interactions govern the properties of our material, and can be described using the many-body Schrödinger equation:

$$\hat{H}\Psi = E\Psi, \tag{3.1}$$

which consists of the wavefunction Ψ, the total energy eigenvalue E, and the Hamiltonian operator $\hat{H}$ of the system. $\hat{H}$ can be expanded upon when considering electrons and nuclei and introduces the following equation:

$$\hat{H} = -\sum_i \frac{\hbar^2}{2m_e}\boldsymbol{\nabla}_i^2 - \sum_I \frac{\hbar^2}{2M_I}\boldsymbol{\nabla}_I^2 - \frac{1}{4\pi\epsilon_0}\sum_{i,I}\frac{Z_I e^2}{|\mathbf{r}_i - \mathbf{R}_I|}$$
$$+ \frac{1}{2}\frac{1}{4\pi\epsilon_0}\sum_{i\neq j}\frac{e^2}{|\mathbf{r}_i - \mathbf{r}_j|} + \frac{1}{2}\frac{1}{4\pi\epsilon_0}\sum_{I\neq J}\frac{Z_I Z_J e^2}{|\mathbf{R}_I - \mathbf{R}_J|}, \tag{3.2}$$

where $\hbar$, m_e, ϵ_0 are the reduced Planck's constant, electron mass, and vacuum permittivity, respectively. Additionally, M_I is the nucleus mass, Z_I is the atomic number of the nucleus. $\mathbf{r}_i$ and $\mathbf{R}_I$ represent three

dimensional position vectors for the ith electron and I^{th} nucleus, respectively. The five terms of of our Hamiltonian represent the various interactions between electrons and nuclei, and $\hat{H}$ can summarily be denoted by:

$$\hat{H} = \hat{T}_e + \hat{T}_I + \hat{V}_{eI} + \hat{V}_{ee} + \hat{V}_{II}. \tag{3.3}$$

$\hat{T}_e$ and $\hat{T}_I$ are the kinetic energy operators for the electrons and nuclei (or ions) respectively. $\hat{V}_{eI}$, $\hat{V}_{ee}$ and $\hat{V}_{II}$ represent the operators for electron-nucleus, electron-electron and nucleus-nucleus Coulomb interactions. The notation is further simplified through the use of atomic units by having $\hbar = e = m_e = 4\pi\epsilon_0 = 1$.

Our wavefunction Ψ displays a dependency on the degrees of freedom of the ions and electrons, $\Psi(\mathbf{r}_i, \mathbf{R}_I)$, such that eq. 3.1 can be rewritten as:

$$\left(\hat{T}_e + \hat{T}_I + \hat{V}_{eI} + \hat{V}_{ee} + \hat{V}_{II} \right) \Psi(\mathbf{r}_i, \mathbf{R}_I) = E\Psi(\mathbf{r}_i, \mathbf{R}_I). \tag{3.4}$$

Obtaining properties for a system requires solving the Schrödinger equation, which, if attempted starting at eq. 3.4, proves troublesome without some form of approximation, such as the Born-Oppenheimer approximation discussed in the following section.

3.1.1 Born-Oppenheimer approximation

For a material consisting of a system of N nuclei, the number of interacting particles will be $N + \sum_{I=1}^{N} Z_I$. In attempt to reduce this the complexity of these interactions, the following assumption is made; electron and nucleus motion can be decoupled, or, relative to the motion of electrons in our many-body problem, the positions of our nuclei are fixed. The justification for this relies primarily on the mass difference between nuclei and electrons, since for even the lightest element H, the mass ratio is ~ 1800 in favor of the nucleus.

This allows for the replacement of operator $\hat{T}_I$ with classical kinetic energy T_I in eq. 3.4, which can be neglected thanks to the Hamiltonian. Positions $\mathbf{R}_I$ have become fixed, thus there are the nucleus-nucleus Coulomb interactions being expressed classically; $\hat{V}_{II}$ becoming V_I. Our initial wavefunction Ψ can now be separated into an electronic wavefunction ψ and nuclear wavefunction χ,

$$\Psi(\mathbf{r}_i, \mathbf{R}_I) = \psi(\mathbf{r}_i) \cdot \chi(\mathbf{R}_I). \tag{3.5}$$

The wavefunction ψ has no explicit $\mathbf{R}_I$ dependency, since the nucleus positions $\mathbf{R}_I$ are no longer variables but parameters, as changes to nuclei positions show immediate effect in the rearrangement of electrons. Following the substitution of wavefunction 3.5 into the the Schrödinger equation (3.2), the result is:

$$\left(-\sum_i \frac{1}{2} \boldsymbol{\nabla}_i^2 - \sum_{i,I} \frac{Z_I}{|\mathbf{r}_i - \mathbf{R}_I|} + \frac{1}{2} \sum_{i \neq j} \frac{1}{|\mathbf{r}_i - \mathbf{r}_j|} \right) \psi(\mathbf{r}_i) = E_e(\mathbf{R}_I)\psi(\mathbf{r}_i)$$

$$\left(\hat{T}_e + \hat{V}_{ext} + \hat{V}_{ee} \right) \psi(\mathbf{r}_i) = E_e(\mathbf{R}_I)\psi(\mathbf{r}_i), \tag{3.6}$$

where the energy eigenvalue $E_e(\mathbf{R}_I)$ is the total energy with all nuclear energies subtracted:

$$E_e(\mathbf{R}_I) = E - T_I - V_I. \tag{3.7}$$

Following the Born-Oppenheimer approximation, eq. 3.6 still proves troublesome to solve. The electrons remain large in number, interacting with each other and with nuclei (the $\hat{V}_{ee}$ and $\hat{V}_{ext}$ terms). An additional issue that has yet to be addressed is the fermion nature of electrons, which complicate calculations through the addition of the wavefunction ψ being anti-symmetric. The next section introduces an additional approximation, further simplifying the solution to the Schrödinger equation.

3.1.2 Hartree-Fock approximation

The initially proposed Hartree approximation assumes that the interactions between electrons can be replaced with a mean-field describing the potential effecting each electron individually. The many-body wavefunction $\psi(\mathbf{r}_i)$ can then be considered as a product of N single electron independent wavefunctions ϕ expressed as follows:

$$\psi(\mathbf{r}_1, \mathbf{r}_2, \ldots, \mathbf{r}_N) = \phi_1(\mathbf{r}_1)\phi_2(\mathbf{r}_2) \ldots \phi_N(\mathbf{r}_N). \tag{3.8}$$

Applying this approximation to eq. 3.6 will obtain an independent particle Schrödinger equation, the Hartree equation, which looks as follows:

$$\left(\hat{T}_e + \hat{V}_{eff}\right)\phi_i(\mathbf{r}) = \varepsilon_i(\mathbf{r})\phi_i(\mathbf{r}). \tag{3.9}$$

The energy eigenvalue $\varepsilon_i(\mathbf{r})$ for the ith electron is obtained. $\hat{V}_{eff}$ represents the effective potential. This is the mean-field potential experienced by each electron, which is the sum of the external potential $\hat{V}_{ext}$ and the potential due to all other electrons V_H, called the Hartree potential:

$$\begin{aligned}\hat{V}_{eff} &= \hat{V}_{ext} + V_H(\mathbf{r}) \\ &= \hat{V}_{ext} + \int \frac{\rho(\mathbf{r}')}{|\mathbf{r} - \mathbf{r}'|}d\mathbf{r}'. \end{aligned} \tag{3.10}$$

$\rho(\mathbf{r})$ is our electron density. The total electron density of the system can be determined as:

$$\rho(\mathbf{r}) = \sum_i^N |\phi_i(\mathbf{r})|^2. \tag{3.11}$$

The single-particle Hartree equation 3.9 is solvable through iterative self-consistent field methods. Starting from the initial wavefunction ϕ_i and a constructed total electron density $\rho(\mathbf{r})$, the effective potential $\hat{V}_{eff}$ would be obtained; this result is then used to obtain a new set of wavefunctions ψ_i. However, after the Hartree approximation underwent experimental testing, results were inconsistent with real systems of the many-body wavefunction. This is due to the approximation was made in ignorance of the Pauli exclusion principle; the electron wavefunction must be anti-symmetric.

To correct for this inconsistency, Fock improved upon the Hartree approximation through the inclusion of anti-symmetry to satisfy Pauli exclusion. The notion of a Slater determinant is used to obtain the

following revision of eq. 3.8:

$$\psi(\mathbf{r}_1,\sigma_1,\mathbf{r}_2,\sigma_2,\ldots) = \frac{1}{\sqrt{N!}} \begin{vmatrix} \phi_1(\mathbf{r}_1,\sigma_1) & \phi_2(\mathbf{r}_1,\sigma_1) & \cdots & \phi_N(\mathbf{r}_1,\sigma_1) \\ \phi_1(\mathbf{r}_2,\sigma_2) & \phi_2(\mathbf{r}_2,\sigma_2) & \cdots & \phi_N(\mathbf{r}_2,\sigma_2) \\ \vdots & \vdots & \ddots & \vdots \\ \phi_1(\mathbf{r}_N,\sigma_N) & \phi_2(\mathbf{r}_N,\sigma_N) & \cdots & \phi_N(\mathbf{r}_N,\sigma_N) \end{vmatrix} \tag{3.12}$$

The $(N!)^{-1/2}$ factor is in place to normalize the Slater determinant, and σ_i represents the spin component of each electron orbital, which can have one of two spin functions. The electron labels increasing along columns while the orbital labels increases along rows, conserves the anti-symmetric properties of Pauli exclusion. The Slater determinant can be written in a simplified form as follows:

$$\psi(\mathbf{r}_1,\sigma_1,\mathbf{r}_2,\sigma_2,\ldots) = \frac{1}{\sqrt{N!}} \sum_p^{N!} (-1)^p \hat{P} \left[\phi_1, \phi_2, \ldots, \phi_N \right], \tag{3.13}$$

where $\hat{P}$ is the permutation operator. The variational principle can now be used along with the expectation value of the Hamiltonian with the Hartree-Fock (HF) approximation. Calculating the expectation value for total energy E_{HF}, will result in obtaining the HF equations.

$$\begin{aligned} E_{HF} =& \langle \psi | \hat{H} | \psi \rangle = \int \psi^*(\mathbf{r}_1,\ldots,\mathbf{r}_N) \hat{H} \psi(\mathbf{r}_1,\ldots,\mathbf{r}_N) d\mathbf{r}_1 \ldots d\mathbf{r}_N \\ =& \int \phi^*(\mathbf{r}) \left(-\frac{1}{2} \sum_i^N \boldsymbol{\nabla}^2 + \hat{V}_{ext} \right) \phi_i(\mathbf{r}) d\mathbf{r} \\ &+ \frac{1}{2} \sum_{i,j(i\neq j)}^N \int \frac{\phi_i^*(\mathbf{r}_1)\phi_i(\mathbf{r}_1)\phi_j^*(\mathbf{r}_2)\phi_j(\mathbf{r}_2)}{|\mathbf{r}_i - \mathbf{r}_j|} d\mathbf{r}_1 d\mathbf{r}_2 \\ &- \sum_{i,j(i\neq j)}^N \int \frac{\phi_i^*(\mathbf{r}_1)\phi_j(\mathbf{r}_1)\phi_i(\mathbf{r}_2)\phi_j^*(\mathbf{r}_2)}{|\mathbf{r}_i - \mathbf{r}_j|} d\mathbf{r}_1 d\mathbf{r}_2 \end{aligned} \tag{3.14}$$

Through additional algebra, the HF equation for a single electron i can be obtained:

$$\left(\hat{T}_e + \hat{V}_{ext} + V_H \right) \phi_i(\mathbf{r}) + \int V_X(\mathbf{r},\mathbf{r}') \phi_i(\mathbf{r}') d\mathbf{r}' = \varepsilon_i \phi_i(\mathbf{r}), \tag{3.15}$$

in which the function V_X, is the non-local exchange potential. This potential is derived as consequence of Pauli exclusion preventing electrons from occupying the same state, and is defined in eq. 3.16. The non-locality of this potential is indicated by the additional positional vector $\mathbf{r}'$.

$$V_X(\mathbf{r},\mathbf{r}') = -\sum_j^N \frac{\phi_j^*(\mathbf{r}')\phi_j(\mathbf{r})}{|\mathbf{r} - \mathbf{r}'|}. \tag{3.16}$$

Overall, several conclusions can be drawn from eq. 3.14. As discussed, the non-interacting electrons are described as being under the influence of a mean-field consisting of the sum of the Hartree potential and the non-local exchange potential. An issue appears as consequence of neglecting electron correlation, which can be considered as the difference between the exact value and the HF energy. This difference is caused by the HF equation being derived using the variational principle, leading to it being an upper

bound of the true ground state energy E_0. The difference causes errors in predicting the density of states of the homogeneous electron gas for more extreme conditions, such as an erroneous prediction of the gas vanishing at the Fermi level. To improve upon the HF approximation, correlation effects must be taken into account, as is done with the DFT method, although improvements can also be done after application of HF to improve its accuracy.

3.2   Introduction to Density Functional Theory

Understanding the methodology of DFT can be done through contrasting it with the previously discussed HF method. Whereas the previous method had a process of $V_{ext}(\mathbf{r}) \Rightarrow \psi(\mathbf{r}, \mathbf{R})$ and $E(\mathbf{R}) \Rightarrow$ Properties, that is to say, starting from the mean electric field to obtain the wavefunction and then the properties of a material, now the mean field V_{ext} is substituted with a more easily obtainable value; the charge density. Given the charge distribution or density of a material, an approximate wavefunction can be obtained, and from the wavefunction the total energy is obtained which is used to determine electronic properties: $\rho(\mathbf{r}) \Rightarrow \psi(\mathbf{r}, \mathbf{R})$ and $E(\mathbf{R}) \Rightarrow$ Properties.

Charge density $\rho(\mathbf{r})$ is calculated from the electronic wavefunction:

$$\rho(\mathbf{r}) = \sum_{i=1} N \int \ldots \int \psi^*(\mathbf{r}_1, \ldots, \mathbf{r}_N)\delta(\mathbf{r} - \mathbf{r}_i)\psi(\mathbf{r}_1, \ldots, \mathbf{r}_N)d\mathbf{r}_1 \ldots d\mathbf{r}_N, \tag{3.17}$$

with N being the number of electrons. Additionally, frequently a functional (i.e. a function for which another function is its variable) is made use of , such as the energy functional $E(n)$. As required, the functional derivative is defined as:

$$\frac{\delta}{\delta f(x)}F[f] = \lim_{\epsilon \to 0} \frac{F[f(x) + \epsilon\delta(x - x')] - F[f(x)]}{\epsilon}. \tag{3.18}$$

In addition to the derivative, there are the following derived properties of functional derivation:

$$\frac{\delta}{\delta f(x)}\left(\int F[f]dx\right) = \frac{\delta F[f]}{\delta f(x)},$$
$$\frac{\delta}{\delta f(x)}\left(\int F[f]f(x)dx\right) = \frac{\delta F[f]}{\delta f(x)}f(x) + F[f(x)], \tag{3.19}$$
$$\frac{\delta}{\delta f(x)}\left(\frac{1}{2}\iint g(x, x')f(x)f(x')dxdx'\right) = \int g(x, x')f(x')dx'.$$

3.2.1   Hohenberg-Kohn theorems

The Hohenberg-Kohn (HK) theorems form the basis of DFT, and were first formulated by P. Hohenberg and W. Kohn in 1964. The first of the two theorems states as follows[1]:

> For any system of interacting particles, the external potential $V_{ext}(\mathbf{r})$ is a uniquely determined–except for a constant–functional of density $\rho(\mathbf{r})$. This in turn fixes $\hat{H}$ such that the many-particle ground state energy is a unique functional of ground state density $\rho_0(\mathbf{r})$.

The proof of this theorem is based on reductio ad absurdum, or proven by contradiction. The proof starts with assuming that there exist two Hamiltonians with external potentials V_{ext}^1 and V_{ext}^2. It can be

assumed that the Hamiltonians gives two different wavefunctions $\psi_1 \neq \psi_2$, from the same ground state electron density $\rho_0(\mathbf{r})$.

$$
\begin{cases}
\hat{H}_1\psi_1 = E_1\psi_1 \\
\hat{H}_1\psi_2 = E_2\psi_2
\end{cases}
\tag{3.20}
$$

An additional requirement becomes apparent when subtracting these Hamiltonians from each other, producing the following equation:

$$
\left(\hat{V}_{ext}^1 - \hat{V}_{ext}^2\right)\psi = (E_1 - E_2)\psi,
\tag{3.21}
$$

Which would suggest that if the difference $\hat{V}_{ext}^1 - \hat{V}_{ext}^2$ is a constant, two different wavefunctions $\psi_1 \neq \psi_2$ are not obtained. Thus, the difference must be greater than a constant.

Returning to the proof, the variational principle is used to show that the same electron density is obtained from both wavefunctions. Firstly:

$$
\begin{aligned}
E_1 < \langle \psi_2 | \hat{H}_1 | \psi_2 \rangle &= \langle \psi_2 | \hat{H}_1 - \hat{H}_2 + \hat{H}_2 | \psi_2 \rangle \\
&= \langle \psi_2 | \hat{V}_{ext}^1 - \hat{V}_{ext}^2 | \psi_2 \rangle + E_2 \\
&= \int \rho_0(\mathbf{r}) \left(\hat{V}_{ext}^1 - \hat{V}_{ext}^2\right) d\mathbf{r} + E_2.
\end{aligned}
\tag{3.22}
$$

Consequently:

$$
E_1 - E_2 < \int \rho_0(\mathbf{r}) \left(\hat{V}_{ext}^1 - \hat{V}_{ext}^2\right) d\mathbf{r}.
\tag{3.23}
$$

The same procedure is repeated while swapping out the Hamiltonian and wavefunction:

$$
E_2 < \langle \psi_1 | \hat{H}_2 | \psi_1 \rangle,
\tag{3.24}
$$

which will lead to the result:

$$
E_1 - E_2 > \int \rho_0(\mathbf{r}) \left(\hat{V}_{ext}^1 - \hat{V}_{ext}^2\right) d\mathbf{r}.
\tag{3.25}
$$

Comparing the results of equations 3.23 and 3.25 shows that the contradiction $E_1 + E_2 < E_1 + E_2$ has been produced, which is cannot be true due to the strict inequalities. The assumptions made for external potentials differing by more than a constant does not hold, and for any particular Hamiltonian and ground state density, the result is a uniquely determined external potential.

Moving on to the second HK theorem, which states [1]:

> *There exists an energy functional $E[\rho]$, for which the ground state energy is given by the global minimum of the energy functional $E[\rho]$. The ground state density $\rho_0(\mathbf{r})$ is the density that minimizes this functional to the exact ground state energy.*

The second HK theorem builds on the first HK theorem, which allows the energy to be a functional of density, thus all components are also functionals of density.

$$E[\rho] = \langle\psi|\hat{H}|\psi\rangle = T[\rho] + V_{ee}[\rho] + V_{ext}[\rho] \tag{3.26}$$

Define an HK functional to keep the remainder beyond external energy, thus $F_{HK}[\rho] = T[\rho] + V_{ee}[\rho]$, valid for any number of electrons and external potential. Thus the following rewrite is allowed:

$$E[\rho] = \langle\psi|\hat{H}|\psi\rangle = F_{HK}[\rho] + \int \rho(\mathbf{r})V_{ext}(\mathbf{r})d\mathbf{r} \tag{3.27}$$

Next, define an energy with the ground state electron density wavefunction as follows:

$$E_0 = E[\rho_0] = \langle\psi_0|\hat{H}_0|\psi_0\rangle \tag{3.28}$$

As consequence of this definition, any variation in electron wavefunction, i.e. using the variation principle, must give a total energy greater than the ground state energy:

$$E_0 = E[\rho_0] = \langle\psi_0|\hat{H}_0|\psi_0\rangle < \langle\tilde{\psi}|\hat{H}_0|\tilde{\psi}\rangle = \tilde{E}[\tilde{n}] \tag{3.29}$$

This is always true, and it can be concluded that the ground state density $\rho_0(\mathbf{r})$ minimizes the energy functional $E[\rho]$, proving the second HK thoerem.

3.2.2 Kohn-Sham equations

The many-body problem within DFT has yet to be simplified to the point of practical application, with the HK theorems providing only a basis for finding the ground state energy and density. The most popular method of simplifying many-body problems is the method introduced by W. Kohn and L. J. Sham[2], which builds on the HK theorems. The Kohn-Sham (KS) approach replaces the fully interacting many-body system with an auxiliary system that is more easily solved. Our initial assumption is that ground state density of the difficult interacting system is the same as a system of non-interacting electrons moving in a mean field format. First, look at the total energy functional, building on eq. 3.26:

$$E[\rho(\mathbf{r})] = T_{KS}[\rho(\mathbf{r})] + (E_H[\rho(\mathbf{r})] + E_{XC}[\rho(\mathbf{r})]) + V_{ext}[\rho(\mathbf{r})]. \tag{3.30}$$

The four terms of the total energy functional are, in order, the KS kinetic energy, in brackets (which represents electron-electron interactions) the Hartree energy and exchange-correlation term, and lastly the external potential. The latter needs no further approximation and is used as it exists in eq. 3.27. Now new equations for each term needs to be introduced, with these equations being applied to the more solvable auxiliary system, starting with the KS kinetic energy:

$$T_{KS}[\rho(\mathbf{r})] = -\frac{1}{2}\sum_{i}^{N} \langle\phi_i|\boldsymbol{\nabla}^2|\phi_i\rangle. \tag{3.31}$$

Here, the single-electron wavefunction is preferred for the sake of simplicity. The KS kinetic energy, as with all KS energies, is not the same as the kinetic energy of the many-body problem, but there is still the same ground state density derived from the electron wavefunction:

$$n_{KS}(\mathbf{r}) = \sum_{i}^{N} |\phi_i(\mathbf{r})|^2 = \rho_0(\mathbf{r}). \tag{3.32}$$

The last term to look at, the external potential, is as mentioned similar to the expression in eq. 3.27:

$$V_{ext}[\rho] = \int \rho(\mathbf{r})V_{ext}(\mathbf{r})d\mathbf{r}, \tag{3.33}$$

and moving on to the first term in brackets, the Hartree energy, which will bear similarity to the Hartree potential of eq. 3.10:

$$E_H[\rho] = \frac{1}{2} \iint \frac{\rho(\mathbf{r})\rho(\mathbf{r}')}{|\mathbf{r} - \mathbf{r}'|} d\mathbf{r}d\mathbf{r}'. \tag{3.34}$$

Next, the exchange-correlation energy functional $E_{XC}[\rho]$ remains undefined, and requires some experimentation regarding possible solutions. Before discussing them, consider the differentiation of our energy functionals w.r.t. $\rho(\mathbf{r})$. The obtained definitions for the external, Hartree, and exchange-correlation potentials will sum to result in the KS effective potential:

$$
\begin{aligned}
V_{ext}(\mathbf{r}) &= \frac{\delta V_{ext}[\rho(\mathbf{r})]}{\delta\rho(\mathbf{r})} = \frac{\delta \int V_{ext}(\mathbf{r})\rho(\mathbf{r})d\mathbf{r}}{\delta\rho(\mathbf{r})} \\
V_H(\mathbf{r}) &= \frac{\delta E_H[\rho(\mathbf{r})]}{\delta\rho(\mathbf{r})} = \int \frac{\rho(\mathbf{r}')}{|\mathbf{r} - \mathbf{r}'|}d\mathbf{r}' \\
V_{XC}(\mathbf{r}) &= \frac{\delta E_{XC}[\rho(\mathbf{r})]}{\delta\rho(\mathbf{r})}
\end{aligned}
\tag{3.35}
$$

$$V_{eff}(\mathbf{r}) = V_{ext}(\mathbf{r}) + V_H(\mathbf{r}) + V_{XC}(\mathbf{r}) \tag{3.36}$$

The exchange-correlation energy is expanded upon in the next section. A variety of methods exist to solve for this functional, with varying degrees of accuracy.

3.3 Exchange-correlation functionals

The exchange-correlation functional, which remains undefined following the KS equations, can have a solution constructed to allow for the correct ground state energy and density. Several approximations exist for $E_{XC}[\rho(\mathbf{r})]$, with a choice of two general types that can also be applied simultaneously. These approximation types are the local density approximation (LDA) and generalized gradient approximation (GGA).

Before approaching these approximations, the functional should be considered with respect to how the real interacting system and the auxiliary non-interacting system can be connected.

$$H_\lambda = T + \lambda V_{ee} + \lambda V_{ext}^\lambda \tag{3.37}$$

To connect the systems eq. 3.37 is introduced. The equation makes use of the parameter λ to differentiate being the non-interacting $(\lambda = 0)$ and interacting $(\lambda = 1)$ systems. The difference between the systems should represent $E_{XC}[\rho(\mathbf{r})]$:

$$E_{XC}[\rho] = \langle\psi^\lambda[\rho]|T + \lambda V_{ee}|\psi^\lambda[\rho]\rangle\Big|_{\lambda=1}$$
$$- \langle\psi^\lambda[\rho]|T + \lambda V_{ee}|\psi^\lambda[\rho]\rangle\Big|_{\lambda=0} - E_H, \tag{3.38}$$

which can be solved as follows:

$$E_{XC}[\rho] = \int_0^1 d\lambda \frac{d}{d\lambda} \langle\psi^\lambda[\rho]|T + \lambda V_{ee}|\psi^\lambda[\rho]\rangle - E_H$$
$$= \int_0^1 d\lambda \langle\psi^\lambda[\rho]|\frac{dV_{ee}}{d\lambda}|\psi^\lambda[\rho]\rangle - E_H. \tag{3.39}$$

We end up with the following Coulomb integral as result:

$$E_{XC}[\rho] = \frac{1}{2} \iint \frac{\rho(\mathbf{r})n_{xc}(\mathbf{r},\mathbf{r}')}{|\mathbf{r}-\mathbf{r}'|} d\mathbf{r}d\mathbf{r}' \tag{3.40}$$

The introduced density, $n_{xc}(\mathbf{r},\mathbf{r}')$, is known as the exchange-correlation hole. Investigating the nature of this density reveals several properties that act as requirements for any approximation of the $E_{XC}[\rho]$ functional. Among these properties is the decomposition of the functional into a sum of the exchange and correlation parts:

$$E_{XC}[\rho] = E_X[\rho] + E_C[\rho] \tag{3.41}$$

3.3.1 Local density approximation

Looking at LDA, the approximation is applied for system of a homogeneous or uniform electron gas. In particular, the exchange-correlation energy per electron at a point $\mathbf{r}$ in the electron gas is the same as the exchange-correlation energy per electron for the homogeneous electron gas. For sufficiently slowly varying $\rho(\mathbf{r})$ the exchange-correlation energy under LDA is described by:

$$E_{XC}^{LDA}[\rho] = \int \varepsilon_{XC}^{hom}[\rho(\mathbf{r})]\rho(\mathbf{r})d\mathbf{r}, \tag{3.42}$$

and as stated, the exchange-correlation energies have been equated:

$$\varepsilon_{XC}^{hom}[\rho(\mathbf{r})] = \varepsilon_{XC}[\rho(\mathbf{r})]. \tag{3.43}$$

Unfortunately, eq. 3.42 disregards magnetic materials, for which spin must be considered. The addition of spin densities $(n_\uparrow(\mathbf{r}), n_\downarrow(\mathbf{r}))$ is required for a more accurate approximation. This leads to a modification of the exchange-correlation energy to obtain what is known as the local spin density approximation (LSDA):

$$E_{XC}^{LSDA}[\rho] = \int \varepsilon_{XC}^{hom}[n_\uparrow(\mathbf{r}), n_\downarrow(\mathbf{r})]\rho(\mathbf{r})d\mathbf{r}. \tag{3.44}$$

We have an exchange correlation energy per electron ε_{XC}^{hom} present within the integral. Since this depends only on local density at $\mathbf{r}$, applying eq. 3.41 separates the X and C contributions, resulting in:

$$\varepsilon_{XC}[\rho(\mathbf{r})] = \varepsilon_X[\rho(\mathbf{r})] + \varepsilon_C[\rho(\mathbf{r})] \tag{3.45}$$

An exact equation for the X contribution was proposed by Dirac in 1930[3], evaluated exactly as[4]:

$$\varepsilon_X[\rho(\mathbf{r})] = -\frac{3}{4}\left(\frac{3\rho(\mathbf{r})}{\pi}\right)^{\frac{1}{3}} \tag{3.46}$$

Accurate values for the correlation energy ε_C have been acquired using Monte Carlo simulations[5]. Obtaining the result analytically only works for the low and high limits of density.

LSDA by design works perfectly for a uniform system, while also approximating a slowly varying density system with a good degree of accuracy. Issues become apparant for real electronic systems, which have a rapidly varying density, for which LSDA only has a moderate degree of accuracy. The preferred applications of this approximation are for the ground state properties of metals, and at times obtaining KS eigenvalues in photo-emission experimentation. The drawbacks of LSDA can result in an overestimation of $\varepsilon_{XC}[\rho]$, and consequently the total energy[6].

3.3.2 Generalized gradient approximation

In an attempt to prevent the errors of LDA and LSDA, GGA represents a general family of methods, with GGA(PBE) being a popular example. LDA is improved upon by accounting for spatial change in local density, which is done by including (powers of) the gradient in the exchange-correlation functional. In general, the generalized gradient approximation is described by:

$$E_{XC}^{GGA}[n_\uparrow(\mathbf{r}), n_\downarrow(\mathbf{r})] = \int \varepsilon_{XC}[\rho(\mathbf{r})]g[n_\uparrow(\mathbf{r}), n_\downarrow(\mathbf{r}), \boldsymbol{\nabla} n_\uparrow(\mathbf{r}), \boldsymbol{\nabla} n_\downarrow(\mathbf{r})]\rho(\mathbf{r})d\mathbf{r} \tag{3.47}$$

The exchange-correlation energy $\varepsilon_{XC}[\rho(\mathbf{r})]$ makes use of the same homogeneous electron gas density from eq. 3.43. Due to the number of existing GGA variations, focus will be placed on the previously mentioned GGA(PBE) developed by Perdew, Burke and Ernzerhof[7]. Similar to LDA, separate the X and C contributions of $E_{XC}[\rho]$:

$$E_{XC}^{GGA}[\rho] = E_X^{GGA}[\rho] + E_C^{GGA}[\rho]. \tag{3.48}$$

For each contribution, an integral containing the homogeneous energy per electron along with additional terms is constructed. For the exchange functional that results in:

$$E_X^{GGA}[\rho] = \int \varepsilon_X^{hom}[\rho(\mathbf{r})]F_X(s)\rho(\mathbf{r})d\mathbf{r}. \tag{3.49}$$

The additional term $F_X(s)$ is an enhancement factor to improve our exchange energy result. This factor is defined as[8,9]:

$$F_X(s) = 1 + \kappa - \frac{\kappa}{1 + \frac{\mu}{\kappa}s^2}, \tag{3.50}$$

with constants $\kappa = 0.804$ and $\mu = 0.21951$. The variable s is derived from the gradient of density where $s = \frac{|\boldsymbol{\nabla} n|}{2(3\pi^2)^{1/3}n^{4/3}}$.

Moving on to the correlation functional, defined as:

$$E_C^{GGA}[n_\uparrow, n_\downarrow] = \int \left(\varepsilon_C^{hom}(r_s, \zeta) + H(r_s, \zeta, t) \right) \rho(\mathbf{r}) d\mathbf{r}. \tag{3.51}$$

r_s is the local Seitz radius, and $\zeta = \frac{n_\uparrow - n_\downarrow}{n}$ the relative spin polarization. The variable $t = \frac{|\boldsymbol{\nabla} n|}{2\phi k_s n}$ is the dimensionless gradient of density, for which ϕ is defined as $\phi = \frac{1}{2}[(1 + \zeta)^{\frac{2}{3}} + (1 - \zeta)^{\frac{2}{3}}]$. Returning to eq. 3.51, the term $H(r_s, \zeta, t)$ represents the gradient contribution of the homogeneous gas.

GGA(PBE) more accurately predicts the energy and volume of certain atoms and structures, overcoming LDA's major drawbacks. Additionally, better results are obtained for binding and atomization energies, which can be applied to systems of much more quickly varying density (although limits to this improvement exist),

Having discussed both of the general types of exchange-correlation functionals, a drawback of the standard DFT model becomes apparent. The usage of the Hartree energy introduces its self-interaction flaw, while integrating over the electrons interferes with the particle discontinuity that should be present for a system of quantum particles. Hybrid functionals and modifying methods, such as DFT+U, can be applied to counter these flaws.

3.3.3 DFT+U method

A significant issue with the default DFT method, with regards to LDA and GGA results, is an underestimation of band gaps of up to 40% compared to experimental results. More particularly, the this underestimation occurs for materials with any of the following properties; strong correlations forces, the presence of defects, the presence of organic molecules, etc. Various post-DFT methods as well as hybrid functionals exist to correct this and correlated errors, such as the time-dependent DFT (TDDFT) formulation, the GW method, and Diffusion Monte Carlo[10–12]. In this section the DFT Hubbard U method for correction is explained, which is applied as part of the computational method undergone to obtain the results of chapter 4. When compared to the previously mentioned methods, DFT+U provides a similar level of reliability while lowering the computational cost considerably for a post-DFT method.

The method starts by making corrections to the electron structure of the target system using the U parameter, and as a result the accuracy of predictions regarding intermolecular forces and formation energy is improved. Beyond improvements with respect to electronic properties, improvements can also be seen in the results of magnetic and structural properties, electron charge transfer, and chemical reactions.

Where the Hubbard method starts to fail is in the prediction of properties for systems with more widespread density, that is to say the electrons are more delocalized, which includes heavier transition metals. The Hubbard model separates the localized and delocalized electrons, with the former having strong Coulomb repulsion U that need to be taken into account, and the latter can continue to be expressed using the existing DFT functionals. The ease of use of DFT+U is among its best advantages, through which underestimated electron energies are improved by simply adding a chosen parameter $\mathcal{U}$ to obtain the correct band gap result[13]:

$$E_{DFT+\mathcal{U}}[\rho(\mathbf{r}), n] = E_{DFT}[\rho(\mathbf{r})] + E_\mathcal{U}[n_{mm'}^{l\sigma}] - E_{dc}[n^{l\sigma}]. \tag{3.52}$$

In eq. 3.52, n represents the electron energy level, with parameters m and l indicating the electron

state and atomic site to determine the orbital, while σ indicates spin. In effect, the standard LDA or GGA total energy has a Hubbard contribution $E_{\mathcal{U}}$ added to it, while also subtracting E_{dc}, a term for eliminating "double-counting". Variations on the above exist and can be applied depending on the system, as E_{dc} remains undefined.

Returning to the parameter $\mathcal{U}$, with the ease at which it can be selected, DFT+U can easily determine the influence of electron correlation at higher energy levels and how this effects a system's properties. The primary drawbacks of the method are that it is more computationally heavy than DFT alone, though the advantage of obtaining an accurate band gap can outweigh that, depending on the material.

Returning to eq. 3.52, this imprecise equation can be expanded upon with more specific formulations, such as the fully localized limit (FLL) formulation which uses more localized electrons and orbitals. The FLL formulation is preferred for its capability to expand the KS orbitals, to more effectively capture Mott transition and localization in semiconductors. The formulation replaces E_{dc} in eq. 3.53 such that:

$$E_{DFT+\mathcal{U}}[\rho(\mathbf{r}), n] = E_{DFT}[\rho(\mathbf{r})] + \sum_l \left[\frac{\mathcal{U}^l}{2} \sum_{m,\sigma \neq m',\sigma'}' n_m^{l\sigma} n_{m'}^{l\sigma'} - \frac{\mathcal{U}^l}{2} n^l(n^l - 1) \right]. \tag{3.53}$$

Limiting the equation to a single orbital eigenvalue results in:

$$\varepsilon_m = \frac{\partial E_{DFT+\mathcal{U}}[\rho(\mathbf{r}), n]}{\partial n_m} = \varepsilon_m^{DFT} + \mathcal{U}(\frac{1}{2} - n_m). \tag{3.54}$$

The presence of n in each equation shows that the U parameter makes adjustments specific to an atom, and to a selected electron state m and orbital l within the atom. This being the case, the situations requiring GGA+U involve heavier atoms, and adjustments are often limited to only the electron state and orbital with the highest energy. In the case of SnS_2, the electron configurations at the highest energy level are $3s^2 3p^4$ for S and $5s^2 4d^{1}05p^2$ for Sn. For S, GGA+U will be applied to the 3p orbitals, while Sn has it applied to the 5p orbitals[14].

3.4 Hellmann-Feynman theorem

The Hellmann-Feynman theorem states if a functional value is stationary w.r.t. parameter, then the derivative of the functional can be derived from using only explicit dependence. It is possible to obtain the forces acting on nuclei I, using the derivative of total energy w.r.t. the nuclei positions R. From the existing approximations that can be made use of, assume that the system of nuclei are in equilibrium, giving a total force of zero:

$$\mathbf{F}_I = -\frac{\partial E}{\partial \mathbf{R}_I} = 0. \tag{3.55}$$

Evaluating this derivative requires the use of the Hellmann-Feynmann theorem, which is applicable for the energy eigenvalue $E(\lambda)$ of our hamiltonian $\hat{H}$. Then obtain the energy derivative w.r.t. the λ parameter:

$$\frac{\partial E}{\partial \lambda} = \langle \psi | \frac{\partial \hat{H}}{\partial \lambda} | \psi \rangle, \tag{3.56}$$

now making it possible to prove the correctness of applying the Hellmann-Feynmann theorem. This requires the application of derivation product rules being applied to the hamiltonian $\hat{H}$ derivative:

$$\hat{H} = \hat{T} + \hat{V}_{int} + \hat{V}_{ext} + \hat{H}_I. \tag{3.57}$$

We substitute the hamiltonian $\hat{H}$ into eq. 3.55, resulting in:

$$\begin{aligned}
\mathbf{F}_I &= -\langle\psi_0|\frac{\partial \hat{H}}{\partial \mathbf{R}_I}|\psi_0\rangle \\
&= -\langle\frac{\partial \hat{T}}{\partial \mathbf{R}_I}\rangle - \langle\frac{\partial \hat{V}_{int}}{\partial \mathbf{R}_I}\rangle - \langle\frac{\partial \hat{V}_{ext}}{\partial \mathbf{R}_I}\rangle - \frac{\partial E_n}{\partial \mathbf{R}_I}.
\end{aligned} \tag{3.58}$$

The kinetic and internal energy terms will vanish, having no explicit R dependence for a system using the Born-Oppenheimer approximation, resulting in the following equation for the force acting on nuclei:

$$\mathbf{F}_I = \int \frac{\partial \hat{V}_{ext}(\mathbf{r})}{\partial \mathbf{R}_I}\rho_0(\mathbf{r})d\mathbf{r} - \frac{\partial E_n}{\partial \mathbf{R}_I}. \tag{3.59}$$

This equation helps govern the process of atomic relaxation, through which nuclei are perturbed throughout the crystal lattice in an effort to minimize the forces acting on them, in an effort to reach equilibrium. The equilibrium state is preferred for obtaining more accurate total energies and derived results for a system of nuclei.

3.5 Application and calculations

Till this point, the foundational points of DFT, i.e. the HK theorems, have been discussed, and the the KS equations for simplifying the many-body problem were derived. To begin the practical application of the preceding theory, as applied to crystal lattice structures, it is first required to elaborate on the mathematical structure of crystal lattices.

The first subject to be introduced are periodic boundary conditions. Working with crystal lattices is simplified through the use of repeating unit cells, as calculations are applied only within the unit cell, or the larger scale super cell. The particles within the crystal lattice have position vectors $\mathbf{R}_n$.

An important aspect of the crystal lattice that results from its periodic nature is the reciprocal lattice. Points in the reciprocal lattice reside in the $\mathbf{k}$-space described as a set containing all points for which the $\mathbf{k}$-vector obtains a result $e^{i\mathbf{k}\cdot\mathbf{R}_n} = 1$.

Furthermore, lattice parameters in the real space a, b and c, are linked to their reciprocal lattice vector equivalents as $\kappa_1 = \frac{2\pi}{a}\hat{x}$, $\kappa_2 = \frac{2\pi}{b}\hat{y}$, and $\kappa_3 = \frac{2\pi}{c}\hat{z}$ within the $\mathbf{k}$-space. Additionally, the real space primitive cell has a reciprocal equivalent known as the first Brillouin zone (BZ), which will prove useful in simplifying the evaluation of material properties pertaining to energy.

3.5.1 Bloch's theorem

The spacial periodicity of a crystal lattice is partially described mathematically by the periodic KS potential:

$$V_{KS}(\mathbf{R}) = V_{KS}(\mathbf{r} + \mathbf{R}). \tag{3.60}$$

The periodic nature of the potential allows for the application of Bloch's theorem, which states that the wavefunction of an electron in a periodic potential can be described by the product of a wave-like function $e^{i\mathbf{k}\cdot\mathbf{r}}$ and a function to describe periodicity:

$$\phi_{j\mathbf{k}}(\mathbf{r}) = e^{i\mathbf{k}\cdot\mathbf{r}} f_{j\mathbf{k}}(\mathbf{r}) \tag{3.61}$$

Here, $\mathbf{k}$ is a wave vector within the first BZ. The lattice periodicity is described within by the $f_{j\mathbf{k}}$ function such that $f_{j\mathbf{k}}(\mathbf{r}) = f_{j\mathbf{k}}(\mathbf{r} + \mathbf{R})$. Similarly, a periodic energy spectrum can be described for the reciprocal lattice:

$$E_n(\mathbf{k}) = E_n(\mathbf{k} + \mathbf{G}), \tag{3.62}$$

for any reciprocal lattice vector $\mathbf{G}$. The concept of periodicity in the reciprocal lattice favours the defining a plane wave basis set for the periodic wavefunction. Eq. 3.61 adequately represents the entire energy spectrum contained within the first BZ. This energy spectrum is of particular importance and is called the band structure, which helps display the electronic structure of a material.

3.5.2 Plane wave basis set

The advantages of plane waves lie in their mathematical simplicity and completeness, and, in the case of the crystal lattice, the ability to cover the entire space evenly. The creation of a plane wave basis set allows for a representation of the wavefunction, such as representing the atomic wavefunctions with a basis set. Expanding the periodic function $f_{j\mathbf{k}}(\mathbf{r})$ to form this basis set uses $\mathbf{G}$, which is the reciprocal wave vector.

$$f_{j\mathbf{k}}(\mathbf{r}) = \sum_{\mathbf{G}} c_{j\mathbf{k}}(\mathbf{G}) e^{i\mathbf{G}\cdot\mathbf{r}} \tag{3.63}$$

In the above, $c_{j\mathbf{k}}(\mathbf{G})$ represents the plane wave coefficient, and the reciprocal space wave vectors $\mathbf{G}$ are the set of all vectors $\mathbf{G}$ that satisfy $\mathbf{G} \cdot \mathbf{R} = 2\pi n$, for bravais lattice vector $\mathbf{R}$ and integer n. Eq. 3.62 can be combined with the existing electronic wavefunction in eq. 3.60, completing the atomic wavefunction basis set:

$$\phi_{j\mathbf{k}}(\mathbf{r}) = \sum_{\mathbf{G}} c_{j,\mathbf{k}+\mathbf{G}} e^{i(\mathbf{k}+\mathbf{G})\cdot\mathbf{r}}. \tag{3.64}$$

From this equation it can be concluded that the KS equations are solvable by finding a finite number of electron wavefunctions per unit cell, though it is first required to calculate the plane wave coefficients $c_{j,\mathbf{k}+\mathbf{G}}$. There is, however, an infinite number of vectors $\mathbf{G}$, therefore requiring some limit being placed to bound these values and achieve a finite number of wavefunctions.

3.5.3 Kinetic energy cutoff

Inserting the plane wave basis set into the KS equations, then integrating over $\mathbf{r}$ results in the following equation:

$$\sum_{\mathbf{G}'} \left[\frac{1}{2}|\mathbf{k}+\mathbf{G}|^2 \delta_{\mathbf{G}\mathbf{G}'} + V_{II}(\mathbf{G}-\mathbf{G}') + V_{II}(\mathbf{G}-\mathbf{G}') + V_H(\mathbf{G}-\mathbf{G}') + V_{XC}(\mathbf{G}-\mathbf{G}') \right] c_{j,\mathbf{k}+\mathbf{G}'}$$
$$= \varepsilon_j c_{j,\mathbf{k}+\mathbf{G}}, \tag{3.65}$$

from which the first term in the summation is understood to be the kinetic energy of a plane wave in the reciprocal space. This summation can also be understood as the Hamiltonian matrix having undergone diagonalization. The coefficients $c_{j,\mathbf{k}+\mathbf{G}'}$ each have an associated kinetic energy, representing the diagonal elements of the Hamiltonian matrix. Of note is a tendency for the more important coefficients to be attached to low kinetic energies, which allows for the use of the cutoff energy parameter to place an upper bound on the plane wave basis set:

$$E_{cut} = \frac{|\mathbf{k}+\mathbf{G}_{max}|^2}{2} \tag{3.66}$$

During DFT calculations, the cutoff energy (E_{cut}) allows for a restriction to be placed on the number of plane waves, by removing all coefficients with kinetic energies above E_{cut} from the calculation. Equivalently, it can be stated that an upper bound has been placed on the value for wave vector $\mathbf{G}$, as signified by $\mathbf{G}_{max}$ in eq. 3.65.

The cutoff energy offers a considerable degree of control over the resolution of available detail, with any information falling beneath of the acceptable bound of the wavefunction (the inverse of the cutoff) being ignored. E_{cut} allows for the introduction of error into resultant data, however the degree of error can be decreased (while also increasing accuracy) by increasing the E_{cut} input. Decreasing the margin of error to an acceptable level occurs during convergence tests.

3.5.4 Brillouin zone integration

DFT calculations are capable of deriving quantities starting from the electron density. The electron density can be obtained from an integral in real space over the system, but this infinite integral is more difficult to evaluate. Rather, the finite integral over the first BZ of the reciprocal space is evaluated, which will obtain the same result as proven by Bloch's theorem. For the reciprocal space, the electron density is calculated as:

$$\rho(\mathbf{r}) = \int_{BZ} \sum_{n=1}^{N_{\mathbf{k}}} g_{n\mathbf{k}} |\psi_{n\mathbf{k}}(\mathbf{r})|^2 d\mathbf{k}, \tag{3.67}$$

for which summation is occurring over all occupied bands, while $g_{n\mathbf{k}}$ determines the occupancy of each band, being 1 below the Fermi level or 0 otherwise. The computational solving of this integral for the continuous variable $\mathbf{k}$ is in no way efficient, and it is required to approximate the integral for a sampled set of k-points.
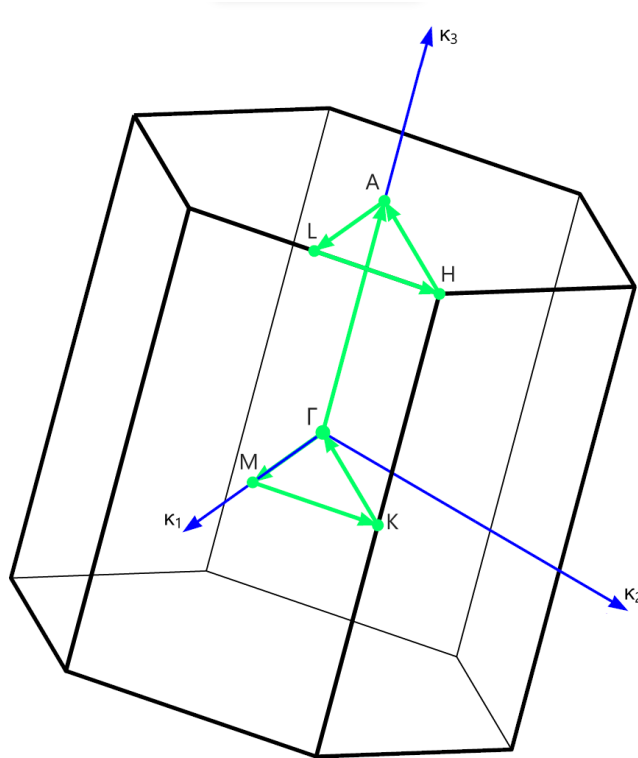
Figure 3.1: Primitive Brillouin Zone for SnS_2, with symmetry points labelled.

For the obtainment of band structures, paths through the BZ are selected, intersecting with symmetry points as seen in the example of figure 3.1. Multiple points along each path are used as the sampled set of k-points for the integral.

For other calculations that ignore the band structure, it is possible to generate an grid of k-points, known as a Monkhorst-Pack grid[15], that divides up the BZ into equidistant points. Sampling of the irreducible Brillouin zone (IBZ), which further reduces the first BZ based on lattice symmetry, should be sufficient for calculating the electron density. The equation for generating the Monkhorst-Pack grid is given by:

$$\mathbf{k}_{1,2,3} = \sum_{i=1}^{3} \frac{2n_i - N_i - 1}{2N_i} \mathbf{G}_i, \tag{3.68}$$

If the IBZ has been used, a weight coefficient $w_{\mathbf{k}}$, which takes into account how often k-points in IBZ are repeated over the entire first BZ, must be added to eq. 3.67. Following the implementation of k-point sampling, the resulting electron density will be:

$$\rho(\mathbf{r}) \cong \sum_{\mathbf{k} \in IBZ} w_{\mathbf{k}} \sum_{n=1}^{N_{\mathbf{k}}} g_{n\mathbf{k}} |\psi_{n\mathbf{k}}(\mathbf{r})|^2 d\mathbf{k}. \tag{3.69}$$

An additional challenge lies in the presence of the Fermi step in occupations, which, if required, can be addressed through the inclusion of the Methfessel-Paxton smearing method[16]. This will smooth the sharp drop at the Fermi level, allowing for faster convergence for especially small k-point grids.

44

3.5.5 Pseudopotentials

Now that the periodic system is described using a plane wave basis set, the DFT method can be applied. However, the orbitals of the entire system contains many nodes and oscillates rapidly nearer to the nucleus. This increases the size of the basis set considerably, which in turn leads to a much higher E_{cut} being required to adequately calculate the properties of the system.

Nearer to the nucleus are the core electrons of an atom, which are responsible for a large majority of rapid wavefunction oscillations. Unlike valence electrons (which have smoother wavefunctions), core electrons are rarely, if ever, of relevance to bonding, which in turn means that core electrons are not as important for the derivation of material properties. This being the case, the motion of core electrons are safe to ignore during DFT calculations, and the core electrons can be approximated in some way.

The pseudopotential method attempts this by freezing the core electrons in place, such that the remaining valence electrons experience instead an effective potential, the pseudopotential, made up of the electron-nucleus and core-valence interactions. This new pseudopotential will have a much smoother wavefunction, decreasing the size of the plane wave basis set to a more efficient value. Figure 3.2 illustrates the difference between the all-electron (AE) potential and pseudo potential, as well as their respective wavefunctions.

The basis of the pseudopotential was introduced in 1934, with Fermi and studying alkali atom energy levels[17]. Later in 1958, the empirical pseudopotential method, capable of accurately describing band structures was pioneered, with the drawback of requiring large amounts of experimental results on semiconductor energy levels to produce wavefunctions[18]. To further improve the pseudopotential required the application of *ab initio* methodology, which resulted in several variations, such as the norm-conserving and ultrasoft pseudopotentials.

Norm-conserving pseudopotentials were introduced in 1979[19], requiring (*i*) identical AE and pseudo-wavefunction energies, (*ii*) being identical beyond the cutoff radius r_c, (*iii*) and having the same charge inside r_c. These conditions are mostly ignored by ultrasoft pseudopotentials (by Vanderbilt and Blöchl in 1990[20]), further reducing the size of the basis set and reducing Fourier components needed in describing valence electrons.

One of the most recent of *ab initio* pseudopotential approximations is the projector augmented wave (PAW) pseudopotential. The PAW method, developed by Blöchl in 1994[21], retains AE characteristics in the wavefunction, making it generally more accurate than other pseudopotential methods.

3.5.6 Projector augmented wave pseudopotential

There is a close relation between the general pseudopotential and PAW methods, as the latter still attempts to distinguish between oscillating core orbitals and the smoother valence orbitals. However, the PAW method is designed to also conserve the all-electron characteristics of the wavefunction. The description of how this is done follows[22].

For a single atom, the single electron wavefunctions ϕ_i of the AE orbitals are initially obtained from all-electron calculations. As with pseudopotential methods, these are transformed into the smoother wavefunctions $\tilde{\phi}_i$, which produce partial waves. The true and partial waves must match beyond the cutoff r_c, and converting between the two makes use of a linear transformation operator $\mathcal{T}$:
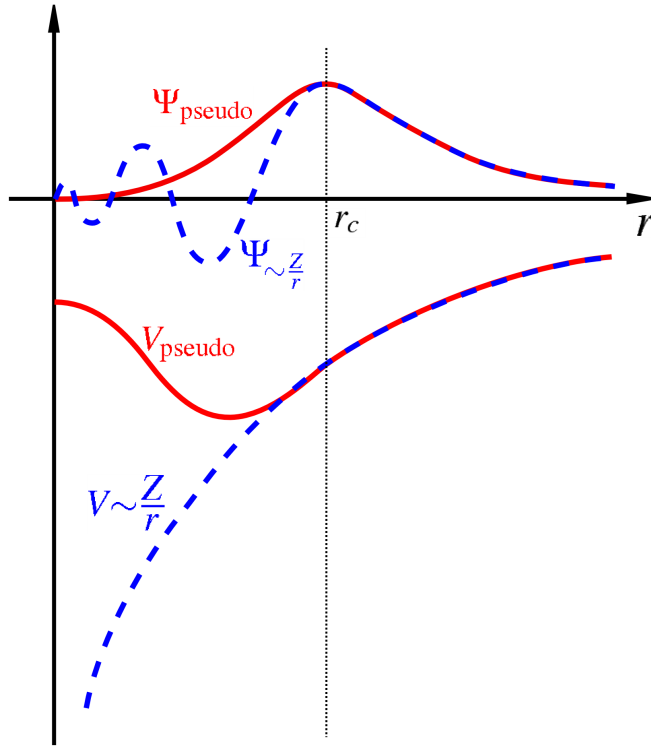
Figure 3.2: All-electron potential (dashed curve), the pseudopotential (solid curve) and their wavefunctions. Beyond r_c, the cutoff radius, the pseudo- and all-electron values match.

$$\phi_i = \mathcal{T}\tilde{\phi}_i. \tag{3.70}$$

Next, the smooth wavefunctions for valence electrons are expanded for interaction with other atoms, obtaining:

$$\tilde{\Phi}_i = \sum_i c_i \tilde{\phi}_i, \tag{3.71}$$

which in combination with eq. 3.70 reads as:

$$\Phi_i = \mathcal{T}\left(\sum_i c_i \tilde{\phi}_i\right) = \sum_i c_i \phi_i. \tag{3.72}$$

The operator $\hat{T}$ has yet to be defined, requiring first the projectors p_i, which act only within the core region, be defined:

$$\langle p_i | \tilde{\phi}_i \rangle = \delta_{ij}. \tag{3.73}$$

Projectors allow for the following definition of operator $\hat{T}$:

$$\mathcal{T} = 1 + \sum_j \left(|\phi_i\rangle - |\tilde{\phi}_i\rangle\right) \langle p_i|, \tag{3.74}$$

which when inserted into eq. 3.70, along with the use of eq. 3.73, results in:

$$|\phi_i\rangle = \mathcal{T}|\tilde{\phi}_i\rangle = |\tilde{\phi}_i\rangle + \sum_j \left(|\phi_i\rangle - |\tilde{\phi}_i\rangle \right)\delta_{ij}. \tag{3.75}$$

and the same can be done with the true electron wavefunction for the system in eq. 3.72:

$$|\Phi_i\rangle = \mathcal{T}|\tilde{\Phi}_i\rangle = |\tilde{\Phi}_i\rangle + \sum_j \left(|\phi_i\rangle - |\tilde{\phi}_i\rangle \right)\langle p_i|\tilde{\Phi}_i\rangle. \tag{3.76}$$

The above equation allows for the calculation of any of the physical properties of a material, which is done by reconstructing the AE wavefunction from the smooth pseudo-wavefunctions. Reconstruction occurs through the correcting of differences between true orbitals ϕ_i and the partial waves $\tilde{\phi}_i$. This allows the PAW method to retain AE characteristics, as well as a higher accuracy in general when compared to other pseudopotential methods. Additionally, a lower cutoff energy E_{cut} is necessary for good accuracy levels, increasing computational efficiency. With these advantages, PAW pseudopotentials are the choice for all computations done throughout dissertation.

3.6   Software options

Density functional theory has successfully simplified the many-body problem. Having reached the KS equations which can be solved self-consistently, the only requirements are that a sufficiently large basis set is chosen, as well as the implementation of larger supercells to solve more complex systems of particles. These requirements are much more easily solved computationally, and the numerical implementation of DFT has led to a wide variety of software options for solving systems. DFT Software packages include BigDFT, CPMD, DMol^3, SIESTA, Quantum ESPRESSO, VASP, etc. Differences between software packages include implementation of basic functions, pseudopotentials, and algorithms, as well as the general user experience and usage of computational resources. For the results calculated during this dissertation, Quantum ESPRESSO (QE) was used, and as such, the details regarding its implementation and capabilities will be expanded upon. These details are largely extracted from the user guide, as well as the guides detailing the usage of the `PWscf`, `PWneb`, and `PostProc` packages[23].

3.6.1   Overview of Quantum ESPRESSO

The Quantum ESPRESSO distribution is developed under the coordination of Paolo Giannozzi (University of Udine and IOM-CNR, Italy) and Pietro Delugas (SISSA Trieste), with the intention for research into and simulation of electronic structures, and their optimization[24]. The distribution consists of several component software packages, with the core packages being `PWscf` and `CP`, used for calculating electronic structure properties using DFT, plane wave basis sets, and pseudopotentials. QE is built to take advantage of the CPU. However, an alternative branch developed in parallel by Pietro Bonfà (University of Parma), ports the current QE version over to a GPU enabled version. This alternate branch can be used instead so as to enable GPU support in addition to the use CPU for running calculations.

Of relevance to the dissertation, `PWscf` is responsible for self-consistent field (SCF) calculations, but is also capable of non-self-consistent field (NSCF) calculations. It is capable of obtaining ground state

energy, KS orbitals, atomic forces, and stresses. `PWscf` is also responsible for structural optimization, having relax and variable cell relax calculations as a subset of its calculation types. The software package is known to work for insulators and metals in any crystal structure. `PWscf` can solve most XC functionals, for variations such as spin polarization and DFT+U, and is capable of working with norm-conserving pseudopotentials, ultrasoft pseudopotentials, as well as using the PAW method.

`Pwneb` builds on top of the `PWscf` package. It requires an optimized initial and final structure as an input for applying the nudged elastic band (NEB) method. This is applied so as to find a path of least resistance for the diffusion of a particle through a crystal lattice, with this particle having different positions in the initial and final structure. These paths and their extremes can then be further optimized with the additional application of the climbing image NEB method.

The `PostProc` package is capable of processing the data obtained from `PWscf` for a variety of organized results. Primarily, this is through the use of the `pp.x` executable to extract specific data from the `PWscf` output files, such are charge density, various potentials, and local density of states. Also included as part of this package, are executables for the plotting of partial and total density of states, as well as band structures along an input k-path.

Regarding the optimization of running QE, the software suite is capable of performing calculations with the help of parallelism. The message passing interphase (MPI) allows for a copy of executable runs to take place on each CPU of a system, taking advantage of a system containing multiple processors. OpenMP allows for a single executable to have multiple subprocesses (threads) to perform specific tasks in parallel.

Note, for this particular dissertation, in the case of larger supercells containing upwards of 25 atoms, in an effort to save time these calculations are run on a more powerful supercomputer system. The larger systems are computed with the help of the NICIS Centre for High Performance Computing and the Lengau cluster supercomputer, with over 30 000 cores rated for more than 1000 teraflops[25].

3.6.2 Input and output

Preliminary calculations are often required before running more complicated calculations, which would be either an SCF calculation or structural optimization. Running the QE executable `pw.x` for these preliminary calculations requires an input file `file.in`, along with pseudopotential files in the unified format `element_and_type.UPF` for each element present in the unit cell.

The parameters required for `file.in` are divided into sections, starting a namelist of options. First `&CONTROL` for deciding type of calculation, the location of pseudopotential files resulting outputs, among other settings. `&SYSTEM` needs all the structural information of the system, most importantly lattice parameters, the number of and the number of types of atoms, occupation type for metallic systems, smearing, and Hubbard U parameters. The kinetic energy cutoff for expansion of plane wavefunctions will be determined following convergence tests, while the cutoff for charge densities and potentials was set to 300 Ry ($\sim$4000 eV). The Hubbard U parameter is also determined from convergence tests. The electronic occupancy was set using the Gaussian smearing method[26], with a spread of 0.01 Ry.

`&ELECTRONS` determines the maximum iterations for SCF calculations, as well as the convergence threshold, the estimated error for total energy, after which calculations can be concluded. Energy and force criteria were set to converge for differences less than 1×10^{-4} eV and 1×10^{-3} eV/Å, respectively. The

remaining namelists are optional for SCF calculations, though structural optimization or NSCF will need them enabled.

Following these namelists, there are input regions for the types of atoms, their atomic mass, and their pseudopotential files, followed by inputting `K_POINTS` (either as a grid, along a path, or each individual point) and `ATOMIC_POSITIONS` for every atom within the unit cell. The k-points will need to undergo convergence tests to determine the best choice for accuracy and efficiency. For the description of the electron exchange correlation potential, the generalized gradient approximation (GGA) was chosen through the Perdew-Burke-Ernzerhof (PBE) flavour[7], which is reflected by the pseudopotential files.

`pw.x` has an output `file.out`, which in general will logs all actions during calculations. Total energy is recorded following SCF calculations, or Fermi energy E_F following NSCF calculations. During structural optimization, `file.out` records the changes in atomic positions and unit cell structure along with total energy for each step, as the system nears equilibrium.

Running any other executable must always take place following an SCF calculation, and quite often also an NSCF calculation as well. These two sequential calculations should provide enough raw data that can be processed for any result that QE is capable of. That is specifically what the `PostProc` package is used for, with the executable `pp.x` extracting specific results as selected in its input file, such as electron charge density, total potential, or magnetization. The k-mesh will be doubled in size to correctly apply the Hubbard U corrections for the band gap, along with using the Tetrahedra method[27] for electron occupancy, which gives a better estimate when calculating DOS.

The `PostProc` also has multiple executables for the preperation of DOS plots (`dos.x` for TDOS and `projwfc.x` for PDOS) or band structure plots (after a bands calculation with `pw.x`, `bands.x` extracts the data). For these results, `file.out` will only log the progress of the calculation, while the resulting data is given its own `file.dat` data file free of commentary, simplifying the process of plotting the results.

The `Pwneb` requires multiple images of the system, represented by optimized atomic positions for the system in which a single atom has changed positions, as input for the `neb.x` executable. To investigate Li/Na diffusion across the surface of the pristine and vacancy defect SnS_2 monolayers, the nudged elastic band (NEB) method[28] was used. The minimum energy path of the single atom between these points will then be calculated through repeated SCF and relaxation calculations, making this procedure especially intensive to compute. The resulting output will have `file.out` summarizing the results, with total energies given to each point along the path at each step of the process, along with the margin of error (which also determines when the calculation is concluded) and the activation energy required to move along the path. Additionally, the output `file.path` will have the atomic positions for each point along the resultant minimum energy path.

These inputs were all used for the extent of this dissertation. Executable `pw.x` will optimize the atomic structures and find total energies required to obtain additional results. We use `neb.x` to determine the minimum energy paths for diffusion across the substrate surface, which in turn locates preferred sites for ion occupation. Data was extracted and processed as necessary using `dos.x` and related executables, for the creation of TDOS plots as necessary.

Bibliography

[1] P. Hohenberg and W. Kohn. Inhomogeneous Electron Gas. *Phys. Rev.*, 136:B864–B871, Nov 1964. doi: 10.1103/PhysRev.136.B864. URL `https://link.aps.org/doi/10.1103/PhysRev.136.B864`.

[2] W. Kohn and L. J. Sham. Self-Consistent Equations Including Exchange and Correlation Effects. *Phys. Rev.*, 140:A1133–A1138, Nov 1965. doi: 10.1103/PhysRev.140.A1133. URL `https://link.aps.org/doi/10.1103/PhysRev.140.A1133`.

[3] P. A. M. Dirac. Note on Exchange Phenomena in the Thomas Atom. *Mathematical Proceedings of the Cambridge Philosophical Society*, 26(3):376–385, 1930. doi: 10.1017/S0305004100016108.

[4] Richard M Martin. *Electronic structure: basic theory and practical methods*. Cambridge university press, 2020.

[5] D. M. Ceperley and B. J. Alder. Ground State of the Electron Gas by a Stochastic Method. *Phys. Rev. Lett.*, 45:566–569, Aug 1980. doi: 10.1103/PhysRevLett.45.566. URL `https://link.aps.org/doi/10.1103/PhysRevLett.45.566`.

[6] J.F. Dobson, G. Vignale, and M.P. Das. *Electronic Density Functional Theory: Recent Progress and New Directions*. Springer US, 2013. ISBN 9781489903167. URL `https://books.google.co.za/books?id=4OvvBwAAQBAJ`.

[7] John P. Perdew, Kieron Burke, and Matthias Ernzerhof. Generalized Gradient Approximation Made Simple. *Phys. Rev. Lett.*, 77:3865–3868, Oct 1996. doi: 10.1103/PhysRevLett.77.3865. URL `https://link.aps.org/doi/10.1103/PhysRevLett.77.3865`.

[8] Philipp Haas, Fabien Tran, Peter Blaha, Karlheinz Schwarz, and Robert Laskowski. Insight into the performance of GGA functionals for solid-state calculations. *Phys. Rev. B*, 80:195109, Nov 2009. doi: 10.1103/PhysRevB.80.195109. URL `https://link.aps.org/doi/10.1103/PhysRevB.80.195109`.

[9] J Kohanoff and Nikitas Gidopoulos. Density Functional Theory: Basics, New Trends and Applications. *Handbook of Molecular Physics and Quantum Chemistry*, 2, 01 2003.

[10] John P. Perdew. Density functional theory and the band gap problem. *International Journal of Quantum Chemistry*, 28(S19):497–523, 1985. doi: https://doi.org/10.1002/qua.560280846. URL `https://onlinelibrary.wiley.com/doi/abs/10.1002/qua.560280846`.

[11] Vladimir I. Anisimov, Jan Zaanen, and Ole K. Andersen. Band theory and Mott insulators: Hubbard U instead of Stoner I. *Phys. Rev. B*, 44:943–954, Jul 1991. doi: 10.1103/PhysRevB.44.943. URL `https://link.aps.org/doi/10.1103/PhysRevB.44.943`.

[12] Manolo C Per and Deidre M Cleland. Roadmap on post-DFT methods for nanoscience. *Nano Futures*, 4(3):032004, Aug 2020. doi: 10.1088/2399-1984/aba109. URL `https://dx.doi.org/10.1088/2399-1984/aba109`.

[13] Sarah A. Tolba, Kareem M. Gameel, Basant A. Ali, Hossam A. Almossalami, and Nageh K. Allam. The DFT+U: Approaches, Accuracy, and Applications. In Gang Yang, editor, *Density Functional Calculations*, chapter 1. IntechOpen, Rijeka, 2018. doi: 10.5772/intechopen.72020. URL `https://doi.org/10.5772/intechopen.72020`.

[14] Nicole E. Kirchner-Hall, Wayne Zhao, Yihuang Xiong, Iurii Timrov, and Ismaila Dabo. Extensive Benchmarking of DFT+U Calculations for Predicting Band Gaps. *Applied Sciences*, 11(5):2395, Mar 2021. doi: 10.3390/app11052395. URL `https://doi.org/10.3390%2Fapp11052395`.

[15] Hendrik J. Monkhorst and James D. Pack. Special points for Brillouin-zone integrations. *Phys. Rev. B*, 13:5188–5192, Jun 1976. doi: 10.1103/PhysRevB.13.5188. URL `https://link.aps.org/doi/10.1103/PhysRevB.13.5188`.

[16] M. Methfessel and A. T. Paxton. High-precision sampling for Brillouin-zone integration in metals. *Phys. Rev. B*, 40:3616–3621, Aug 1989. doi: 10.1103/PhysRevB.40.3616. URL `https://link.aps.org/doi/10.1103/PhysRevB.40.3616`.

[17] Enrico Fermi et al. Motion of neutrons in hydrogenous substances. *Ricerca Scientifica*, 7(2):13–52, 1936.

[18] James C. Phillips. Energy-band interpolation scheme based on a pseudopotential. *Phys. Rev.*, 112: 685–695, Nov 1958. doi: 10.1103/PhysRev.112.685. URL `https://link.aps.org/doi/10.1103/PhysRev.112.685`.

[19] D. R. Hamann, M. Schlüter, and C. Chiang. Norm-conserving pseudopotentials. *Phys. Rev. Lett.*, 43:1494–1497, Nov 1979. doi: 10.1103/PhysRevLett.43.1494. URL `https://link.aps.org/doi/10.1103/PhysRevLett.43.1494`.

[20] David Vanderbilt. Soft self-consistent pseudopotentials in a generalized eigenvalue formalism. *Phys. Rev. B*, 41:7892–7895, Apr 1990. doi: 10.1103/PhysRevB.41.7892. URL `https://link.aps.org/doi/10.1103/PhysRevB.41.7892`.

[21] P. E. Blöchl. Projector augmented-wave method. *Phys. Rev. B*, 50:17953–17979, Dec 1994. doi: 10.1103/PhysRevB.50.17953. URL `https://link.aps.org/doi/10.1103/PhysRevB.50.17953`.

[22] Peter E. Blöchl, Clemens J. Först, and Johannes Schimpl. Projector augmented wave method:ab initio molecular dynamics with full wave functions. *Bulletin of Materials Science*, 26(1):33–41, Jan 2003. ISSN 0973-7669. doi: 10.1007/BF02712785. URL `https://doi.org/10.1007/BF02712785`.

[23] Documentation, Nov 2022. URL `https://www.quantum-espresso.org/documentation/`.

[24] Paolo Giannozzi, Stefano Baroni, Nicola Bonini, Matteo Calandra, Roberto Car, Carlo Cavazzoni, Davide Ceresoli, Guido L Chiarotti, Matteo Cococcioni, Ismaila Dabo, Andrea Dal Corso, Stefano de Gironcoli, Stefano Fabris, Guido Fratesi, Ralph Gebauer, Uwe Gerstmann, Christos Gougoussis, Anton Kokalj, Michele Lazzeri, Layla Martin-Samos, Nicola Marzari, Francesco Mauri, Riccardo Mazzarello, Stefano Paolini, Alfredo Pasquarello, Lorenzo Paulatto, Carlo Sbraccia, Sandro Scandolo,

Gabriele Sclauzero, Ari P Seitsonen, Alexander Smogunov, Paolo Umari, and Renata M Wentzcovitch. QUANTUM ESPRESSO: a modular and open-source software project for quantum simulations of materials. *Journal of Physics: Condensed Matter*, 21(39):395502, 2009. doi: 10.1088/0953-8984/21/39/395502. URL `https://doi.org/10.1088%2F0953-8984%2F21%2F39%2F395502`.

[25] Wiki.chpc.ac.za, Jun 2022. URL `https://wiki.chpc.ac.za/chpc:lengau`.

[26] C. L. Fu and K. M. Ho. First-principles calculation of the equilibrium ground-state properties of transition metals: Applications to Nb and Mo. *Phys. Rev. B*, 28:5480–5486, Nov 1983. doi: 10.1103/PhysRevB.28.5480. URL `https://link.aps.org/doi/10.1103/PhysRevB.28.5480`.

[27] Peter E. Blöchl, O. Jepsen, and O. K. Andersen. Improved tetrahedron method for Brillouin-zone integrations. *Phys. Rev. B*, 49:16223–16233, Jun 1994. doi: 10.1103/PhysRevB.49.16223. URL `https://link.aps.org/doi/10.1103/PhysRevB.49.16223`.

[28] Hannes Jónsson, Greg Mills, and Karsten W. Jacobsen. *Classical and Quantum Dynamics in Condensed Phase Simulations*, chapter Nudged elastic band method for finding minimum energy paths of transitions, pages 385–404. World Scientific, 1998. doi: 10.1142/9789812839664_0016. URL `https://www.worldscientific.com/doi/abs/10.1142/9789812839664_0016`.

Chapter 4

Results and Discussion

Having explored the existing research and information regarding SnS_2 monolayers, as well as the foundations of DFT and the principles of its application, we will now elaborate on the data we obtained in our own exploration of the material. We go over the initial structure of SnS_2, and how it can be optimized to obtain more accurate results, then go on to look at the lithiation and sodiation of the surface, and how the ions will interact between adatoms and vacancy defects on the substrate surface. Results will be interspersed with explanations, as required, of properties and their meaning, and how they are derived from the base data.

4.1 Structural aspects of the SnS_2 monolayer

Monolayer tin disulfide has two phases, 1T and 1H, which differ in structure as detailed in section 1.1.3. Both structures have an Sn layer sandwiched between two S layers, and have a hexagonal prism unit cell. The difference in their structures lies in the offset between the S layers. For 1H, the S atoms in both layers have the same corresponding xy-plane atomic positions, fitting the overall unit cell into the $P\bar{6}m2$ (trigonal prismatic) space group. The 1T unit cell has the S layers are mirrored across the xy-plane, and fit into the close packed $P\bar{3}m2$ (octahedral) space group.

The structures for 1T- and 1H-SnS_2 are shown in figure 4.1, displaying the preliminary unit cell structures prior to any structural optimization. The initial lattice constant a was set to 3.638 Å, and has the same magnitude as lattice constant b. The lattice constant c (the equivalent of interlayer distance) was set to 10.0 Å, isolating the individual SnS_2 layers to emulate a monolayer, while also avoiding interlayer interactions.

Experimental coordinates are set for preliminary 1T- and 1H-SnS_2 unit cells. The Sn atomic position is set to $\left(0, 0, \frac{c}{2}\right)$ at the xy-origin, while along the z-axis the atom is placed at the center of the unit cell. For 1H-SnS_2, the S atomic positions are set to $\left(\frac{a}{3}, \frac{2a}{3}, \frac{c}{2} \pm 1.25\text{Å}\right)$, +1.25 for the top layer S atoms and −1.25 for the bottom layer S atoms. For 1T-SnS_2, the top layer S atomic positions are set to $\left(\frac{a}{3}, \frac{2a}{3}, \frac{c}{2} + 1.25\text{Å}\right)$, while the bottom layer atomic positions are $\left(\frac{2a}{3}, \frac{a}{3}, \frac{c}{2} - 1.25\text{Å}\right)$. The Sn–S bond lengths are initially set to 2.442 Å, with the placement of S atoms on the z-axis giving both monolayers a thickness (measured between layers S↔S) of 2.490 Å.

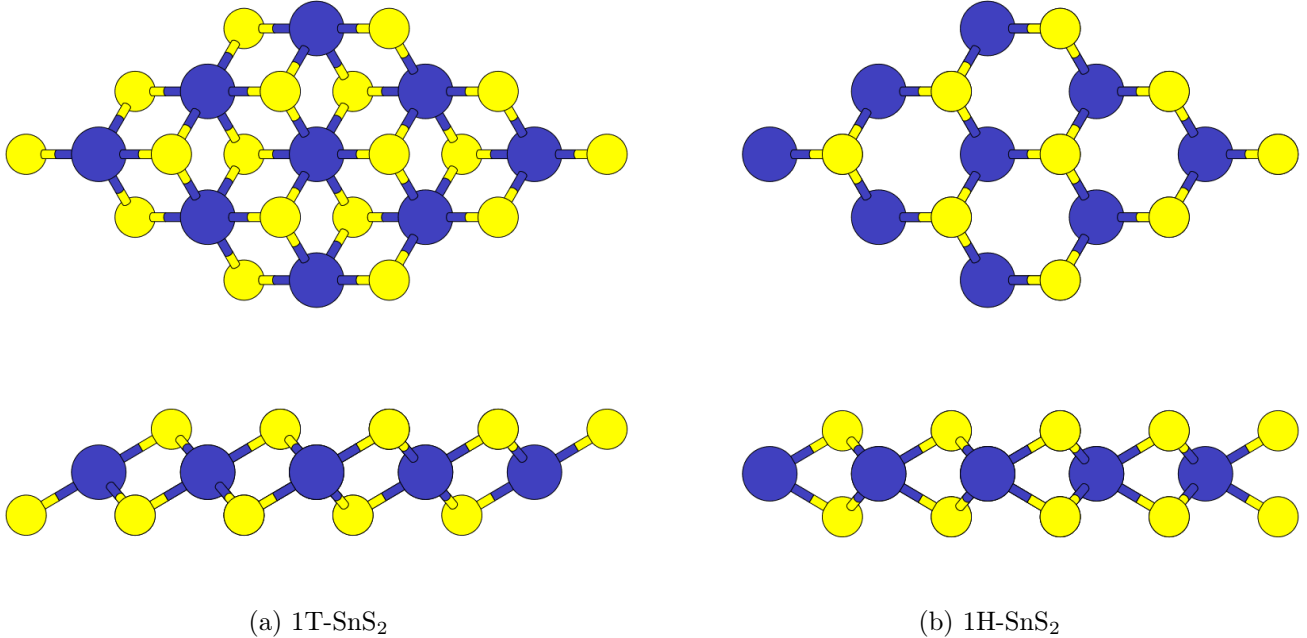(a) 1T-SnS$_2$ (b) 1H-SnS$_2$

Figure 4.1: The top views (top row) and side views (bottom row) of the SnS$_2$ monolayer phases, 1T and 1H.

4.2   Tests of convergence for input parameters

Before electronic and structural properties for the SnS$_2$ monolayer can be calculated (as relevant to its usage as an anode material), various decisions must be made regarding the input parameters; the atomic positions/phase, lattice constants, cutoff energy E_{cut}, k-points, and U parameter. Firstly, a decision should be made regarding which of the SnS$_2$ monolayer phases, 1T or 1H, are more suitable for acting as an anode material, through an investigation of their energetic stability. This is done through a comparison of equilibrium lattice parameters and cohesive energies E_C, the former of which can be obtained from relax calculations, the latter from self-consistent field (SCF) calculations. We compare the E_C values of 1T and 1H to determine their respective structural stability, as a higher cohesive energy in general suggests a higher degree of structural energetic stability.

Second, the QE input variable parameters, such as E_{cut} and k-points, must be decided following a series of convergence tests. Once more, this is done using a comparison of resultant cohesive energies following a series of SCF calculations. Computing the cohesive energy rather than simply focusing on the total energy allows for an immediate comparison to experimentally measurable values. The total energy of a system is dependant on the arbitrary size of the system, thus will not be consistent between experiments of variable initial conditions. E_C is limited to a single unit cell, while also being dependent on the number of atoms in the unit cell. Cohesive energy results obtained during convergence tests are reported in units of eV/atom. The formula for calculating E_C is[1]:

$$E_C = \frac{|E_{cell} - \sum E_{isolated}|}{n},$$ (4.1)

where the sum of the isolated atom energies $E_{isolated}$ of the cell is subtracted from the total unit cell

54

or supercell energy E_{cell}, after which the result is divided by the number of atoms n in the cell.

Improving the unit cell parameters and SnS_2 structure employs three levels of optimization; zero optimization for an unrelaxed structure, atomic position optimization via relaxation calculations, and full optimization via variable cell (VC) relaxation calculations. For each level, a series of SCF calculations were performed for convergence tests (figure 4.3). The preliminary 1H- and 1T-SnS_2 unit cells have undergone zero optimization. Following the first set of convergence tests, the second pair of SnS_2 unit cells have undergone atomic position optimization. This relaxation minimizes the forces acting on the system, bringing the unit cells closer to equilibrium. The final pair of SnS_2 unit cells have undergone full optimization, for which VC relaxation calculations have improved the shape and volume of the relaxed unit cell, adjusting lattice constants and cell angles. The results of these convergence tests should allow us to identify and choose the more stable SnS_2 monolayer phase and its input parameters for future calculations.

4.2.1 Lattice constants

(a) E_C as function of lattice constant a. (b) E_C as function of lattice constant c.
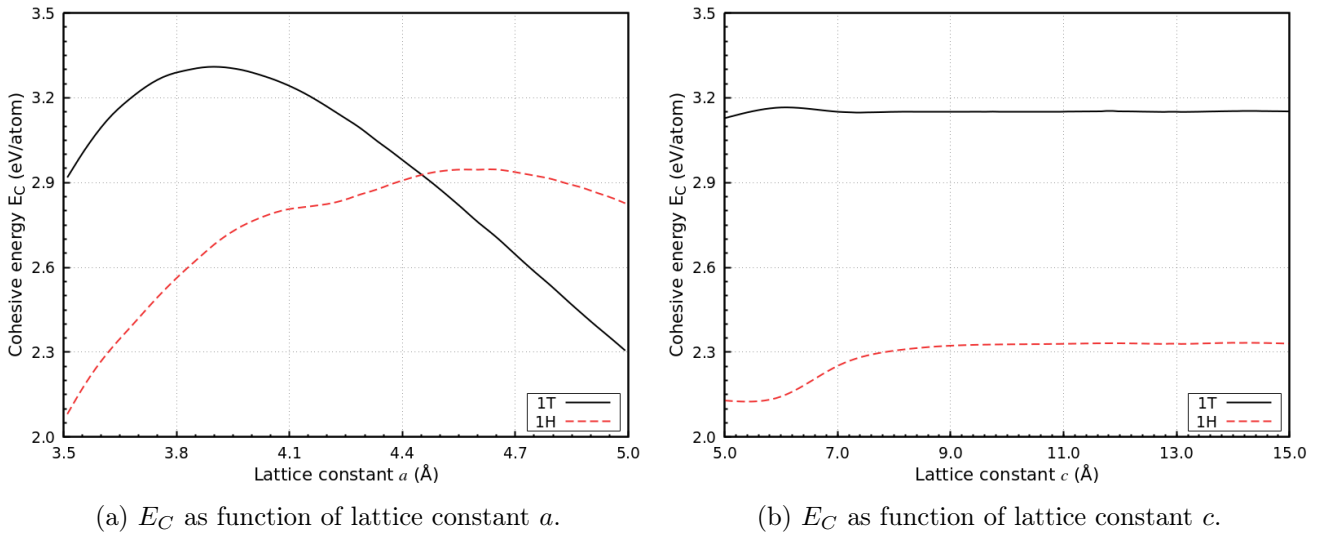
Figure 4.2: Variation in cohesive energy as the lattice constants are increased.

Existing literature suggests that the 1T-SnS_2 monolayer phase is more stable than 1H-SnS_2[2]. To support this information and confirm the choice of phase, the lattice constant a of the SnS_2 monolayer unit cell, for both 1T and 1H, is varied within a 20% range around a starting value of 3.9 Å. The resulting data was plotted with the hope of finding a local maximum near this starting value, the maximum representing our equilibrium cohesive energy E_C of the unit cell. The resulting plots are displayed in figure 4.2. In figure 4.2a, the plot for 1H shows a maximum E_c of 3.0 eV/atom corresponding to lattice constant a of 4.7 Å. The plot for 1T shows a maximum E_C of 3.3 eV/atom corresponding to lattice constant a of 3.8 Å. We can see that the 1T-SnS_2 phase has a higher E_C than 1H-SnS_2. This is an indication that 1H will more easily disintegrate than 1T, in agreement with previous studies[2].

The obtained a for 1H-SnS_2 at maximum E_C is considerably larger than experimental values, likely resulting from the lack of structural optimization, and is unsuitable as an input parameter. For both phases, their cohesive energies are lower than the existing values of Bacaksiz et $al.$[2]. To obtain improvements for the lattice constant a results, VC relaxation calculations were performed. The initial lattice constant

a for both unit cells is 3.64 Å, and following the VC relaxation, lattice constant a decreased to 3.55 Å for 1H-SnS$_2$, and increased to 3.71 Å for 1T-SnS$_2$. There is an agreement between the latter 1T result and the expected experimental value of 3.65 Å[3], as well as comparable GGA measurements of 3.70 Å for 1T-SnS$_2$ and 3.62 Å for 1H-SnS$_2$[4].

For lattice constant c, which in the case of monolayer SnS$_2$ represents the interlayer distance, convergence tests were performed to find the lower bound for interlayer interactions. A sufficiently large c must be chosen to mitigate these interactions. Figure 4.2b shows us that, for both 1T and 1H, lattice constant c only begins to converge to constant cohesive energies for c greater than 8.00 Å. Choosing any value greater than 8.00 Å will be sufficient to significantly reduce interlayer interactions, preventing them from interfering with the monolayer results. In future calculations, the input interlayer distance will be set to 15.0 Å, adding extra space to the unit cell to allow for added atoms on top of the substrate.

4.2.2 Cutoff energy

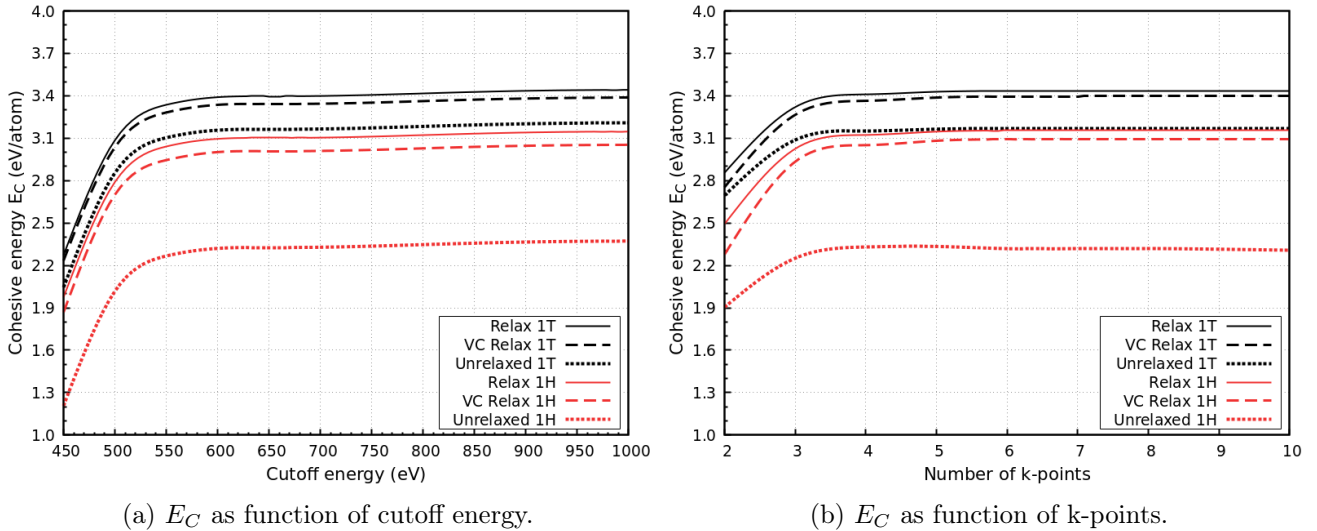(a) E_C as function of cutoff energy.   (b) E_C as function of k-points.

Figure 4.3: Variation in cohesive energy E_C with respect to increasing (a) cutoff energy and (b) number of k-points. Cohesive energies plotted are for the unrelaxed (experimental coordinates), relaxed, and VC relaxed unit cells of 1T-SnS$_2$ and 1H-SnS$_2$.

As detailed in section 3.5.3, the cutoff energy E_{cut} places a limit on the accuracy of the total energy computed for a system of particles. The increase in cutoff energy improves the accuracy of the system, but the higher cutoff will also cost us computational time. Also, at some point the number of plane waves will reach a limit beyond which accuracy will no longer improve. E_{cut} is balanced between these bounds, with the application of tests of convergence allowing us to find a point at which results remains fairly consistent.

Figure 4.3a presents the variation in E_C for both 1T and 1H. The cutoff energy E_{cut} is increased from 450 eV to 1000 eV, for increments of 50 eV. The Monkhorst-Pack grid was set to an arbitrary size of $3 \times 3 \times 1$ for the duration of cutoff energy convergence tests. For both SnS$_2$ structures at all optimization levels, E_C quickly begins to plateau between 500 and 600 eV, with all plots in figure 4.3a having converged beyond 600 eV. There is still a continuous increase in cohesive energies for all optimization levels, which

results in less than 1% overall difference, making it is negligible.

Starting with the 1T unit cell, the cutoff energy E_C converges at 3.20 eV, and the convergence for the 1H unit cell is at a considerably lower E_C of 2.35 eV, both values obtained from SCF calculations. After relaxation and performing a new set of SCF calculations, E_C for 1T increases up to 3.44 eV, and E_C for 1H up to 3.14 eV. The large increase in E_C for 1H-SnS$_2$ shows that there is a considerable necessity for atomic position optimization when working with multiple structural polytypes. After VC relaxation and performing another set of SCF calculations, figure 4.3a shows a slight decrease in E_C for both unit cells, by a margin of 0.05-0.08 eV. This shows that only a slight correction to the unit cell structure is necessary. Overall, we see that the 1T-SnS$_2$ phase has a higher E_C than 1H-SnS$_2$, supporting our supposition that the former is energetically more stable.

In the obtained data, for all cutoff energies over 600 eV, the maximum deviation in E_C from the recorded value is ~ 0.01 eV (less than 1% of E_C), thus negligible. Setting the input cutoff energy at this value should allow for consistent results (baring the influence of other parameters), while also keeping computations efficient. The cutoff energy E_{cut} will be set to 600 eV for future calculations. Even though there might still be a margin of error on cohesive energy results, the additional adjustment of the k-points input will further optimize the energies and minimize errors.

4.2.3   k-points

The k-points input has various options available, from giving a specific selection of every k-point to simply setting the parameters for the creation of a Monkhorst-Pack grid[5]. Due to working with a two-dimensional monolayer, and with no need for band structure details when determining initial binding energy, a two-dimensional Monkhorst-Pack grid was considered to generate the k-points. The convergence test for increasing grid sizes was performed and the corresponding cohesive energies were obtained.

In figure 4.3b, along the x-axis we have the number of k-points in each direction of the 2D Monkhorst-Pack grid, starting from a $2 \times 2 \times 1$ grid and ending with a $10 \times 10 \times 1$ grid. Along the y-axis, the obtained cohesive energies E_C are plotted and compared for both SnS$_2$ unit cells at all optimization levels. E_C begins to plateau between a k-point grid of size $3 \times 3 \times 1$ and $4 \times 4 \times 1$, and converges from the $5 \times 5 \times 1$ grid and beyond. Starting with 1T unit cell, E_C converges at 3.16 eV, while the 1H unit cell is converges at the considerably lower E_C of 2.31 eV. Both values were obtained from SCF calculations. After relaxation and performing a new set of SCF calculations, E_C for 1T has increased to 3.43 eV, and E_C for 1H has increased to 3.15 eV. After VC relaxation and performing another set of SCF calculations, figure 4.3b shows that cohesive energy for both unit cells has decreased slightly, by a margin of 0.05-0.08 eV. This is in agreement with the difference present for the E_{cut} convergence tests. The same conclusion can also be drawn regarding the requirement for structural optimization, rather than using unit cells without optimization. Again, the 1T-SnS$_2$ monolayer phase is energetically more stable, and favoured over 1H-SnS$_2$ for future calculations.

Similar to the results of the previous section, past the convergence threshold there are only negligible increases in E_C. The remaining calculations of this dissertation will have the k-point input set at a $5 \times 5 \times 1$ grid, although exceptions will be made for results that require a higher number of k-points. Such results would include any data that needs to look at the band structure and energy spectrum of the BZ. In those cases, a $10 \times 10 \times 1$ grid will be used, or specific k-paths through the BZ will be selected.
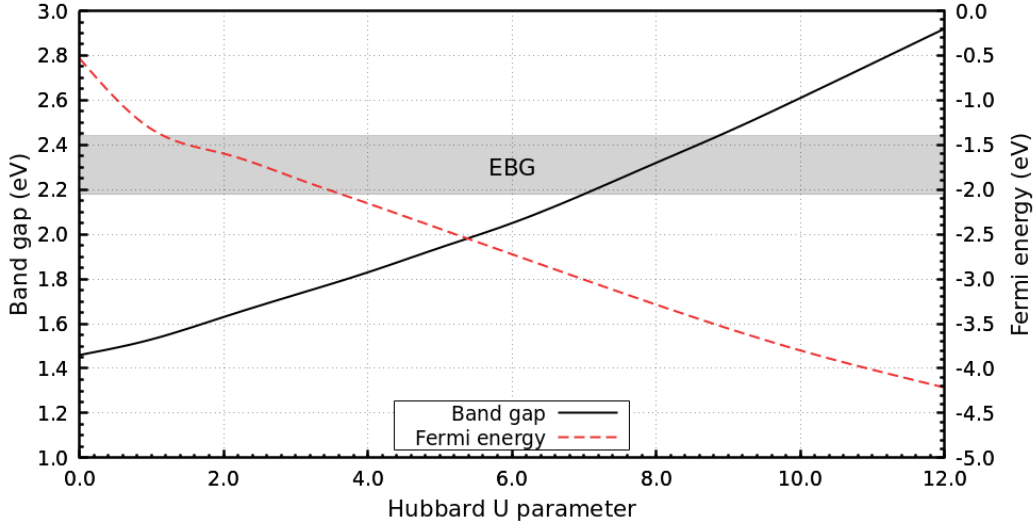
4.2.4 Hubbard U parameter

Figure 4.4: Change in band gap and Fermi energy E_F of 1T-SnS$_2$ as the Hubbard U parameter is adjusted. The shaded region labelled EBG shows the range of experimental measurements of the 1T-SnS$_2$ band gap.

At this point in the dissertation, we can confirm 1T-SnS$_2$ as our choice of phase, and look to improve the more strenuous U parameter input. The initially obtained DOS and band structure for 1T-SnS$_2$ displayed an inaccurate band gap E_g of 1.45 eV, roughly 40% below experimentally recorded values.[6–8] This is precisely the error meant for correction using Hubbard U, due to the presence of larger atoms within the lattice with high energy electron orbitals.

Determining the correct Hubbard U parameter requires its manual adjustment as an input in QE, until the measured E_g value falls within the range of measured experimental values. Hubbard U values need to be adjusted for each atom type within the unit cell individually. Having made initial measurements of the effect of the U parameter for both atom types (S and Sn), it was determined that the U parameter for Sn has a overall negligible or even detrimental effect on the E_g and Fermi energy E_F of the substrate. Instead, only the U parameter for S is adjusted, with the x-range in figure 4.4 spanning from 0 to 12. The shaded EBG region displays the possible values of E_g for 1T-SnS$_2$, ranging from 2.18 eV to 2.44 eV sourced from experimental results.[6–8] Lying almost exactly in the middle of the EBG range, a Hubbard U value of 8.0 proves to be the correct choice for obtaining a E_F and E_g accurate to experimental measurements. A correct E_g of $\sim$ 2.3 eV is measured for the substrate, along with E_F of -3.3 eV.

In summary, following a series of convergence tests, the optimal values were determined for multiple input parameters. The 1T-SnS$_2$ monolayer is selected for its greater energetic stability. Following structural optimization, the equilibrium lattice constant a_0 is determined to be 3.71 Å, while lattice constant c is set at 15.0 Å to minimize interlayer interactions. A cutoff energy E_{cut} of 600 eV was found to be sufficient obtaining a convergent cohesive energy. A Monkhorst-Pack grid of size $5 \times 5 \times 1$ is suitable for generating adequate k-points for Brillouin sampling, unless stating otherwise as determined by calculation requirements. Lastly, a Hubbard U parameter of 8.0 is set to be applied to 3p orbitals of the S atoms, correcting E_g measurements for all relevant results.

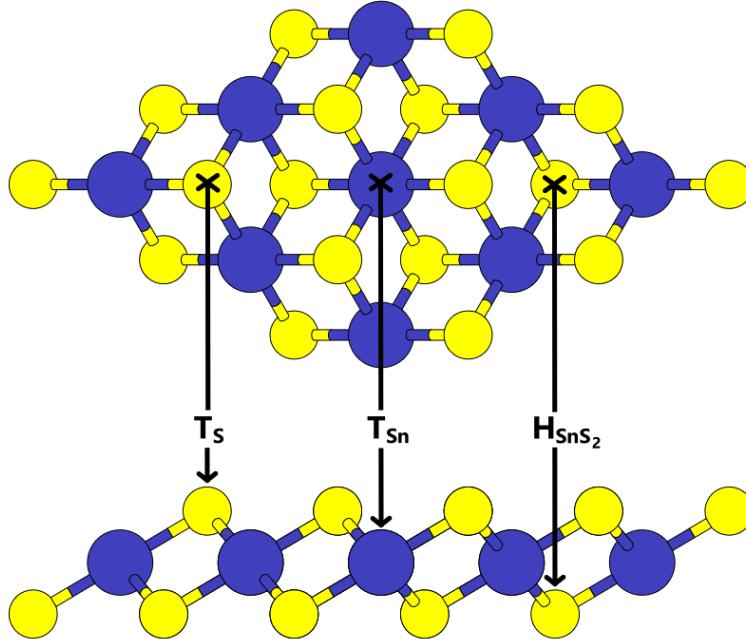## 4.3 SnS$_2$ monolayer surface mobility and activation barriers

Figure 4.5: The top and side view of the 1T-SnS$_2$ monolayer with binding sites labelled.

Consider the electronegativity of S (2.5) and Sn (1.8). Locations with higher concentrations of more negatively charged S atoms on the SnS$_2$ substrate will be more attractive for the binding of positively charged ions Li$^+$ or Na$^+$, and can in turn be labelled as seen in figure 4.5. Surface binding sites at top layer S atoms or at Sn atoms, as they are located on the 1T-phase substrate, are called the T$_S$ or T$_{Sn}$ sites, respectively. The T$_S$ sites specifically are restricted to S atoms of the upper S layer, as an additional binding site, called H$_{SnS_2}$, is located at all the bottom layer S atoms. These are the most likely locations for adatom binding, T$_S$ for being right next to an S atom, and T$_{Sn}$ and H$_{SnS_2}$ for occupying the centre of a triangle of top layer S atoms. A supercell test of convergence was performed for SnS$_2$, for the sizes 2×2, 3×3, 4×4, 5×5 and 6×6 each containing one Li adatom. The Li binding energy differences for these supercells are 0.199 eV (2×2 and 3×3), 0.018 eV (3×3 and 4×4), 0.013 (4×4 and 5×5) and 0.010 (5×5 and 6×6). Although the test results start to converge at 3×3, the larger 5×5 supercell has been adopted for all configurations studied. The 1T-SnS$_2$ monolayer has been placed into a 5×5 supercell, with this size in particular being chosen to allow us have both regions of strong interaction with a surface defect, as well as regions of negligible interaction, within the same supercell. We examine how the SnS$_2$ surface interacts with the adsorption of Li and Na atoms, as well as the addition of vacancy defects. Two types of vacancies are introduced, either an S vacancy (forming a V$_S$ site) or an Sn vacancy (forming a V$_{Sn}$ site).

To start, the mobility and diffusion of Li-/Na-ions across the SnS$_2$ monolayer substrate are examined. By the nature of the surface charge differences, there will be regions of higher and lower energy, acting as diffusion barriers, as we move between the fixed locations of the binding sites. These locations are

considered fixed, because they are the results of relaxation calculations performed for the Li-/Na-ion at that site, with atomic position optimization obtaining a more precise total energy. Additionally, these ions have not deviated considerably from the location of the binding site following relaxation, allowing the location to be considered a valid binding site. We investigate the results of NEB calculations, which have obtained saddle points and minimum energy paths between fixed locations as displayed in figures 4.6, 4.8, and 4.10.

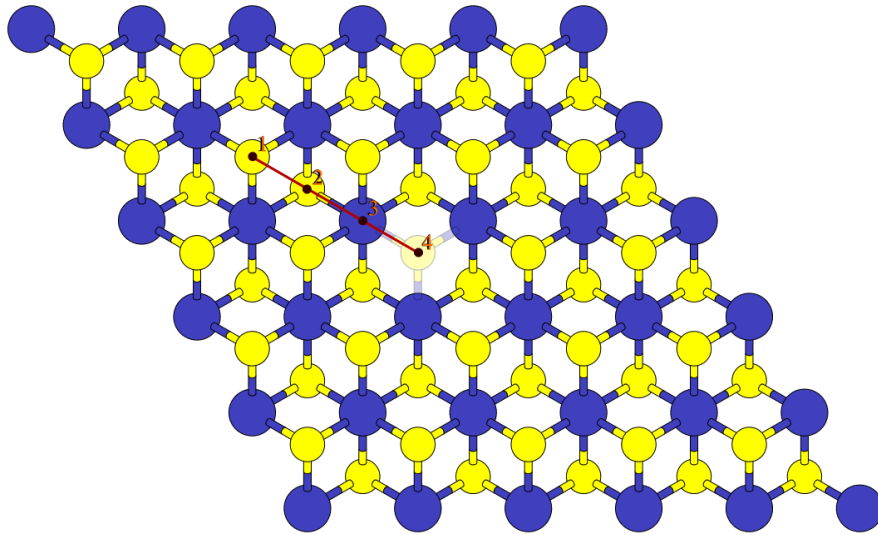### 4.3.1 Li/Na diffusion across the pristine SnS_2 monolayer

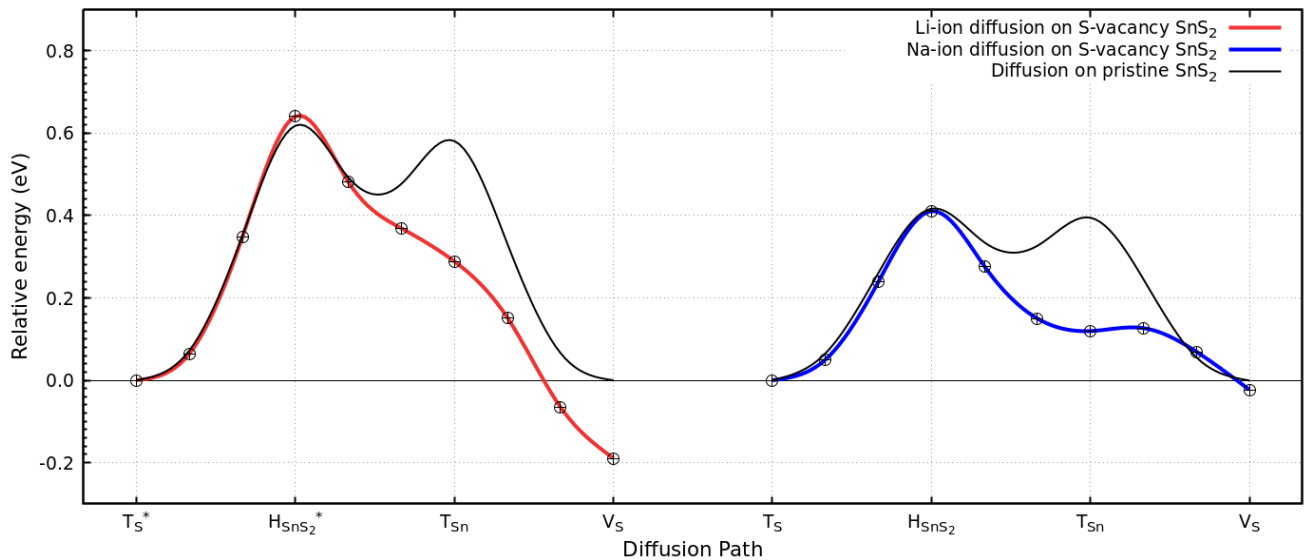Figure 4.6: Li/Na diffusion path across the pristine and S-vacancy SnS_2 monolayer.

Figure 4.7: Relative energy for diffusion across the pristine and S-vacancy SnS_2 surfaces, for (left) Li- and (right) Na-ions.

Figure 4.6 displays a top-down view of our 5×5 supercell of the 1T-SnS$_2$ monolayer, along with the S-vacancy location and a line for the diffusion path with fixed ion locations numbered. Our diffusion path, in this case for the pristine substrate, has four locations between which the minimum energy paths have been determined using NEB methods. These four fixed ion locations or binding sites along the diffusion path are:

$$(1)\ T_S \rightarrow (2)\ H_{SnS_2} \rightarrow (3)\ T_{Sn} \rightarrow (4)\ T_S,$$

with the last ion location of the path also being the location of the S-vacancy (V_S), to be considered in the next section.

Focusing on the pristine SnS$_2$ monolayer, we can see in figure 4.7 that the T_{Sn} and H_{SnS_2} sites visibly display the highest relative energy peaks. The overall diffusion barrier or activation energies recorded at the highest peaks are 0.61 eV for Li-ions and 0.42 eV for Na-ions, located at the H_{SnS_2} sites. The T_{Sn} relative energy is slightly lower. These results compare poorly to similar graphene-like materials. For an SnS monolayer, a diffusion barrier of 0.45 eV for Li-ions was obtained[9]. Additionally, studies have obtained diffusion barriers of 0.40 eV for Li-ions and 0.22 eV for Na-ions on borophene[10], 0.47 eV for Li-ions and 0.11 eV for Na-ions on MoS$_2$[11,12], and 0.13 eV for Na-ions on MoO$_2$[13].

The referenced diffusion barriers are all along the most efficient minimum energy paths across the surfaces, ignoring sites for which the difference in relative energy makes movement towards those locations prohibitive. Similarly, our own ion diffusion barriers will decrease significantly if more efficient paths across the SnS$_2$ monolayer are taken. Considering figure 4.7, an improved approach limits movement to paths along sites $\mathbf{H}_{SnS_2} \rightarrow \mathbf{T}_{Sn}$, for which the diffusion barriers are significantly decreased. This path more still allows for movement to all of the preferred H_{SnS_2} binding sites on the SnS$_2$ monolayer while ignoring the weaker T_S binding sites. The Li-ion diffusion barrier is now 0.19 eV, while the Na-ion diffusion barrier is 0.13 eV, which suggests exceptional atom mobility along the more efficient diffusion paths.

4.3.2   Li/Na diffusion across the S-vacancy SnS$_2$ monolayer

The diffusion path detailed in figure 4.6 is also of relevance for the S-vacancy SnS$_2$ monolayer. This path for the S-vacancy substrate has the same four locations between with minimum energy paths determined using NEB methods. The four fixed ion locations along the diffusion path are:

$$(1)\ T_S \rightarrow (2)\ H_{SnS_2} \rightarrow (3)\ T_{Sn} \rightarrow (4)\ V_S,$$

with the last location being the S-vacancy, having replaced the previous T_S site which existed on top of the S atom.

As shown in figure 4.7, the inclusion of an S-vacancy increases the overall difference in relative energy. For diffusion between the peak at the H_{SnS_2} site and the minimum at the vacancy binding site V_S, the overall diffusion barrier is now 0.83 eV for Li-ions (33% increase) and 0.43 eV for Na-ions ($\sim$2% increase). The relative energy of the T_{Sn} site neighbouring V_S has decreased significantly. It is apparent that creating an S-vacancy in the SnS$_2$ monolayer causes a higher diffusion barrier. The V_S site itself has a lower relative energy than the T_S site previously positioned at its location. Thus, within the vicinity of the S-vacancy, there is a loss of ion mobility, incentivising ion motion away from the vacancy location and its neighbours.

An additional effect is the loss of relative energy at the neighbouring sites of V_S. For Li, figure 4.7

shows that the relative energy at the T_{Sn} site has dropped by half, but more importantly, this site is not a stable extreme anymore. Li-ions cannot bind stably to T_{Sn} sites in the vicinity of the S-vacancy, and will instead move directly away from the S-vacancy towards H_{SnS_2} sites. This effect will carry over to other sites surrounding the S-vacancy. Li-ions resting at neighbouring H_{SnS_2} sites will move directly away from V_S towards T_{Sn} sites.

Na-ions have displayed better binding site stability in the presence of V_S, as well as smaller diffusion barriers recorded both for the pristine and the S-vacancy surface. This suggests that the 1T-SnS$_2$ monolayer is better suited to acting as an anode material for NIBs rather than LIBs. This is especially apparent for the case in which the monolayer has undergone defect engineering.
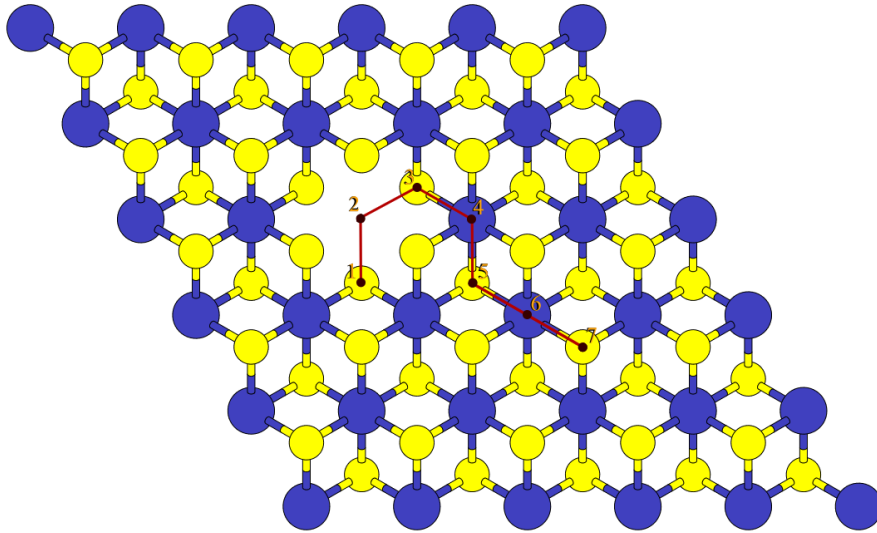
4.3.3 Li/Na diffusion across the Sn-vacancy SnS$_2$ monolayer

Figure 4.8: Diffusion path for Li-ions across the Sn-vacancy SnS$_2$ monolayer.

The configuration of the 1T-SnS$_2$ monolayer displayed in figure 4.8 has an Sn-vacancy instead of an S-vacancy. Figure 4.8 also shows a numbered line along which fixed Li-ion binding sites of the diffusion path are located. A much longer diffusion path was required to analyze diffusion barriers, due to Li-ions being unable to bind to T_S sites within the vicinity of the Sn-vacancy. In this case, for the Sn-vacancy substrate and Li-ion diffusion, we have seven locations between which the minimum energy paths have been determined using NEB methods. The seven fixed Li-ion binding sites along the diffusion path are:

$$(1)\ H_{SnS_2} \rightarrow (2)\ V_{Sn} \rightarrow (3)\ H_{SnS_2} \rightarrow (4)\ T_{Sn} \rightarrow (5)\ H_{SnS_2} \rightarrow (6)\ T_{Sn} \rightarrow (7)\ T_S,$$

with the second Li-ion binding site along the path being the Sn-vacancy location.

Figure 4.9 shows the change in relative energy for a Li-ion moving along the diffusion path of figure 4.8. In contrast to how the S-vacancy alters the relative energy of the SnS$_2$ monolayer, the Sn-vacancy causes a significant increase in relative energy at and around the vacancy site V_{Sn}. The relative energy is a rough measure of the attraction felt by a positively charged ion. Thus, in the absence of an Sn atom
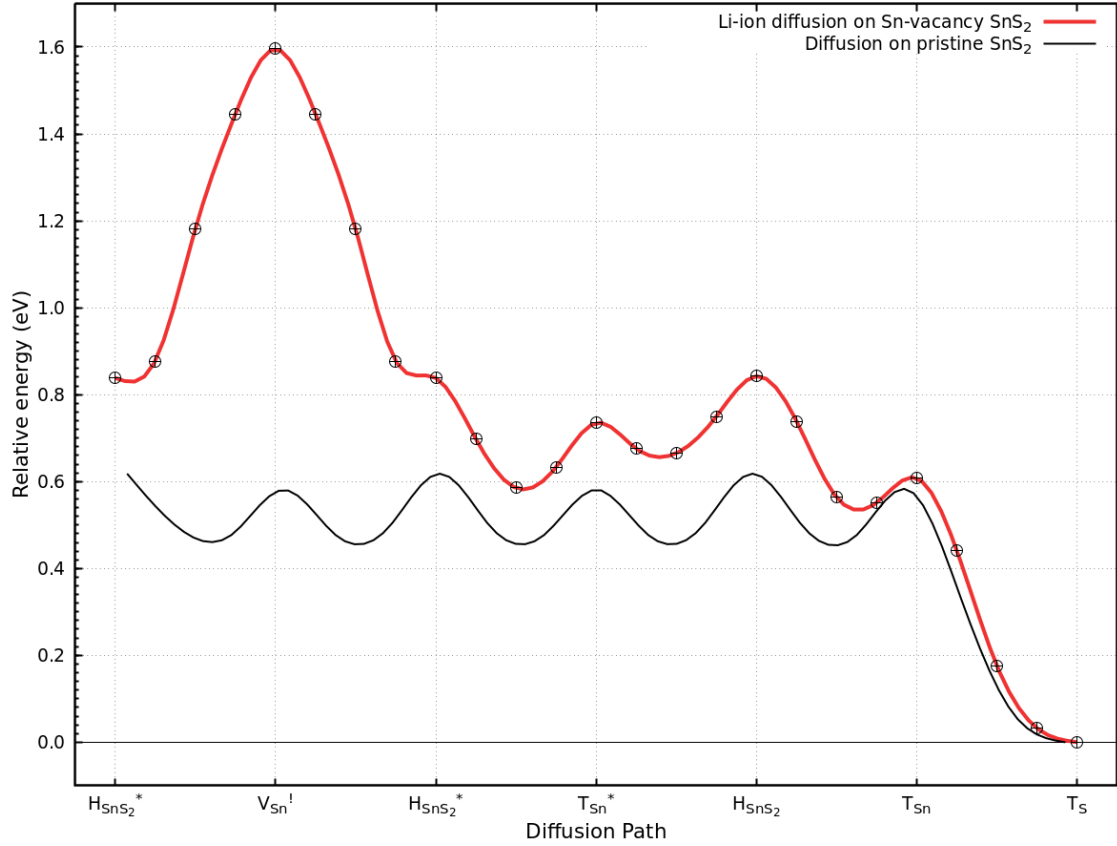
Figure 4.9: Relative energy for diffusion of Li-ions across the Sn-vacancy SnS_2 monolayer.

there is now a higher concentration of negatively charged S atoms present within the vicinity of V_{Sn}.

A note needs to be made regarding peculiarities of the Sn-vacancy SnS_2 surface, especially with regards to smaller Li-ions. The Sn-vacancy represents positively charged ions with the opportunity to bind into the substrate at the atomic position previously occupied by Sn, in effect creating a substitution defect. Li-ions are especially prone to such behaviour due to their smaller atomic radii. Whereas larger ions would be capable of occupying a location on top of the surface at the V_{Sn} site, Li-ions cannot, and will instead be substituted into the substrate. Figure 4.9 shows that, in addition to the substitution having nearly three times the relative energy of the comparable pristine site T_{Sn}, the relative energy is twice that of nearby H_{SnS_2} and T_{Sn} sites. This tremendous diffusion barrier, measured at 1.58 eV for Li-ions, significantly hampers ion mobility on the SnS_2 surface. Additionally, Li-ions are still unable to stably bind to half of the sites (all nearby T_S sites) surrounding the Sn-vacancy.

Figure 4.10 displays the same Sn-vacancy 1T-SnS_2 configuration as in figure 4.8, though in this case we have a different line for the diffusion path, now numbering fixed Na-ion locations. This Na-ion diffusion path is shorter in length than the Li-ion path, due to Na-ions still being capable of binding to the sites. Li-ions could not, following the Sn-vacancy addition. In this case, for the Sn-vacancy substrate and Na-ion diffusion, we have six locations between which the minimum energy paths have been determined using NEB methods. The six fixed Na-ion binding sites along the diffusion path are:

$$(1) \ T_S \rightarrow (2) \ V_{Sn} \rightarrow (3) \ T_S \rightarrow (4) \ H_{SnS_2} \rightarrow (5) \ T_{Sn} \rightarrow (6) \ T_S,$$
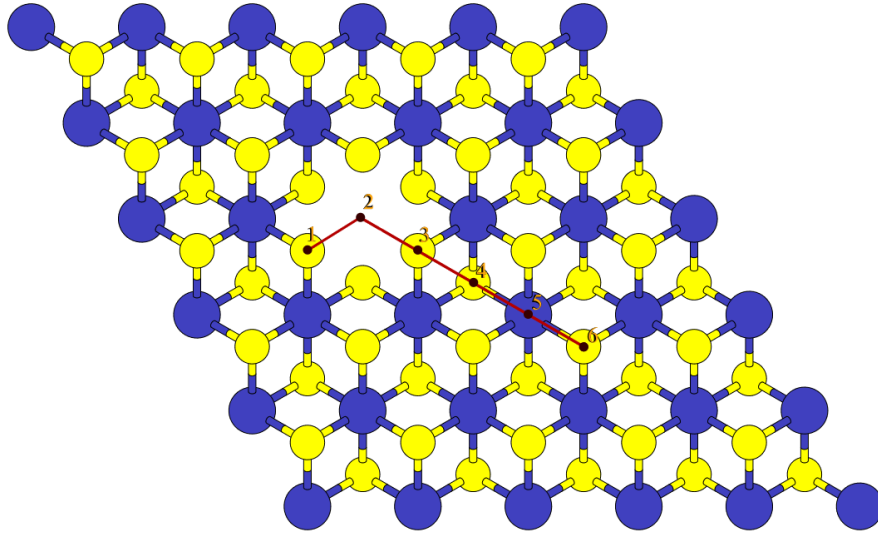
Figure 4.10: Diffusion path for Na-ions across the Sn-vacancy SnS$_2$ surface.
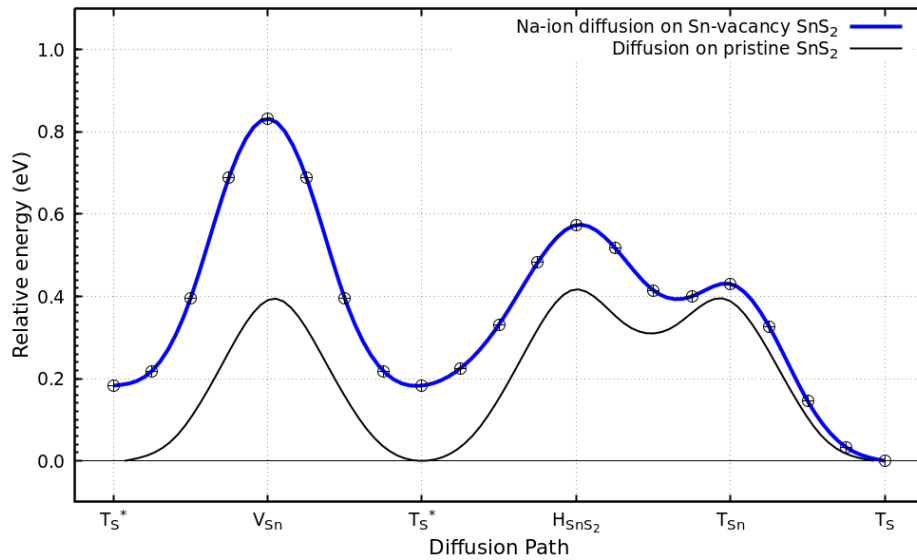

Figure 4.11: Relative energy for diffusion of Na-ions across the Sn-vacancy SnS$_2$ surface.

with the second Na-ion binding site along the path being where the Sn-vacancy is located.

Figure 4.11 shows the change in relative energy for a Na-ion moving along the diffusion path of figure 4.10. We have previously seen with the S-vacancy surface that Na-ions unlike Li-ions, are entirely capable of binding to T$_S$ sites within the vicinity of the vacancy. This remains true for the Sn-vacancy, even with V$_{Sn}$ acting to increase the relative energy of all surrounding sites, rather than decreasing the surrounding relative energy as the V$_S$ site did. The larger Na-ions is not as effected by the substitution problem present for Li-ions, and a stable V$_{Sn}$ site exists on top of the SnS$_2$ monolayer. Na-ions are still capable of being substituted into the surface. The Na diffusion barrier when moving from the surface level V$_{Sn}$ site into the substrate is 0.17 eV. The Na diffusion barrier when moving from V$_{Sn}$ to any neighbouring H$_{SnS_2}$ site is larger than this at roughly 0.22 eV. Na-ions still suffer the substitution problem, though the smaller

diffusion barriers allows Na to more easily escape the potential well of the Sn-vacancy.

In summary, we see that the Sn-vacancy, similar to the S-vacancy, creates a region highly favourable to the binding of Li/Na. Unfortunately, this region has a much higher relative energy than its neighbours, and in turn large diffusion barriers. Due to these properties, the V_{Sn} site acts as an atom trap, and impedes atom mobility, simultaneously impeding the charge and discharge cycles utilized by LIBs. The effect is not as pronounced for larger atoms, thus Sn-vacancies are still fairly useful for NIBs. However, consider the S-vacancy site V_S, which is not favoured for Li/na binding, but still increases neighbouring relative energy. V_S does not act as an atom trap, and though it can still impede atom mobility, but not to the same degree as the V_{Sn}. When considering the vacancy defect engineering to improve 1T-SnS$_2$ monolayers, for application as an anode material, an S-vacancy offers similar binding energy advantages and less atom mobility drawbacks than an Sn-vacancy.

4.3.4 Charge density following Li/Na adsorption

(a) Li on pristine SnS$_2$ (b) Li on S-vacancy SnS$_2$ (c) Na on pristine SnS$_2$ (d) Na on S-vacancy SnS$_2$
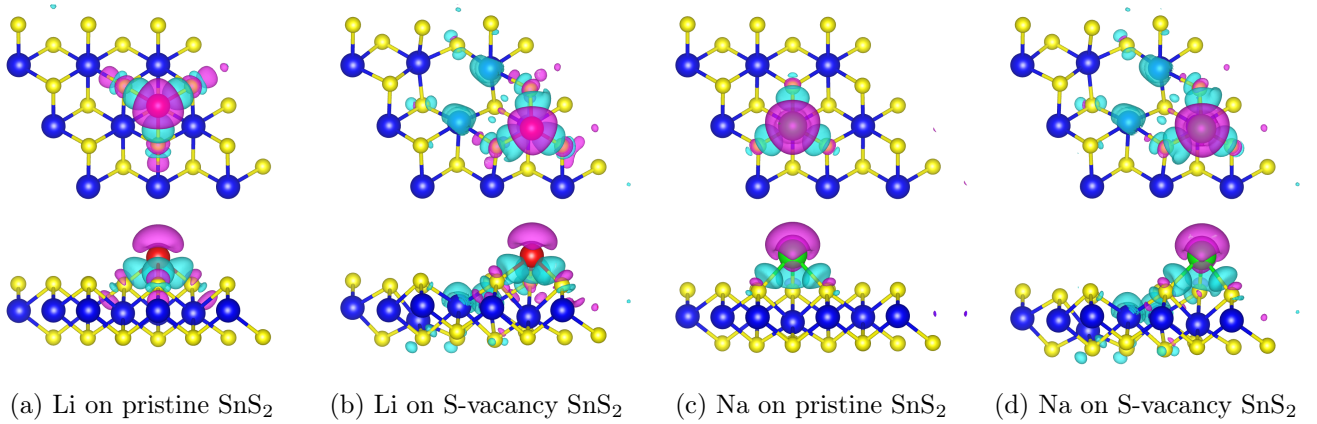
Figure 4.12: Top and side views of the charge density difference for Li/Na adatoms on SnS$_2$ monolayer, calculated considering an isovalue of 0.002 electrons/bohr^3. Cyan regions show where charge density has increased, while purple regions show where charge density has decreased.

The charge difference due to the inclusion of Li/Na adatoms and vacancies can be analysed by looking at a visualization of charge density differences. Charge density difference $\Delta\rho$ can be described by the following equation[14]:

$$\Delta\rho = \rho_T - \sum_i \rho_i. \tag{4.2}$$

The charge density difference $\Delta\rho$ is determined by obtaining the total charge density of the system ρ_T, and then subtracting all partial charge densities ρ_i. For the latter, a pseudo structure is constructed by dividing the overall structure into i sections, for which the charge density ρ_i is determined for each individual section i. Each section of the structure will still have the same lattice parameters and symmetry as the original structure. If we want to know the charge density difference following the adsorption of lithium or sodium, there will only be two sections, one containing the adatom, and one containing the SnS$_2$ monolayer.

Figure 4.12 presents the changes in electronic charge distribution surrounding the Li or Na adatom at various binding sites of the pristine as well as the S-vacancy SnS_2 monolayer. From the figures it is notable that changes in charge is concentrated nearby the adatoms, indicating that the Li or Na adatom greatly influences the uniform charge distribution of SnS_2 monolayer. Similarly, changes in the charge distribution are observed surrounding the S-vacancy. Near the adatoms, it was found that charge mainly depletes from the Li or Na adatoms towards S atoms. There is a large disturbance in charge distribution directly at the adatom (visible as a larger purple region), while portions of this charge is distributed towards each of the surrounding S atoms (forming three smaller cyan regions). This redistribution of charge carries on in straight lines away from the adatom site; on the side of the S atoms opposite the adatom site, there is smaller region of charge redistribution mirroring the charge transfer from the adatom towards the S atoms. On the opposite sides we instead have charge depleted from Sn atoms and moving towards the S atoms. For the pristine SnS_2 monolayer, the charge transfer is symmetrically shared between all three surrounding S atoms.

As for the charge distribution surrounding the S-vacancy, we can immediately see that the pristine charge transfer symmetry is disturbed. Near the S-vacancy, there is an increase in charge distribution mostly localized at Sn atoms. The two Sn atoms in closest proximity to the adatom site have and show a larger region of increased charge density, while the furthest Sn atom does not show any change in charge density. This increase is also visible for the S atoms neighbouring the adatom. The S atoms nearest the S-vacancy site have a larger increase in charge density.

4.4   Energetic stability of Li/Na on the SnS_2 monolayer

To gain insight into the energetic stability of the SnS_2 monolayer for Li- and Na-ion configurations, we calculated the binding energy E_b at the H_{SnS_2}, T_{Sn}, T_S, and V_S binding sites visible in figure 4.5. At each binding location, the Li- and Na-ions have been adsorbed onto the SnS_2 monolayer. Each monolayer configuration underwent additional atomic position optimization, from which the total energy is recorded. The total energy result is in turn used to calculate E_b, which represents the energy difference between the relaxed SnS_2 monolayer with the bonded Li-/Na-ion adatom, the isolated SnS_2 monolayer and the isolated Li-/Na-ion adatom. This energy difference is described by the following expression[13]:

$$E_b = - \left(\frac{E_{SnS_2+ad} - E_{SnS_2} - nE_{ad}}{n} \right),$$ (4.3)

with E_{SnS_2+ad} being the total energy of relaxed SnS_2 monolayer with the bonded Li/Na adatom, E_{SnS_2} is the total energy of the isolated SnS_2 monolayer, E_{ad} is the energy of an isolated Li/Na adatom, and n is the number of adatoms adsorbed on the monolayer substrate. For this dissertation, E_b for both Li- and Na-ion configurations at each of the most stable binding sites are indicated in table 4.1. The binding energy E_b, which can also be called the adsorption energy in many cases, describes the energy needed to form a bond between an adatom and the SnS_2 monolayer (and in turn the energy required to remove an adatom from the surface). Obtaining a positive value for E_b reveals that an adatom is attracted to the substrate surface. For the SnS_2 monolayer, the Li-/Na-ions will form a uniform adatom dispersion. Negative E_b values would instead have an introduced Li/Na adatom agglomeration forming an undesired bulk of metallic material above the substrate.

Table 4.1: The calculated Li/Na binding energy E_b and bond length $d_{Li/Na-SnS_2}$ for various adatom configurations on the SnS_2 monolayer.

Site	E_b for Li (eV)	d_{Li-SnS_2} (Å)	E_b for Na (eV)	d_{Na-SnS_2} (Å)
Pristine SnS$_2$ monolayer				
T_{Sn}	2.96 (2.68[15])	1.30	2.51 (1.34[16])	1.89
T_S	2.38	2.25	2.11	2.61
H_{SnS_2}	3.00 (2.72[15])	1.27	2.53 (1.36[16])	1.84
SnS$_2$ monolayer with S-vacancy				
V_S	2.25	0.67	2.16	1.04
T_{Sn}^*	3.26	1.30	2.93	1.60
T_S^*	2.44	2.26	2.19	2.50
$H_{SnS_2}^*$	3.24	1.05	2.77	1.69
SnS$_2$ monolayer with Sn-vacancy				
V_{Sn}	5.01	−1.25	4.01	1.32
T_{Sn}^*	4.17	1.56	3.70	1.91
T_S^*	—	—	3.36	2.40
$H_{SnS_2}^*$	4.28	1.07	3.77	1.70

* Li/Na configurations directly neighbouring the vacancy site on the SnS$_2$ monolayer.

4.4.1 Energetic stability of Li/Na on the pristine SnS$_2$ monolayer

Comparing H_{SnS_2}, T_{Sn} and T_S sites on the pristine SnS$_2$ monolayer, table 4.1 shows that H_{SnS_2} is the most stable site with an E_b of 3.00 eV for Li and 2.53 eV for Na. Being only slightly less stable we have T_{Sn}, for which E_b is smaller by 0.04 eV for Li and 0.02 eV for Na. The small difference in binding energy suggests that a Li/Na dispersion can consist of both H_{SnS_2} and T_{Sn} sites, and co-exist under conditions of finite temperature. The similarity in binding energies can be attributed to 1st nearest neighbor S atoms in both sites, since the positively charged Li- and Na-ions are more strongly attracted to the negatively charged S atoms (see figures 4.13d and 4.13g). Of the investigated binding sites, T_S is the least stable for both Li and Na adatom configurations, with E_b being 0.62 eV smaller for Li and 0.42 eV smaller for Na. These differences are similar to the diffusion barriers observed in figure 4.7. Table 4.1 shows that our calculated E_b values for the H_{SnS_2} and T_{Sn} configurations are comparable to those reported by Lv et al.[15], calculated from the same exchange correlation functional (GGA-PBE). In comparison, the E_b results of Samad et al.[16] for Na on pristine SnS$_2$ monolayer configurations are smaller by almost half as compared to our values, while still using the same GGA-PBE functionals. Such an underestimation likely results from a smaller energy cutoff of 350 eV being used.

Measurements of relaxed Li/Na adatom bond lengths ($d_{Li/Na-SnS_2}$) measured vertically between the ions and the substrate surface are also listed in table 4.1. The most stable site H_{SnS_2} also has the shortest d_{Li-SnS_2}, recorded at 1.27 Å , while d_{Na-SnS_2} has a value of 1.84 Å. The least stable site T_S has a greater bond length for both alkali metal adsorptions, longer by almost 0.8 Å. This difference can be attributed entirely to the bond energies at these sites. Considering again the larger electronegativity of S atoms, you can see the higher number of 1st nearest neighbor S atoms (of which there are three, see figure 4.5) at
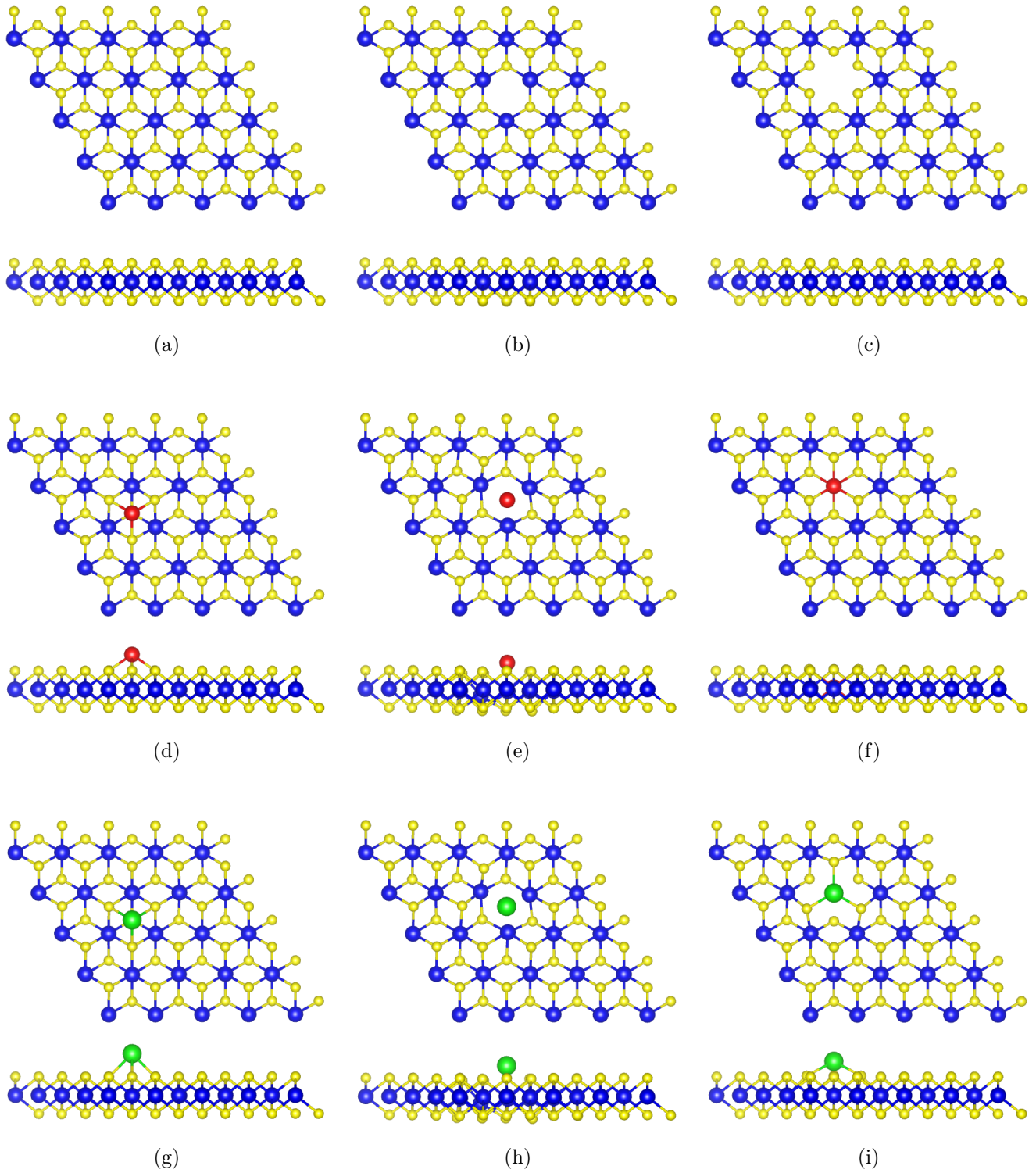
Figure 4.13: Relaxed structures of pristine, S-vacancy and Sn-vacancy SnS_2 monolayers, displaying the supercell (1st row) prior to adsorption and after the adsorption of (2nd row) Li- and (3rd row) Na-ions.

H_{SnS_2} sites are more likely to accept the Li/Na valence electron, in turn forming a strong ionic bonding with high E_b. The higher bond energy correlates directly with a shorter $d_{Li/Na-SnS_2}$. In comparison, T_S sites have three Sn atoms as the 1st nearest neighbors, which are much less likely to accept the Li/Na valence electron, thus offering a less favourable binding site.

4.4.2 Energetic stability of Li/Na on the S-vacancy SnS$_2$ monolayer

The E_b values of Li/Na configurations on S-vacancy V_S site and on its nearest neighbours (the T^*_{Sn}, T^*_S and $H^*_{SnS_2}$ sites) are also shown in table 4.1. There exists a notable increase in the E_b values for all stable sites T^*_{Sn}, T^*_S and $H^*_{SnS_2}$ within the vicinity of the V_S site. The most stable sites following the increase are still T^*_{Sn} and $H^*_{SnS_2}$. The increase in E_b for Li is approximately 0.25 eV for both binding sites, resulting in T^*_{Sn} and $H^*_{SnS_2}$ having very similar values for E_b. The increase in E_b for Na is much larger for the T^*_{Sn} site, with the result being 0.40 eV higher rather than the 0.25 eV difference recorded for the $H^*_{SnS_2}$ site. This is due to the T^*_{Sn} site not being the same one used for Li. Recall that the sites surrounding the S-vacancy are incapable of forming a stable bond with smaller Li atoms, a characteristic not shared with Na atoms. Figure 4.7 shows a local maximum appearing within the region of the T^*_{Sn} site, and this is the site at which the Na atom was positioned, with a significantly stronger bond energy. Otherwise, T_{Sn} sites further from the S-vacancy will have an increase in E_b similar to the increase measured for the $H^*_{SnS_2}$ site.

Regarding bond lengths d_{Li-SnS_2} and d_{Na-SnS_2}; for most of the previously mentioned sites, bond lengths have decreased as expected for increased E_b, with one exception. For the T^*_{Sn} site, d_{Li-SnS_2} has not changed significantly from the pristine d_{Li-SnS_2} at T_{Sn}. Examining the relaxed atomic positions, it can be determined that the Li adatom has still moved closer to the SnS$_2$ surface. The measurement remains the same because the SnS$_2$ surface, within the vicinity of the Li adatom, has moved closer as well, thus the actual bond length d_{Li-SnS_2} has decreased. Similar structural changes occur for all adatom configurations.

The V_S site is the least stable for both the Li and Na configurations, having only the less electronegative Sn atoms as 1st nearest neighbors, with the nearest S atoms being positioned on the opposite site of the substrate. This observation is confirmed by multiple studies, which study the factors capable of deciding Li/Na adatom preference regarding vacancies, such as vacancy density, and as seen, the surrounding electronegativity.[17–20] E_b at V_S itself has decreased by 0.13 eV for Li and has slightly increased by 0.05 eV for Na, when compared T_S which previously occupied the S-vacancy location. Bond lengths d_{Li-SnS_2} and d_{Na-SnS_2} have both decreased by 0.71 Å and 0.35 Å respectively, due to the S-vacancy forming a gap in the top layer of SnS$_2$ that an adatom can fill partially (see figures 4.13e and 4.13h). The difference in interactions between Li and Na can only be attributed to the difference in atomic size, as otherwise they are electronically similar. This observation points towards SnS$_2$ being a better anode material for NIBs. Regardless, the improvements in E_b surrounding V_S shows that Li/Na can be dispersed above the T^*_{Sn} and $H^*_{SnS_2}$ without forming a metallic cluster. The E_b results for pristine SnS$_2$ have already shown its suitability as an anode material for LIBs/NIBs, while the improvements displayed with the addition of an S-vacancy suggests the possibility of producing high performance LIBs/NIBs, pending investigation of storage capacity.

4.4.3 Energetic stability of Li/Na on the Sn-vacancy SnS$_2$ monolayer

Overall, table 4.1 shows that E$_b$ for Li and Na adatoms is increased within the vicinity of the Sn-vacancy. The increase is especially pronounced at the location of the vacancy, with adatoms tending towards substitution into the atomic position previously occupied by Sn. The Sn-vacancy SnS$_2$ configurations are displayed in the bottom rows of table 4.1, though it must be noted that no values are listed for T$_S^*$ in the case of Li adatoms. This is as result of no stable T$_S$ sites existing for the 1st nearest neighbour top layer S atoms, which is also true for the 2nd nearest neighbour top layer S atoms. There is also a peculiarity regarding d$_{Li-SnS_2}$ for V$_{Sn}$ (figure 4.13f). While it is possible for a Li adatom to bind at the location of the Sn-vacancy, it is a substitution into the substrate. Thus, d$_{Li-SnS_2}$, the distance between the Li adatom and the SnS$_2$ surface, has a negative result. Specifically, this substitution has an E$_b$ value of 5.01 eV and d$_{Li-SnS_2}$ of -1.25 Å. As for Na at V$_{Sn}$, this adatom remains capable of staying on top of the substrate (figure 4.13i), although the diffusion barrier of 0.18 eV for substitution can easily entrap the adatom. Regardless, E$_b$ at V$_{Sn}$ has a value of 4.01 eV, and remains higher than E$_b$ for all surrounding binding sites.

Next, considering the remaining binding sites, T$_S^*$ and H$_{SnS_2}^*$, both are increasing within the vicinity of the Sn-vacancy, being approximately 4.2 eV for Li and 3.7 eV for Na. For both adatoms, this is an increase of 1.2 eV in comparison with the pristine SnS$_2$ monolayer. The increases are greater than within the vicinity of an S-vacancy, although the corresponding bond lengths are shorter than their S-vacancy equivalents. Once more, this is a likely result of structural changes within the vicinity of the Li and Na adatoms, suggesting that the presence of an Sn-vacancy has decreased the structural integrity of the monolayer. That is to say, the monolayer is now more vulnerable to external interactions, which would force significant structural shifts, such as substrate expansion or bending. This factor is another indication of how an Sn-vacancy is not suitable for use as an anode material for LIBs/NIBs, along with the poor surface mobility and the likelihood of poor charge cycling as result of the mobility loss.

4.4.4 Energetic stability of multiple Li/Na on the SnS$_2$ monolayer

We have further examined the effect of multiple Li/Na atoms on the substrate stability, by calculating the E$_b$ with respect to the gradual increase of the number of adatoms. These results are presented in figure 4.14, with the Li/Na atoms all adsorbed on the most energetically stable sites available (H$_{SnS_2}$ and H$_{SnS_2}^*$), doubling in number for an increase from 1 to 16. The gentle curvature of the change in E$_b$, which seems to converge while remaining positive, possibly predicting that the SnS$_2$ monolayer is capable of storing a large agglomeration of Li or Na without ever clustering, even upon reaching the maximum theoretical specific capacity. A bump in the E$_b$ curve for S-vacancy SnS$_2$ is also observable, and results from the positioning of adatoms as the concentration increased. Adatoms were initially centered as close as possible to V$_S$, a region for which binding energy is especially greater than on pristine. Thus, for lower concentrations the binding energy was recorded to be significantly higher on the S-vacancy SnS$_2$ substrate. For higher concentrations, adatoms are spread more evenly. For a higher number of adatoms, the E$_b$ plots have similar curvature.

Figure 4.14 clearly shows that E$_b$ is decreasing as as the number of adatoms increases, for all considered configurations. This reduction in E$_b$ could be attributed to repulsive electrostatic forces experienced
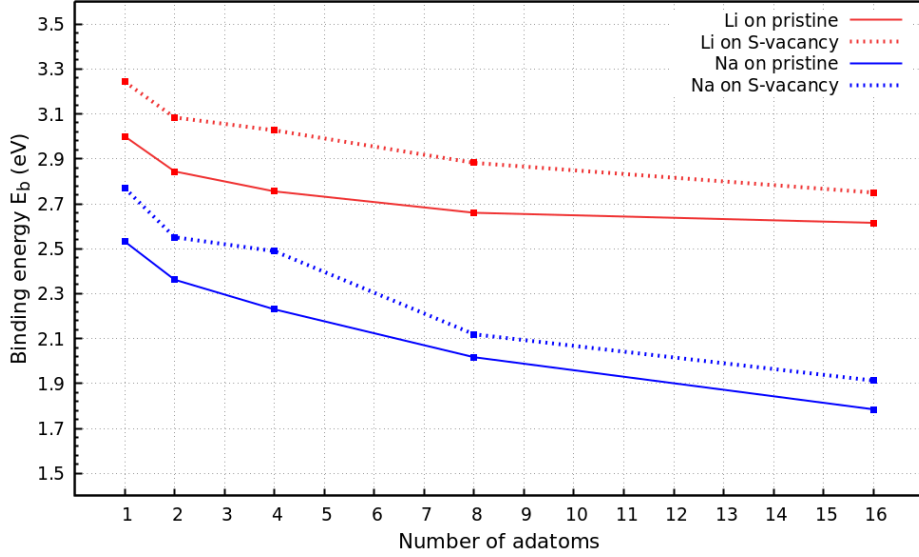
Figure 4.14: Binding energy E_b with respect to the number of Li and Na adatoms on the S-vacancy SnS_2 surface.

between the similarly charged Li/Na atoms increasing in magnitude as the Li/Na surface concentration increases. For the pristine SnS_2 monolayer, with all binding sites being at H_{SnS_2}, E_b has decreased to 2.62 eV for 16 Li adatoms and to 1.79 eV for 16 Na adatoms. For the S-vacancy SnS_2 monolayer and approximately the same binding sites (due to V_S preventing bonds in its vicinity), E_b has decreased to 2.75 eV for 16 Li adatoms and to 1.91 eV for 16 Na adatoms. At this adatom concentration, the binding energies are still far greater than 0.00 eV, suggesting a far greater concentration of adatoms can be accommodated before they would begin to form metallic Li/Na in bulk on top of the substrate surface. The decrease in E_b is an expected result of an increased number of adatoms, similar to results from comparable studies on graphene-like materials; as is the case for TMDs such as MoO_2 and ReS_2,[13,18] as well as MXenes such as Mo_2C.[17]
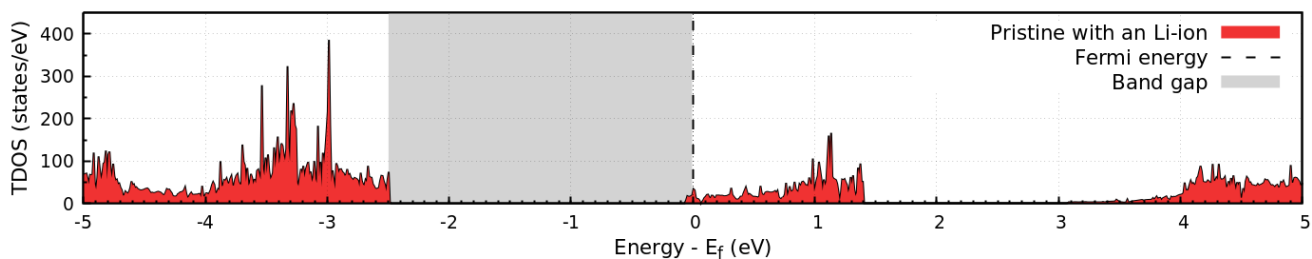
4.5 Density of states

To investigate the electronic conductivity of the 1T-SnS_2 monolayer, for Li and Na adatoms, the total density of states (TDOS) were plotted. This is an attempt to understand the electrochemical performance of the substrate as an anode material. The TDOS was obtained following relaxation computations, with the Hubbard U parameter for Fermi energy and band gap corrections, along with a $10 \times 10 \times 1$ Monkhorst-Pack grid for k-point generation. The obtained TDOS was then plotted in figures 4.15 and 4.16 for the pristine and S-vacancy SnS_2 monolayers, also looking at the addition of both 1 and 16 adatoms for both Li and Na. Lastly, we also plot TDOS for the Sn-vacancy SnS_2 monolayer and thereafter, examine how it reacts to both Li and Na adatoms. By now, we have already concluded that the Sn-vacancy is unsuitable for use as an anode material. The included TDOS plots of figure 4.17 shows how the Sn-vacancy effects the substrate surface, which is then easily contrasted with the TDOS of the pristine and S-vacancy substrates.
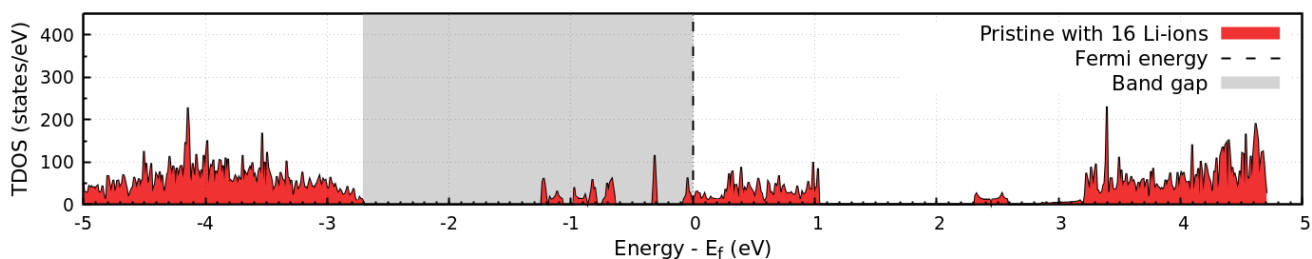
It should be noted that we have plotted along the x-axis $Energy - E_F$, which will place the Fermi energy E_F at 0 eV for all plots. However, E_F is not consistent between the plots at all, and generally
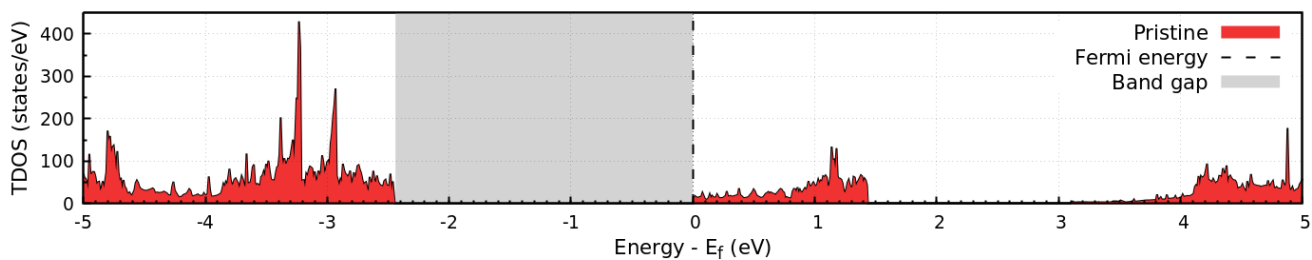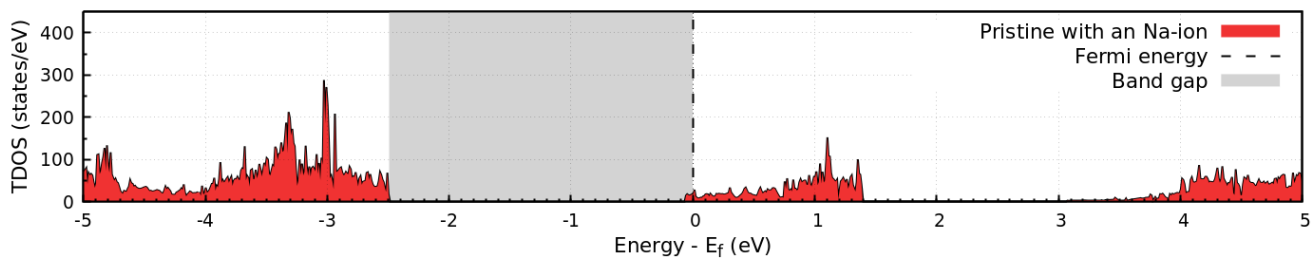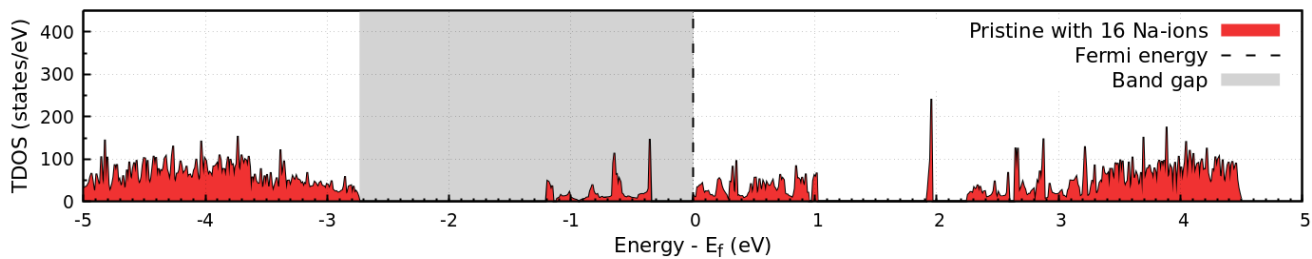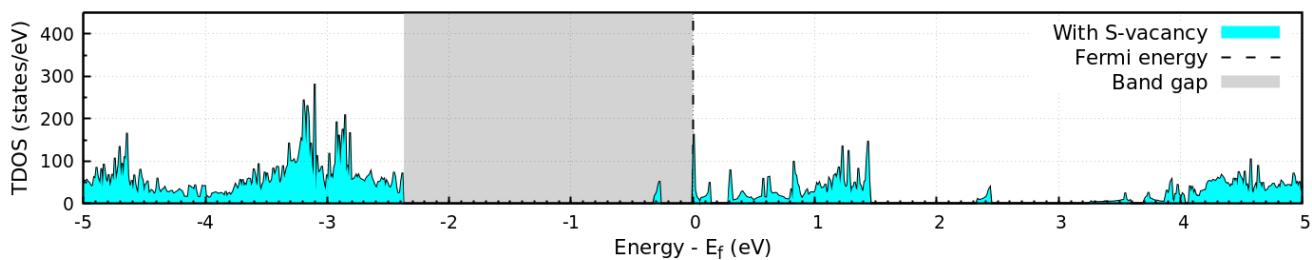
(a) No ions.

(b) 1 Li-ion.

(c) 16 Li-ions.

(d) 1 Na-ion.

(e) 16 Na-ions.

Figure 4.15: Total density of states for the pristine SnS_2 monolayer with adsorbed Li- and Na-ions.

(a) No ions.

(b) 1 Li-ion.

(c) 16 Li-ions.

(d) 1 Na-ion.

(e) 16 Na-ions.

Figure 4.16: Total density of states for the S-vacancy SnS_2 monolayer with adsorbed Li- and Na-ions.
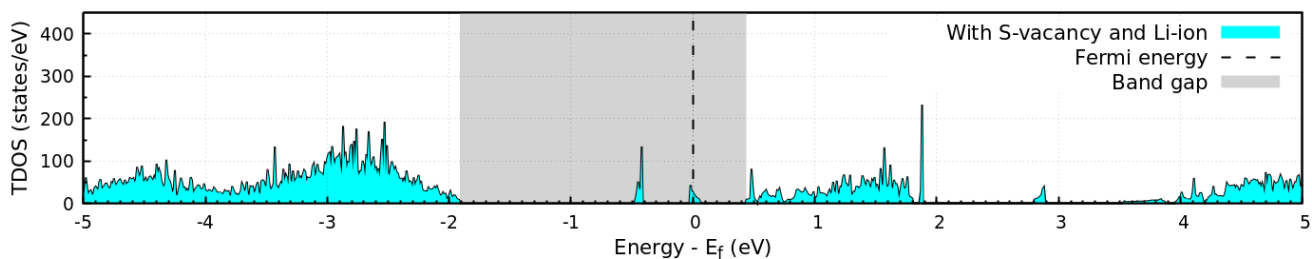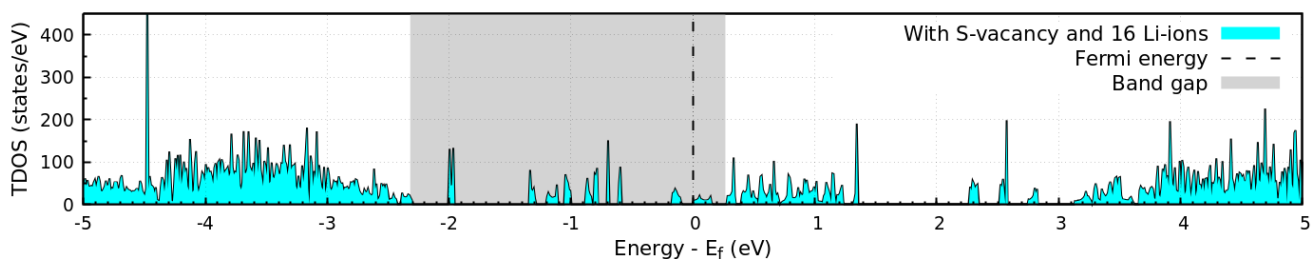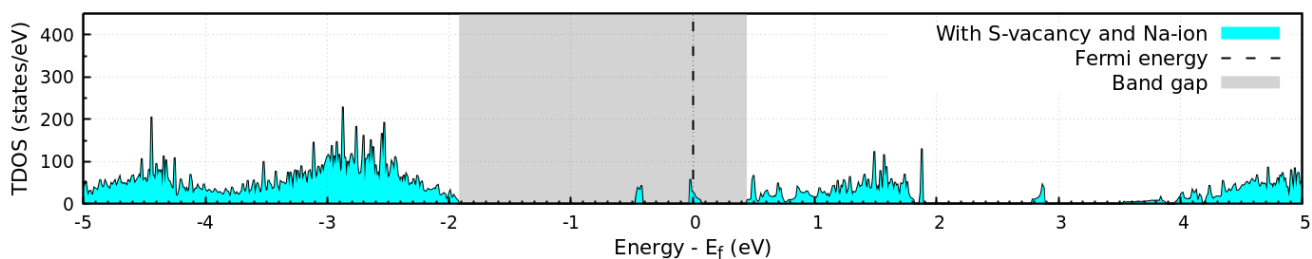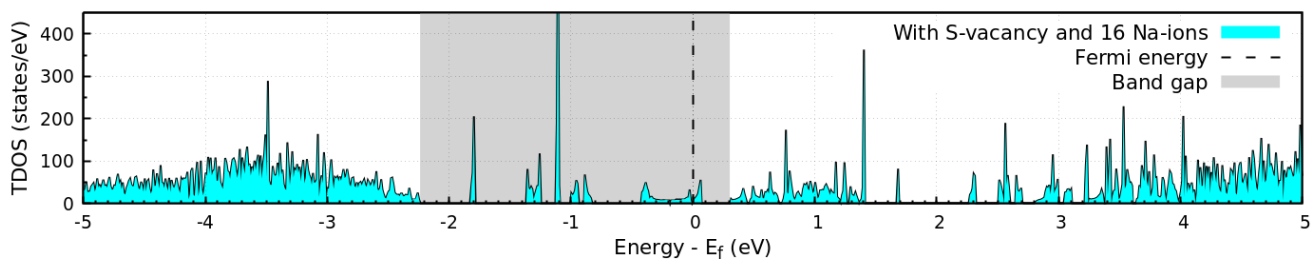
(a) No ions.
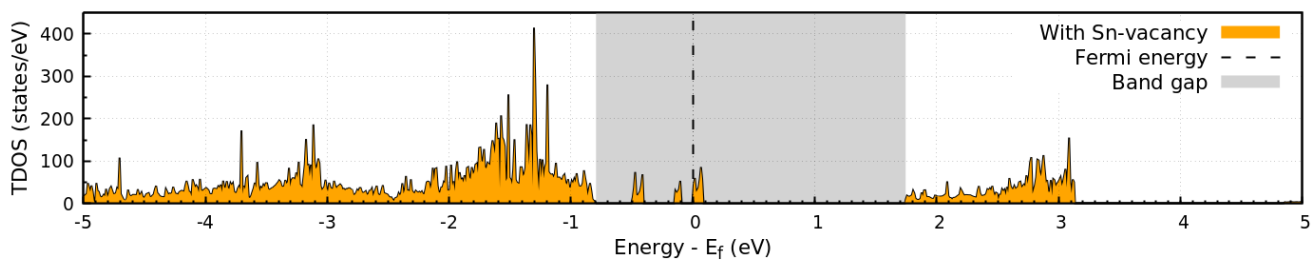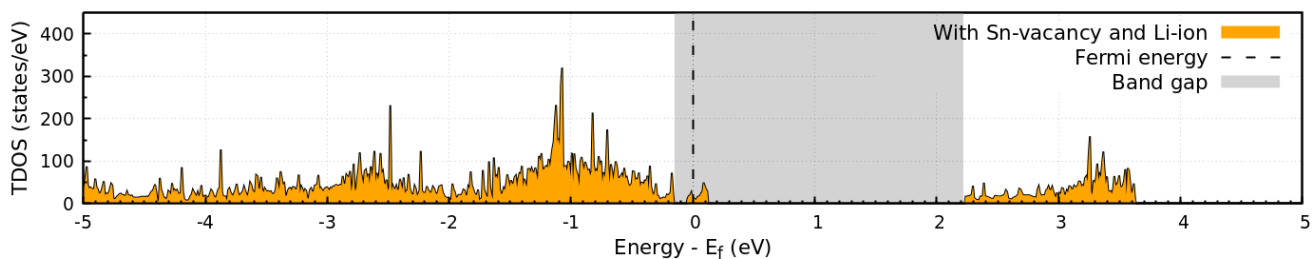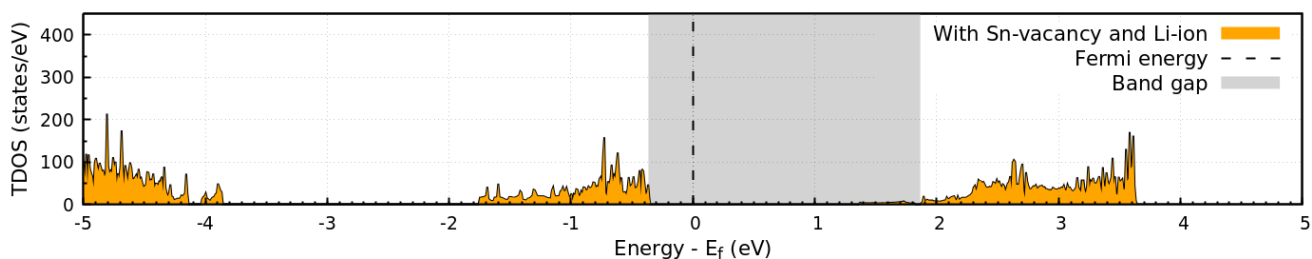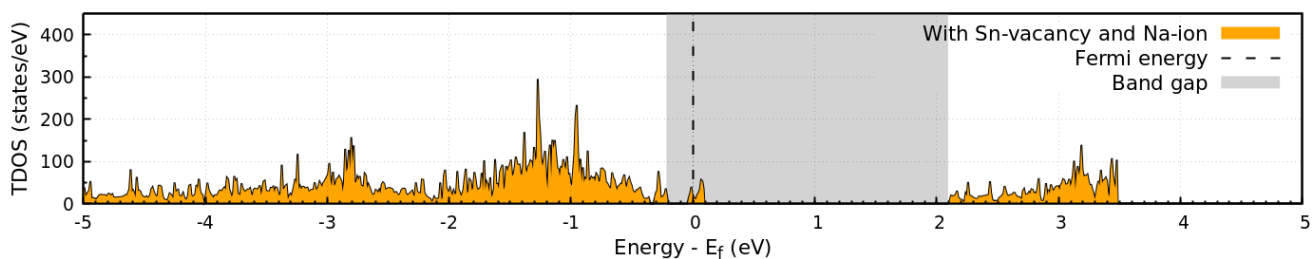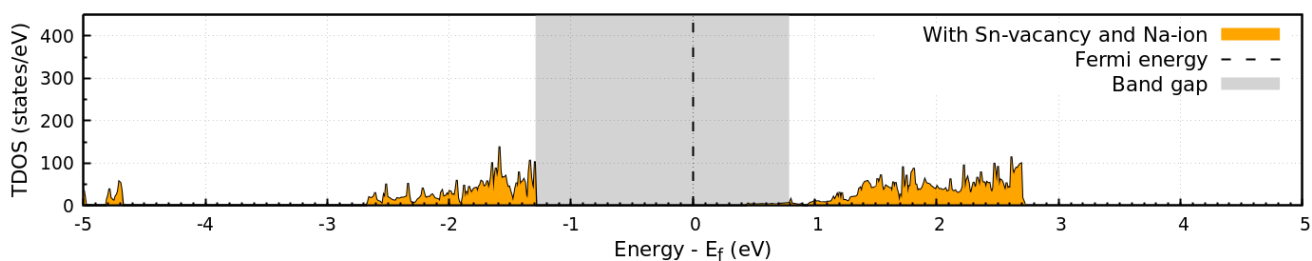
(b) 1 Li-ion.

(c) 16 Li-ions.

(d) 1 Na-ion.

(e) 16 Na-ions.

Figure 4.17: Total density of states for the Sn-vacancy SnS$_2$ monolayer with adsorbed Li- and Na-ions.

will increase with the addition of adatoms, while decreasing when a vacancy defect (the loss of atoms)

is introduced onto the substrate. Recall that the E_F indicates the highest energy achievable by valence electrons at 0 K. In turn, E_F allows us to differentiate between the valence and conduction bands of the energy structure of a material. The states immediately after E_F represent the conduction band, and the states immediately prior to E_F represents the valence band. There is some difficulty in identifying these band in more complex structures of multiple elements, as is the case of our SnS_2 monolayer with Li and Na adsorption atoms and vacancy defects. In these cases, a change in E_F is a good indicator of a change in the electronic properties of the material.

4.5.1 DOS of Li/Na on pristine SnS_2

The pristine SnS_2 monolayer (in figure 4.15a) is an insulator with E_g of 2.44 eV between valence band maximum (VBM) and conduction band minimum (CBM), indicative of a somewhat poorer electronic conductivity. The valence band shows pronounced peaks fairly close to the VBM, while the conduction band is flatter next to CBM, with the peaks occurring nearer to maximum of the conduction band. To start, we have E_F of -2.19 eV. With E_F being next to CBM, the SnS_2 monolayer shows characteristics of an *n*-type semiconductor material.

With the addition of 1 Li-ion, the E_g increases in width slightly to about 2.50 eV, while at the same time the conduction band begins to encroach upon the band gap. This is visible in figure 4.15b where the E_F is positioned just past CBM, with an increased value of -2.03 eV. At this low Li concentration, the DOS has approximately the same peaks. Increasing the Li concentration up to 16 Li-ions, the band gap has widened even further, measurable as roughly 2.70 eV. The encroachment of the conduction band into the band gap has increased considerably, introducing a new band of states onto E_g while E_F is now -0.33 eV. This is indicative of an increased electron presence that can be attributed to the higher Li-ion concentration, and is characteristic of metallic materials. With this additional band, the largest band gap within the vicinity of E_F is measured at 1.45 eV, a good indicator of the increased conductivity of the material as lithiation has increased. Additionally, states within the valence band are distributed more evenly, peaking at a far lower energy. The conduction band is similarly affected, while lacking the more pronounced peaks present for pristine SnS_2.

With the addition of 1 Na-ion, the E_g increases in width slightly to about 2.49 eV, while at the same time the conduction band begins to encroach upon the band gap. This is visible due to E_F being positioned within the conduction band at -1.94 eV. At this low Na concentration, the density of states has approximately the same peaks, though flattened and smoothed across a wider range of energies. Increasing the Na concentration up to 16 Na-ions, the E_g has increased even further, measurable as roughly 2.73 eV. The encroachment of the conduction band into the band gap has increased considerably, creating much wider conduction band with E_F positioned in it at 0.90 eV. This is indicative of an increased electron presence that can be attributed to the higher Na-ion concentration, and the material obtains metallic characteristics. This additional band decreases the effective E_g to 1.53 eV. Thus increased sodiation is shown to cause increased conductivity of the material, the same as caused by increased lithiation. Again, the valence band states are more evenly distributed, although now they also have no more pronounced peaks at all.

Overall, the addition of one Li or Na adatom on H_{SnS_2} causes a Fermi level shift towards the CBM which is in agreement with the existing studies,[13,18,21] and reveals the possibility of electronic charges

transferred into the system and increased conductivity. For an increased adatom concentration, still focused at H_{SnS_2} sites (figures 4.15c and 4.15e), the Fermi level shifts further into the CBM and more occupied states appear within the band gap E_g, and the material acts as a metal with high conductivity.

4.5.2 DOS of Li/Na on S-vacancy SnS$_2$

The S-vacancy SnS$_2$ monolayer (TDOS in figure 4.16a) has undergone a change in its electronic structure. It has a decreased E_g of 2.37 eV following the loss of an S atom, as well as an additional band in the band gap close to VBM. There is also a gap appearing in the valence band, although overall the valence band has a greater density of states, with higher peaks at irregular energy intervals. At this point E_F has decreased slightly to -2.29 eV. It remains next to CBM, and the S-vacancy SnS$_2$ monolayer is still an n-type semiconductor.

With the addition of 1 Li-ion, E_g decreases slightly to about 2.32 eV, while at the same time the valence band begins to encroach upon the band gap. Peaks have appeared close to VBM. E_F of -2.46 eV for 1 Li is measured. At this low Li concentration, the DOS has approximately the same peaks shown figure 4.16b. Increasing the Li concentration up to 16 Li-ions, E_g has increased even further, measurable as roughly 2.55 eV. E_F of -0.92 eV for 16 Li is measured. The encroachment of the valence band into the band gap has increased considerably, creating the new band visible in figure 4.16c. This is indicative of an increased electron presence that can be attributed to the higher Li-ion concentration. This additional band decreases the effective E_g to 0.60 eV, a good indicator of the increased conductivity of the material as lithiation has increased.

With the addition of 1 Na-ion, E_g decreases slightly to about 2.35 eV, while at the same time the valence band begins to encroach upon the E_g. E_F of -2.37 eV for 1 Na is measured. This is visible due to the Fermi energy being position within the valence band. At this low Na concentration, the density of states has approximately the same peaks. Increasing the Na concentration up to 16 Na-ions, E_g has increased even further, measurable as roughly 2.53 eV. E_F of 0.03 eV for 16 Na is measured. The encroachment of the valence band into the band gap has increased considerably, creating the new band visible in figure 4.16e. This is indicative of an increased electron presence that can be attributed to the higher Na-ion concentration. This additional band decreases the effective E_g to 0.40 eV, a good indicator of the increased conductivity of the material as sodiation has increased.

4.5.3 DOS of Li/Na on Sn-vacancy SnS$_2$

The Sn-vacancy SnS$_2$ monolayer (TDOS in figure 4.17) has undergone a change in its electronic structure. It has a significantly increased E_g to 2.53 eV following the loss of an Sn atom. States are present in the band gap, and the widest gap measured within the band gap obtains a result of 1.74 eV. E_F has decreased massively to -3.93 eV, and is positioned closer to VBM versus the CBM like the other variations of the monolayer (see figure 4.17b). Thus, the SnS$_2$ monolayer is now shifting towards acting as a p-type semiconductor. With the addition an Li adatom, E_g is reduced to 2.36 eV, and more unexpected, E_F has decreased to -4.44 eV. The position of the Fermi energy as well as any states existing in the band gap have changed significantly. The band gap is now clear of any states, except for a bit of VBM where E_F is still placed. The material is now even more securely a p-type semiconductor, likely due to a substitution

occurring, with Li occupying the highest binding energy site at V_{Sn}. With the band gap clear of any states, the conductivity of the Sn-vacancy SnS_2 monolayer has decreased. This is likely due to p-type semiconductors having a limited number of electrons in the valence band, thus electrons of much lower energy are required to form the bond with the Li-ion. For 16 Li-ions, E_F has increased to -0.45 eV, and remains close to VBM, preserving the p-type semiconductor nature of the material. The band gap E_g remains significant at 2.20 eV. The Sn-vacancy SnS_2 monolayer retains poor conductivity.

With the addition of an Na-ion, the E_g is reduced to 2.30 eV, while E_F has decreased to -4.15 eV (see figure 4.17d). Overall, the reaction of the monolayer to the Na-ion is the same as its reaction to the introduction of the Li-ion. The Fermi energy has shifted more towards VBM, and the material acts as a p-type semiconductor. Conductivity will be less effective with the addition of ions, unlike the pristine and S-vacancy SnS_2 monolayer. The adatoms for LIBs and NIBs are all positively charged ions, which have more trouble bonding effectively to a p-type semiconductor, due to the excess holes present. Thus, the electronic properties of the Sn-vacancy SnS_2 monolayer also discourage the use of the material as an anode for LIBs/NIBs. For 16 Na-ions, E_F has increased to 0.62 eV, and appears to have moved away from VBM towards CBM, losing the p-type semiconductor nature of the material. The band gap E_g remains significant at 2.10 eV. Poor conductivity is retained, although it appears that increasing the Na concentration will eventually allow for improving this characteristic.

4.6   Open circuit voltage and storage capacity

(a) Li on SnS_2 V_{OC} (b) Na on SnS_2 V_{OC}
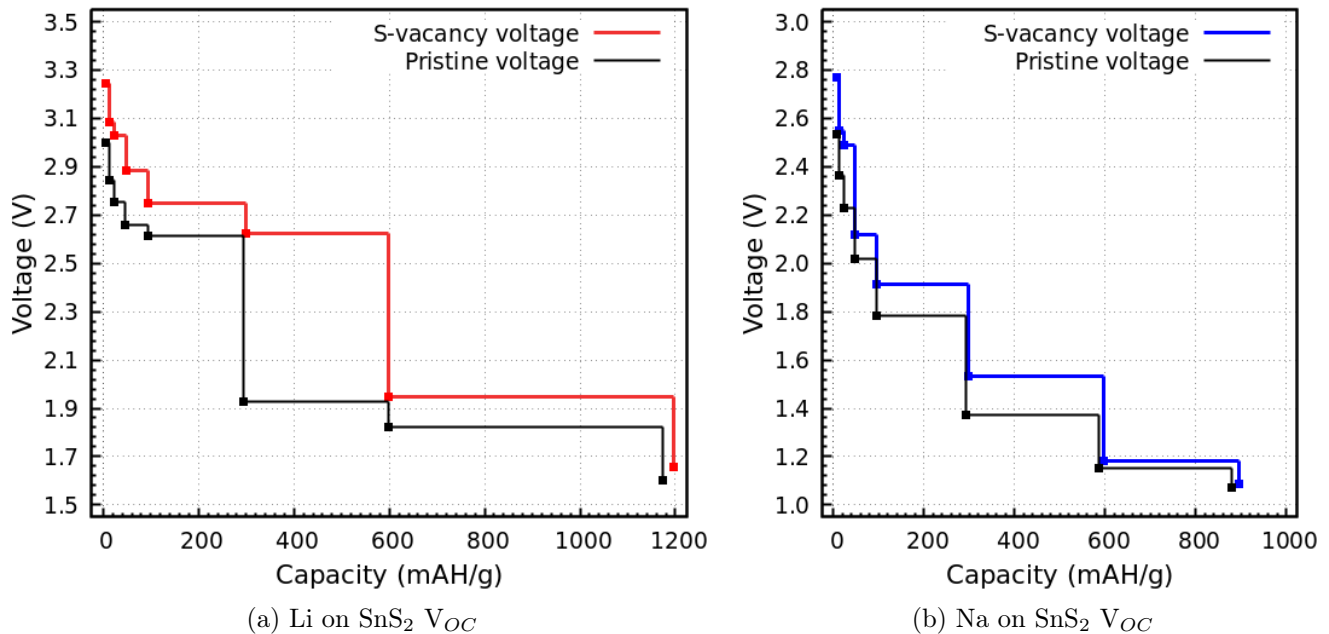
Figure 4.18: Variation in voltage for increasing (left) Li and (right) Na adatom capacity.

Another important property to evaluate the performance of the SnS_2 monolayer as an anode material is the open circuit voltage (V_{OC}). The V_{OC} represents the maximum voltage available from a cell, when no active current is flowing. It is derived by looking at the intercalation of adatoms onto the anode material, which will decrease the cell voltage for increasing intercalation. Thus, to obtain V_{OC} for Li/Na adatoms

on the SnS_2 monolayer, first consider the chemical reaction process for binding Li/Na adatoms to the substrate. These reactions are described by:

$$SnS_2 + xLi^+ + xe^- \rightleftharpoons Li_xSnS_2$$
$$SnS_2 + xNa^+ + xe^- \rightleftharpoons Na_xSnS_2,$$
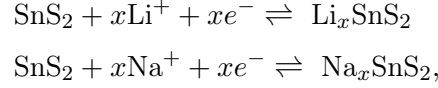
with x being the number of atoms undergoing intercalation during the reaction. Following this chemical reaction, we would have a change in V_{OC}, which will in turn cause a change in the total energy of the cell. For a metallic adatom anode, where the chemical potential of the adatoms is constant, the electrical energy produced by intercalation is equal to the Gibbs free energy G_r. The relationship between V_{OC} and G_r is:

$$V_{OC} = -\frac{\Delta G_r}{nF}, \tag{4.4}$$

where n is the number of adatoms in total adsorbed onto the SnS_2 monolayer, and Faraday's constant F is present as a conversion factor between joule J, the standard units of energy for Gibbs free energy, and voltage V. The change in Gibbs free energy G_r is described by the equation:

$$\Delta G_r = \Delta E_r + P\Delta V_r - T\Delta S_r, \tag{4.5}$$

where ΔE_r is the change in internal energy, P is pressure, ΔV_r is the change in volume, T is temperature, and ΔS_r is the change in entropy. We approximate the calculations by assuming they occur at 0 K to further simplify the equation. As a result, we have that the term $P\Delta V_r$ will be in the order of 10^{-5} eV, much smaller than the order of magnitude for E_r. Similarly, the $T\Delta S_r$ term is of an order with thermal energy, which is also negligible at 0 K. We are left with ΔE_r, which has the same magnitude as the binding energy such that $\Delta E_r = -\Delta E_b$. With the approximation we can use the following result[22]:

$$-\frac{\Delta G_r}{nF} = V_{OC} \approx \frac{\Delta E_b}{e}. \tag{4.6}$$

We have that Faraday's constant is absent, as the existing measurements for E_b are already in units of eV, making the inclusion of F for calculating V_{OC} unnecessary. Some conversion from eV to V must still occur through the cancellation of the electron charge e, though for eV we have that e is 1. The formula we have now obtained is near identical to the equation 4.3 binding energy E_b, bearing only a difference of units:

$$V_{OC} = -\left(\frac{E_{SnS_2+ad} - E_{SnS_2} - nE_{ad}}{ne}\right), \tag{4.7}$$

Looking at equation 4.6, it is clear that V_{OC} will decrease simultaneously with binding energy as the number of adatoms increases. This observation is supported by figures 4.18a and 4.18b, which depict V_{OC} for an increasing capacity of Li and Na adatoms respectively. It is generally known that for the maximum number of adatoms required on the SnS_2 monolayer, the V_{OC} should approach 0.00 V. Just like for binding energy analysis, the positive V_{OC} values reveal that Li/Na adatoms on the SnS_2 monolayer are likely to be bound to the surface, while negative values will have undesired clustering.

Figures 4.18a and 4.18b clearly show that the V_{OC} value for Li reduces from 3.00 V to 1.60 V , while

for Na it reduces from 2.53 V to 1.07 V, for an increasing adatom capacity on the pristine SnS_2 substrate. The maximum capacity is not quite reached, although we have bypassed several existing values obtained for the maximum theoretical specific capacity (averaging at $\sim$1200 mAh/g for LIBs[23,24] and $\sim$800 mAh/g for NIBs[16,24]). Moving on, it can be noted that the Li/Na adatoms on the S-vacancy SnS_2 monolayer consistently have higher V_{OC} values compared to pristine, for the entire plot. Qualitatively, V_{OC} for Li reduces from 3.24 V to 1.66 V , while for Na it reduces from 2.77 V to 1.09 V.

We can also calculate the average V_{OC}. On the pristine SnS_2 monolayer, we would have average voltages of 2.18 V for Li and 1.66 V for Na. In comparison, the S-vacancy SnS_2 gives us higher voltages, being 2.507 V for Li and 1.79 V for Na. The pristine V_{OC} values fall within the acceptable range of 1.00–2.50 V seen in numerous studies[16,20,25], although the average V_{OC} is higher than results in these same studies. The discrepancy is due to our capacity falling just short of maximum capacity for which V_{OC} would be 0 V. We can still conclude that the SnS_2 monolayer can act as an anode material capable of yielding significant charging voltage. In addition, we have significant storage capacity still capable of high V_{OC} values, indicating that clustering and the formation of dendrites should be averted during battery operation.

So far, we have mentioned storage capacity or specific capacity several times. In general, the theoretical specific capacity C is defined by the following equation[22]:

$$C = \frac{znF}{M_{SnS_2}},\tag{4.8}$$

where z is the number of valence electrons of the adatoms (1 in the case of Li and Na), the Faraday constant F is set to 26801 mAh/mol, and M_{SnS_2} is the total molar mass of the SnS_2 monolayer supercell. S-vacancy SnS_2 monolayer will have a slightly lower molar mass than pristine, and consequently, a slightly higher storage capacity if we consider equation 4.6, if the S-vacancy does not significantly hinder the storage capacity. It is shown in figure 4.18 that for the pristine SnS_2 monolayer, the obtained storage capacity at the highest observed Li concentration is 1172.65 mAh/g, with the corresponding chemical formula being Li_8SnS_2 (corresponding to 72 Li adatoms on a 3×3 SnS_2 supercell). For the highest observed Na concentration, with chemical formula Na_6SnS_2, storage capacity was determined to be 879.49 mAh/g. For the S-vacancy SnS_2 monolayer, the obtained storage capacity has increased to 1195.95 mAh/g for the same Li concentration, and similarly for Na the increased storage capacity is 896.96 mAh/g. Immediately, we see that for one S-vacancy, there has been no hinderance to storage capacity. Our results are fairly high, and should be higher than the lower results previously determined for theoretical capacity, being 1200 mAh/g for Li and 600 mAh/g for Na.[16,23,24] Practically, recall that the maximum storage capacity is determined at a point were the voltage reaches 0 V, after which no additional adatoms can be bound. Regardless of what that maximum capacity will be, the storage capacity of our substrate is already significantly greater than that of graphite (372 mAh/g for Li and 150 mAh/g for Na[26,27]) and graphene nanosheets (540 mAh/g for Li and 220 mAh/g for Na[28,29]). Monolayer SnS_2 offers excellent high energy storage in its application as an anode material for LIBs and NIBs.

Bibliography

[1] Charles Kittel and Paul McEuen. *Introduction to Solid State Physics*. John Wiley & Sons, 2018.

[2] C. Bacaksiz, S. Cahangirov, A. Rubio, R. T. Senger, F. M. Peeters, and H. Sahin. Bilayer SnS_2: Tunable stacking sequence by charging and loading pressure. *Phys. Rev. B*, 93:125403, Mar 2016. doi: 10.1103/PhysRevB.93.125403. URL `https://link.aps.org/doi/10.1103/PhysRevB.93.125403`.

[3] F. A. S. Al-Alamy, A. A. Balchin, and M. White. The expansivities and the thermal degradation of some layer compounds. *Journal of Materials Science*, 12(10):2037–2042, Oct 1977. ISSN 1573-4803. doi: 10.1007/BF00561976. URL `https://doi.org/10.1007/BF00561976`.

[4] H.B. Mabiala-Poaty, D.H. Douma, B. M'Passi-Mabiala, and R.E. Mapasha. Structural and electronic properties of SnS_2 stacked nanosheets: An ab-initio study. *Journal of Physics and Chemistry of Solids*, 120:211–217, 2018. ISSN 0022-3697. doi: https://doi.org/10.1016/j.jpcs.2018.04.026. URL `https://www.sciencedirect.com/science/article/pii/S0022369717325179`.

[5] Hendrik J. Monkhorst and James D. Pack. Special points for Brillouin-zone integrations. *Phys. Rev. B*, 13:5188–5192, Jun 1976. doi: 10.1103/PhysRevB.13.5188. URL `https://link.aps.org/doi/10.1103/PhysRevB.13.5188`.

[6] N.G. Deshpande, A.A. Sagade, Y.G. Gudage, C.D. Lokhande, and Ramphal Sharma. Growth and characterization of tin disulfide (SnS_2) thin film deposited by successive ionic layer adsorption and reaction (SILAR) technique. *Journal of Alloys and Compounds*, 436(1):421–426, 2007. ISSN 0925-8388. doi: https://doi.org/10.1016/j.jallcom.2006.12.108. URL `https://www.sciencedirect.com/science/article/pii/S0925838806022444`.

[7] S.K. Panda, A. Antonakos, E. Liarokapis, S. Bhattacharya, and S. Chaudhuri. Optical properties of nanocrystalline SnS_2 thin films. *Materials Research Bulletin*, 42(3):576–583, 2007. ISSN 0025-5408. doi: https://doi.org/10.1016/j.materresbull.2006.06.028. URL `https://www.sciencedirect.com/science/article/pii/S0025540806002856`.

[8] Xianghua Hu, Guosheng Song, Wenyao Li, Yanling Peng, Lin Jiang, Yafang Xue, Qian Liu, Zhigang Chen, and Junqing Hu. Phase-controlled synthesis and photocatalytic properties of SnS, SnS_2 and SnS/SnS_2 heterostructure nanocrystals. *Materials Research Bulletin*, 48(6):2325–2332, 2013. ISSN 0025-5408. doi: https://doi.org/10.1016/j.materresbull.2013.02.082. URL `https://www.sciencedirect.com/science/article/pii/S0025540813001670`.

[9] Fangfang Wang, Qiushi Yao, Liyu Zhou, Zhen Ma, Mingxue He, and Fang Wu. Theoretical understanding of SnS monolayer as Li ion battery anode material. *Journal of Physics and Chemistry of Solids*, 121:261–265, 2018. ISSN 0022-3697. doi: https://doi.org/10.1016/j.jpcs.2018.05.043. URL `https://www.sciencedirect.com/science/article/pii/S0022369718302671`.

[10] Taohua Huang, Binwei Tian, Jiyuan Guo, Huabin Shu, Ying Wang, and Jun Dai. Semiconducting borophene as a promising anode material for Li-ion and Na-ion batteries. *Materials Science in Semiconductor Processing*, 89:250–255, 2019. ISSN 1369-8001. doi: https://doi.org/10.1016/j.mssp.2018.09.025. URL `https://www.sciencedirect.com/science/article/pii/S1369800118313209`.

[11] Jingcang Su, Yong Pei, Zhenhua Yang, and Xianyou Wang. Ab initio study of graphene-like monolayer molybdenum disulfide as a promising anode material for rechargeable sodium ion batteries. *RSC Adv.*, 4:43183–43188, 2014. doi: 10.1039/C4RA06557C. URL `http://dx.doi.org/10.1039/C4RA06557C`.

[12] Yong-Chao Rao, Song Yu, Xiao Gu, and Xiang-Mei Duan. Prediction of MoO2 as high capacity electrode material for (Na, K, Ca)-ion batteries. *Applied Surface Science*, 479:64–69, 2019. ISSN 0169-4332. doi: https://doi.org/10.1016/j.apsusc.2019.01.206. URL `https://www.sciencedirect.com/science/article/pii/S0169433219302387`.

[13] Yungang Zhou and Cheng Geng. A MoO_2 sheet as a promising electrode material: ultrafast Li-diffusion and astonishing Li-storage capacity. *Nanotechnology*, 28(10):105402, 2017. doi: 10.1088/1361-6528/aa56d0. URL `https://doi.org/10.1088/1361-6528/aa56d0`.

[14] Javed Rehman, Xiaofeng Fan, and W.T. Zheng. Computational insight of monolayer SnS_2 as anode material for potassium ion batteries. *Applied Surface Science*, 496:143625, 2019. ISSN 0169-4332. doi: https://doi.org/10.1016/j.apsusc.2019.143625. URL `https://www.sciencedirect.com/science/article/pii/S0169433219324225`.

[15] Yagang Lv, Biao Chen, Naiqin Zhao, Chunsheng Shi, Chunnian He, Jiajun Li, and Enzuo Liu. Interfacial effect on the electrochemical properties of the layered graphene/metal sulfide composites as anode materials for Li-ion batteries. *Surface Science*, 651:10–15, 2016. ISSN 0039-6028. doi: https://doi.org/10.1016/j.susc.2016.03.018. URL `https://www.sciencedirect.com/science/article/pii/S0039602816300164`.

[16] Abdus Samad, Mohammad Noor-A-Alam, and Young-Han Shin. First principles study of a SnS_2/graphene heterostructure: a promising anode material for rechargeable Na ion batteries. *J. Mater. Chem. A*, 4:14316–14323, 2016. doi: 10.1039/C6TA05739J. URL `http://dx.doi.org/10.1039/C6TA05739J`.

[17] Hao Wu, Zhonglu Guo, Jian Zhou, and Zhimei Sun. Vacancy-mediated lithium adsorption and diffusion on MXene. *Applied Surface Science*, 488:578–585, 2019. ISSN 0169-4332. doi: https://doi.org/10.1016/j.apsusc.2019.05.311. URL `https://www.sciencedirect.com/science/article/pii/S0169433219316198`.

[18] Sankha Mukherjee, Avinav Banwait, Sean Grixti, Nikhil Koratkar, and Chandra Veer Singh. Adsorption and Diffusion of Lithium and Sodium on Defective Rhenium Disulfide: A First Principles Study. *ACS Applied Materials & Interfaces*, 10(6):5373–5384, 2018. doi: 10.1021/acsami.7b13604. URL `https://doi.org/10.1021/acsami.7b13604`. PMID: 29350901.

[19] Yaming Liu, Bo Hu, Dechuan Kong, Jianye Wang, Yongfeng Li, Jianxiu Su, and Congxin Xia. Effect of S-vacancy on the oxidation state of Ce in monolayer SnS_2. *International Journal of Modern Physics B*, 33(26):1950308, 2019. doi: 10.1142/S0217979219503089.

[20] Yu Huang, Shengqi Ding, Sunjie Xu, Zi-Feng Ma, and Xianxia Yuan. Binder-free SnS_2 sheet array with high sulfur vacancy concentration for enhanced lithium storage performance. *Electrochimica*

Acta, 409:139979, 2022. ISSN 0013-4686. doi: https://doi.org/10.1016/j.electacta.2022.139979. URL `https://www.sciencedirect.com/science/article/pii/S0013468622001517`.

[21] Meysam Makaremi, Bohayra Mortazavi, Timon Rabczuk, Geoffrey A. Ozin, and Chandra Veer Singh. Theoretical Investigation: 2D N-Graphdiyne Nanosheets as Promising Anode Materials for Li/Na Rechargeable Storage Devices. *ACS Applied Nano Materials*, 2(1):127–135, 2019. doi: 10.1021/acsanm.8b01751. URL `https://doi.org/10.1021/acsanm.8b01751`.

[22] M. K. Aydinol, A. F. Kohan, G. Ceder, K. Cho, and J. Joannopoulos. Ab initio study of lithium intercalation in metal oxides and metal dichalcogenides. *Phys. Rev. B*, 56:1354–1365, Jul 1997. doi: 10.1103/PhysRevB.56.1354. URL `https://link.aps.org/doi/10.1103/PhysRevB.56.1354`.

[23] Yeyun Wang, Junhua Zhou, Jinghua Wu, Fengjiao Chen, Peirong Li, Na Han, Wenjing Huang, Yuping Liu, Hualin Ye, Feipeng Zhao, and Yanguang Li. Engineering SnS_2 nanosheet assemblies for enhanced electrochemical lithium and sodium ion storage. *J. Mater. Chem. A*, 5:25618–25624, 2017. doi: 10.1039/C7TA08056E. URL `http://dx.doi.org/10.1039/C7TA08056E`.

[24] Zhen Kong, Meiling Huang, Zhenyan Liang, Huayao Tu, Kang Zhang, Yongliang Shao, Yongzhong Wu, and Xiaopeng Hao. Phosphorus doping induced the co-construction of sulfur vacancies and heterojunctions in tin disulfide as a durable anode for lithium/sodium-ion batteries. *Inorg. Chem. Front.*, 9:902–913, 2022. doi: 10.1039/D1QI01536B. URL `http://dx.doi.org/10.1039/D1QI01536B`.

[25] Jianbiao Wang, Jiajia Huang, Shuping Huang, Hiroo Notohara, Koki Urita, Isamu Moriguchi, and Mingdeng Wei. Rational Design of Hierarchical SnS_2 Microspheres with S Vacancy for Enhanced Sodium Storage Performance. *ACS Sustainable Chemistry & Engineering*, 8(25):9519–9525, 2020. doi: 10.1021/acssuschemeng.0c02535. URL `https://doi.org/10.1021/acssuschemeng.0c02535`.

[26] Bingkun Guo, Xiqing Wang, Pasquale F. Fulvio, Miaofang Chi, Shannon M. Mahurin, Xiao-Guang Sun, and Sheng Dai. Soft-Templated Mesoporous Carbon-Carbon Nanotube Composites for High Performance Lithium-ion Batteries. *Advanced Materials*, 23(40):4661–4666, 2011. doi: https://doi.org/10.1002/adma.201102032. URL `https://onlinelibrary.wiley.com/doi/abs/10.1002/adma.201102032`.

[27] Yue Dong, Xieji Lin, Dengke Wang, Renlu Yuan, Su Zhang, Xiaohong Chen, Lyubov G. Bulusheva, Alexander V. Okotrub, and Huaihe Song. Modulating the defects of graphene blocks by ball-milling for ultrahigh gravimetric and volumetric performance and fast sodium storage. *Energy Storage Materials*, 30:287–295, 2020. ISSN 2405-8297. doi: https://doi.org/10.1016/j.ensm.2020.05.016. URL `https://www.sciencedirect.com/science/article/pii/S240582972030194X`.

[28] Sheng Han, Dongqing Wu, Shuang Li, Fan Zhang, and Xinliang Feng. Graphene: A Two-Dimensional Platform for Lithium Storage. *Small*, 9(8):1173–1187, 2013. doi: https://doi.org/10.1002/smll.201203155. URL `https://onlinelibrary.wiley.com/doi/abs/10.1002/smll.201203155`.

[29] Xu-Feng Luo, Cheng-Hsien Yang, You-Yu Peng, Nen-Wen Pu, Ming-Der Ger, Chien-Te Hsieh, and Jeng-Kuei Chang. Graphene nanosheets, carbon nanotubes, graphite, and activated car-

bon as anode materials for sodium-ion batteries. *J. Mater. Chem. A*, 3:10320–10326, 2015. doi: 10.1039/C5TA00727E. URL `http://dx.doi.org/10.1039/C5TA00727E`.

Chapter 5

Conclusions

Using a DFT approach, we systematically performed a comparative study of the adsorption and diffusion behaviour of Li/Na on a pristine SnS_2 monolayer, as well as on a vacancy SnS_2 monolayer, looking to enhance electrochemical performance. In brief, we looked for improvements in the Li/Na binding energies, V_{OC}, storage capacities and electronic conductivity. Although all adsorption sites are exothermic, it was established that Li/Na adatoms bind more strongly to H_{SnS_2} and some T_{Sn} sites within the vicinity of the S-vacancy on the defective SnS_2 monolayer, while avoiding the S-vacancy site V_S (there was possible unwanted repulsive force between Li/Na and surrounding Sn atoms). The T_S sites, and T_{Sn} sites for Li adatoms, instead experienced a loss of stability. The Li/Na adatoms tended to bind strongly to the Sn-vacancy. Structural analysis of the Sn-vacancy SnS_2 monolayer revealed that the V_{Sn} site entrapped Li/Na adatoms, forming a substitutional defect. It was also noted that a great number of Li/Na ions can be stored on the substrate without forming bulk metallic, due to the steepness of binding energy plot. The Na ions with larger atomic radii than Li ions had lower binding energies in general. We also studied the diffusion of Li/Na across the S-vacancy SnS_2 monolayer by calculating activation energies. It was established that by avoiding the S-vacancy site along the path, excellent diffusion barriers of 0.19 eV for Li and 0.13 eV for Na could be achieved. The Sn-vacancy surface was not as useful, having introduced significantly increased diffusion barriers across the surface area affected by the S-vacancy.

The S-vacancy in effect introduced electronic states, with pronounced peaks crossing the Fermi level (indicating a metallic character), as well as the shrinkage of E_g from 2.44 eV to approximately 2.00 eV. The addition of Li/Na adatoms introduced more electronic states on the band gap. These induced states became more populated as the number of Li/Na adatoms increased, suggesting the possibility of enhanced electronic transmission performance, a requirement for effective LIBs and NIBs. In contrast, the Sn-vacancy shifted the Fermi energy towards the VBM, altering the material to act as a p-type semiconductor. The creation of V_{Sn} increased E_g to approximately 2.50 eV, with some in gap states present to improve conductivity. However, following the addition of Li/Na adatoms, these electronic states were lost, and a large band gap was maintained to the detriment of conductivity. This suggests that the Sn-vacancy SnS_2 monolayer showcased poor electronic transmission performance, discouraging its use in LIBs and NIBs.

In this study, only pristine and S-vacancy SnS_2 monolayers were considered as viable for application in LIBs/NIBs, and underwent additional calculations to evaluate their voltage and capacity characteristics. The calculated V_{OC} values of our electrode materials was higher than those of graphite and graphene

electrodes, owing to S atoms having more electronegativity than C atoms. It was also noted that the Li/Na adatoms on the SnS_2 monolayer with a S-vacancy, which created more reactive sites, had higher V_{OC} values compared to its pristine counterparts. The obtained V_{OC} values indicates that the formation of dendrites can surely be averted for the envisaged battery operation. The decrease in V_{OC} was a reaction to an increased concentration in adatoms, thus an increase in the measured specific capacity C. Even before V_{OC} had fallen below 1.00 V, the measured C values had surpassed comparable maximum C measurements of 1200 mAh/g for Li and 800 mAh/g for Na. There are few discernible differences in storage capacity between the pristine and S-vacancy SnS_2 monolayers, with both having far higher Li/Na storage capacities than other graphene-like materials. Therefore, both SnS_2 monolayer configurations offers exceptional storage for application in high capacity energy storage devices.

Understanding the effects of vacancy defects on the electrochemical properties of Li/Na on the SnS_2 monolayer allows us to consider possible improvements to energy storage devices that can be applied as result of our improved anode material. The application of S-vacancy SnS_2 monolayers in particular can be explored in more detail, looking in more depth at their electronic properties and especially long-term cycling capabilities. We can also consider similar adsorption atoms such as potassium, as well as the use of doping, and homogeneous and heterogeneous layering, in concert with vacancy defects, to further improve the electrochemical properties of the anode material.

The investigation into vacancy defects on an SnS_2 monolayer has resulted in the alteration of multiple properties, with S-vacancies offering more benefits for the application of SnS_2 in energy storage devices. The obtained results can be expanded upon, through more thorough theoretical and experimental studies of defect engineering in SnS_2. Additionally, this also opens the door to experimental studies into the viability of S-vacancies or vacancies in general in similar 2D materials.

Appendix

The *Advances in Surfaces, Interfaces and Interphases 2022* conference, which took place online from Sunday 15th May to Wednesday 18th May, was attended. At the conference, we presented a poster describing preliminary results of the dissertation, along with a video outlining the research. A written paper regarding the results of the dissertation has also been published by the *Journal of Solid State Electrochemistry* on the 16th of May 2023 [link].